MICHIGAN STATE UNIVERSITY LIBRARIES
3 1293 00791 4520

LIBRARY
Michigan State
University

This is to certify that the

dissertation entitled

Development of Iron Porphyrin-Doped Metalorganic Thin-Film Membranes for Optically Based Chemical Sensing Applications

presented by

Charles D. Gagliardi

has been accepted towards fulfillment
of the requirements for

PhD degree in Chem. Eng.

Major professor

Date Nov 13, 1992

MSU is an Affirmative Action/Equal Opportunity Institution

0-12771

PLACE IN RETURN BOX to remove this checkout from your record.
TO AVOID FINES return on or before date due.

DATE DUE	DATE DUE	DATE DUE

MSU Is An Affirmative Action/Equal Opportunity Institution
c:\circ\datedue.pm3-p.

DEVELOPMENT OF IRON PORPHYRIN-DOPED METALORGANIC THIN-FILM MEMBRANES FOR OPTICALLY BASED CHEMICAL SENSING APPLICATIONS

By

Charles D. Gagliardi

A DISSERTATION

Submitted to
Michigan State University
in partial fulfillment of the requirements
for the degree of

DOCTOR OF PHILOSOPHY

Department of Chemical Engineering

1992

ABSTRACT

DEVELOPMENT OF IRON PORPHYRIN-DOPED METALORGANIC
THIN-FILM MEMBRANES FOR OPTICALLY BASED
CHEMICAL SENSING APPLICATIONS

By

Charles D. Gagliardi

Ferrihemes (Fe(III) porphyrins) were successfully incorporated into very thin, highly porous, optically clear, metalorganic films, and reduced *insitu* to the Fe(II) state. Porphyrin-film compatibility was established by using various functional groups on the porphyrin ring to chemically bind to the metalorganic polymer. Carboxyl, hydroxyl, and pentafluorophenyl groups were effective in securely incorporating the porphyrin within the amorphous film matrix. The hydroxyl and carboxyl group reactivities were well established from the literature; the reactivity of the pentafluorophenyl group was somewhat less well defined, but resonance Raman spectra were attained which strongly suggest that the porphyrin had chemically reacted with the film solution. Porphyrins with these functional groups were incorporated into films at sufficiently high concentrations to provide strong UV-vis absorption at film thicknesses of 850 ± 250 Å.

The chemical stability of the coating solutions was studied to improve film reproducibility. The solutions and films were characterized with vibrational spectroscopy.

The film material was structurally characterized with transmission electron microscopy (TEM) and atomic force microscopy (AFM) indicating the amorphous nature of the material. A general pore-size range of 10-100 Å can be approximated from the images.

The transport of aqueous carbon monoxide into the film, and the reactivity of the solute with Fe(II) porphyrin complexes were also studied, showing that the Fe(III) porphyrins incorporated into the films could be reduced *insitu* and then reacted with the diffusing solute. These studies proved that the iron porphyrin-doped films can be used for sensing applications and for probing the internal structure of the film. The diffusion of CO into the film provides evidence of a fairly broad or possibly bimodal pore-size distribution in which the material has both regions of high and low permeability.

Dedicated to my parents, Charles and Leola Gagliardi.

ACKNOWLEDGEMENTS

I am grateful to my graduate advisor, Dr. Kris A. Berglund, for his energetic enthusiasm, dependable support, and invaluable guidance. His inspiration and encouragement will never be forgotten. The generous funding for my work provided by the Center for Fundamental Materials Research (CFMR) and the Composite Materials and Structures Center (CMSC) at Michigan State University, and by the United States Department of Agriculture (USDA), is acknowledged with much gratitude. The Michigan State University LASER Lab facility provided me with the use of excellent LASER and spectroscopy equipment which I depended upon for many of my experiments, and the Center for Electron Optics provided excellent training and equipment for acquiring TEM, SEM, and AFM data.

Special thanks are also due to Dr. Daniel Nocera, Dr. Carl Lira, Dr. Karen Klomparens, and Dr. Chris Chang for serving on my graduate committee. Their suggestions and advice have been most helpful.

The work of Dilum Dunuwila as an undergraduate research assistant was a great and much appreciated contribution to this project, and discussions with Bharath Rangarajan have also been greatly appreciated. Thanks are also due Jeeseong Hwang, Richard Edelmann, and Dr. Peggy Hogan for their assistance at the Center for Electron Optics. I would also like to thank Dr. Tony Oertling and Dr. Mike Cerreta for their help in learning Raman spectroscopy and proper laser operation and maintenance, and Dr. Ron Lessard, Dr. Joel Dulebon, and Dr. Beatrice Van Vlierberge-Torgerson for their consultations and advice.

TABLE OF CONTENTS

LIST OF TABLES

Page

LIST OF FIGURES

INTRODUCTION

The investigations which comprise this dissertation are based on the hypothesis that optically useful concentrations of a securely incorporated Fe(II) porphyrin can be achieved within porous, optically clear, metalorganic membranes which can then be used as optically probed chemical sensing devices. The research investigates this hypothesis and addresses problems of compatibility between the porphyrin and the film material; the chemical and structural characteristics of the membrane are also investigated to characterize the membrane and aid in the modeling of mass transport within the material.

Membrane technology encompasses a diverse array of materials, structural features, functional behavior, and applications. The word "membrane" originates from the Latin word "membrana," meaning skin (Webster's 7^{th} ed., 1969), and the term commonly refers to a natural or synthetic layer which is permeable by at least one component of a solution or mixture. In an attempt to organize and class the many types of membranes, individuals have devised a variety of different organizational schemes. At this time, however, there is no generally accepted, comprehensive organizational framework, and some reviewers doubt that one can be adopted without sacrificing clarity (Hwang and Kammermeyer, 1975; Lakishminarayanaiah, 1969). It should also be noted that new types of membranes are continually being developed, which increases the difficulty of organization. A comprehensive description

of membrane types and categories is not appropriate to this dissertation; however, many interesting organizational schemes can be found in the two previous references.

Mimetic membranes can be considered as one of the most interesting membrane categories. Many synthetic membranes have been created to mimic the behavior of their naturally occurring counterparts and others are used to house chemicals which themselves imitate some natural phenomenon; both could be classed as mimetic membranes. Mimetic chemistry is of great importance in both primary and applied areas of research: the mimetic model can deepen the understanding of the modelled natural phenomenon, and the model itself can be of substantial industrial value. Iron porphyrins (hemes), being of great biological importance, are undoubtedly among the most widely studied compounds of this nature.

Placing the heme in a film material which does not disable the chemical phenomenon of interest is not a trivial task. Many film materials may demetalate or otherwise chemically deactivate the heme. Furthermore, many film materials would block its reaction with other molecules by steric hindrance. However, if the heme can be placed in a film without being blocked or chemically deactivated, the heme-film system could be used to study the transport properties of the hosting membrane. The diffusion properties of the film can be studied by allowing some species to diffuse through the membrane while monitoring the ligand formation via optical absorption spectroscopy. Ferriheme complexes incorporated into a transparent hosting membrane can be used with a variety of solutes including carbon monoxide, oxygen, and t-butylisocyanide.

Several film materials have proved promising for use as hosting membranes. Titanium, zirconium, and hafnium alkoxides have been combined with carboxylic acids, and the resulting complexes have been hydrolyzed to yield porous, optically transparent, metalorganic polymer films (Gagliardi and Berglund, 1989). The most solvent resistant of these films resulted from the combination of titanium isopropoxide with valeric acid (Gagliardi, et. al., 1990), and the current work focuses on the use of this membrane material.

Certain hemes were found to be compatible with this titanium metalorganic film, providing several suitable film-heme systems. By studying these systems, we intended to learn about the transport properties of the membranes, which we then hoped to understand in terms of the morphology and chemical composition of the material.

The importance of this research rests on the many possible applications for these membranes. The membranes themselves are highly unique due to the combination of their optical clarity, high porosity, small pore size, and apparent homogeneity. The films could be used as separation process membranes or as supports for catalysts or photocatalysts. The methods of doping the films with porphyrin may act as general methods for introducing other catalytically active macromolecules. The hemes to be used in these experiments are themselves of interest as mimetic agents and as catalysts, and the film-heme systems have been shown to be useful as the basis for a carbon monoxide sensor.

The relevant literature concerning membranes and porphyrins will be reviewed, as will the many analytical techniques required for the experiments. The primary goal of this work was to understand the

transport properties in terms of the structural and chemical features of the membrane. A secondary goal of this research was to demonstrate the usefulness of a film-porphyrin system as a CO sensor.

CHAPTER 1.

FILM MATERIALS AND PROCESSING METHODS

Since this investigation is concerned with the characterization and use of porphyrin-doped metalorganic films, it is proper to include a description of the basic materials and methods which control the properties of the films. I will begin with the transition metals themselves, and then proceed to briefly review the nature of colloids and gels, sol-gel processing, alkoxides, carboxylates, and the alcohols, carboxylic acids, and esters which are involved in the production of our coating solutions. Finally, I will discuss the coating solutions and methods themselves.

1.1. TITANIUM, ZIRCONIUM, AND HAFNIUM

Each of the coating materials generated and studied for this work involves titanium, zirconium, or hafnium. These elements comprise the group IV transition or 'd' block metals in the periodic table. To distinguish the transition metal groups from the main element groups, the CAS nomenclature uses an 'A' to designate the main groups and a 'B' to designate the transition groups; the older IUPAC nomenclature is in conflict with this convention. Throughout the remainder of this document I will refer to the transition group IV elements simply as 'group IV' without further distinction.

Titanium is the most abundant element of the group, making up 63% of the earth's crust. Among all the transition metals, titanium is the second most abundant. Zirconium represents roughly 1.6% of the crust, while hafnium comprises less than 0.03%. However, when compared to other elements, hafnium is no more rare than cesium or bromine (Greenwood and Earnshaw, 1984).

Some of the physical properties of Ti, Zr, and Hf are presented in Table 1. Due to the "lanthanide contraction", the ionic radii of Zr and Hf are virtually identical; the only significant difference between these elements are their densities, transition temperatures, and neutron absorbing abilities (Greenwood and Earnshaw, 1984).

Table 1. Some properties of group IV transition metals.

Property		Ti	Zr	Hf
Atomic number		22	40	72
Number of natural isotopes		5	5	6
Atomic weight		47.88	91.22	178.49
Electronic Configuration		[Ar] $3d^2 4s^2$	[Kr] $4d^2 5s^2$	[Xe] $4f^{14}$ $3d^2 4s^2$
Electronegativity		1.5	1.4	1.3
Metal radius/pm		147	160	159
Ionic radius (6 coord.)/pm	M(IV)	60.5	72	71
	M(III)	67.0		
	M(II)	86		
MP/°C		1667	1857	2222
BP/°C		3285	4200	4450
Enthalpy of fusion/kJ/mole		18.8	19.2	(25)
Enthalpy of vaporization/kJ/mole		425	567	571
Density (25°C) g/cm^3		4.5	6.5	13.28
Electrical resistivity (25°C) μohm cm		42.0	40.0	35.1

(Greenwood and Earnshaw, 1984)

The metals are highly corrosion resistant. Except for hydrofluoric acid, mineral acids have little effect on the dense oxide layer which

forms over the metal's surface. The group IV transition metals also exhibit a large range of oxidation states and coordination numbers which are shown in Table 2 (Greenwood and Earnshaw, 1984).

From Table 2, it is apparent that the group IV metals are capable of showing a wide range of complex chemical behavior. It is the richness of this chemistry that will enable us to adjust the properties of our coating materials to suit the needs of specific applications.

1.2. COLLOIDAL SUSPENSIONS AND GELS

A *colloid* has been defined as a suspension of a finely dispersed phase (~1 - 1,000 nm) not significantly affected by gravitational settling, with interaction dominated by short-range forces such as van der Waals attraction and surface charges. The dispersed phase also characteristically exhibits Brownian motion, due to random collisions with molecules of the supporting medium (Brinker and Scherer, 1990).

Colloidal suspensions in a gaseous medium are termed *aerosols*; colloidal liquid droplets in a liquid medium are *emulsions*. A *sol*, distinct from both aerosols and emulsions, is defined as a colloidal suspension of a dispersed solid phase in a liquid medium, where the "solid" can be either *particulate* (non-polymeric) or *polymeric* (Brinker and Scherer, 1990).

Many polymeric systems could also be legitimately considered true solutions rather than sols, and so the terminology chosen often depends

Table 2. Oxidation state, coordination, and stereochemistry

Oxidation state	Coordination	Stereochemistry	Ti	Zr/Hf
-1 (d^5)	6	Octahedral	$[Ti(bipy)_3]^-$	--
0 (d^4)	6	Octahedral	$[Ti(bipy)_3]$	$[Zr(bipy)_3]$
2 (d^2)	6	Octahedral	$TiCl_2$	Layer structures and clusters
	12	--	$[Ti(\eta^5\text{-}C_5H_5)_2(CO)_2]$	
3 (d^1)	3	Planer	$[Ti\{N(SiMe_3)_2\}_2(CO)2]$	
	5	Trigonal bipyr.	$[TiBr_3(NMe_3)_2]$	
	6	Octahedral	$[Ti(urea)_6]^{3+}$	ZrX_3 (Cl, Br, I), HfI_3
4 (d^0)	4	Tetrahedral	$TiCl_4$	$ZrCl_4$(g) (solid is octahedral)
	5	Trigonal bipyr.	$[TiOCl_2(NMe_3)_2]$	--
		Square pyramidal	$[TiOCl_4]^{2-}$	--
	6	Octahedral	$[TiF_6]^{2-}$	$[ZrF_6]^{2-}$, $ZrCl_4$(s)
	7	Pentagonal bipyramidal	$[TiCl(S2CNMe_2)_3]$	--
		Capped trigonal prismatic	$[TiF_5(O_2)]^{3-}$	$[Zr_2F_{13}]^{5-}$
	8	Dodecahedral	$[Ti(\eta^2\text{-}NO_3)_4$	$[Zr(C_2O_4)_4]^{4-}$
		Square antiprismatic	--	$Zr(acac)_4$
	11	--	$[Ti(\eta^5\text{-}C_5H_5)(S_2CNMe_2)_3]$	
	12	--	--	$[M(\eta^3\text{-}BH_4)_4$

(Greenwood and Earnshaw, 1984)

upon the context. The kinetics must also be considered; a solution of monomers and oligomers may gradually evolve into a polymeric sol, and eventually become a particulate sol or gel. There is no exact time when the polymer becomes large enough for the solution to be considered a sol, and the choice of terminology in describing the initial stage may well depend on the kinetics of the reaction.

A *gel* is a substance characterized by the presence of a continuous solid skeleton wet by a continuous liquid phase. Gels can result from the growth of branched or cross-linked polymers, the entanglement of polymeric molecules, or the formation of particulate networks held together by van der Waals forces. Gels can be clear, cloudy, or opaque, and the liquid phase of the gel can exist as a solution, polymeric sol, or particulate sol. The process of gelation generally begins with the formation of fractal aggregates that grow into clusters that link together, as sometimes described by the theory of percolation, until a spanning cluster extends throughout the sol (Brinker and Scherer, 1990). In polymeric systems, the theory of bond percolation seems most applicable to simple cases where a monomer forms bonds at random between neighboring molecules. Complex chemical systems may not be so easily adaptable to this method of modelling.

When gels are allowed to dry by the evaporation of the liquid phase into a surrounding gas phase, the process is accompanied by significant shrinkage and *xerogels* (xero = dry) result. These xerogels are often highly porous and have been used as catalyst supports and filtering media. Gels can also be dried under supercritical conditions, producing *aerogels* which are significantly less dense than the corresponding xerogels.

1.3. SOL-GEL PROCESSING

A variety of systems which exhibit sol formation and gelation can be very useful in the manufacturing of homogeneous powders, radioactive oxide particles, ceramics (including fibers and multicomponent glasses), films, coatings, and monoliths. The recent popularity of the sol-gel approach is attributed to the demonstration by Yoldas (Yoldas, 1975 and 1977) and Yamane and coworkers (Yamane, et. al., 1978) that monoliths can be made by carefully drying gels. The promise of a structurally solid and useful glass produced at room temperature proved to be more dream than reality, and monoliths remain the least important sol-gel products (Brinker and Scherer, 1990).

Sol-gel systems have been made by a diverse array of inorganic and metalorganic precursors including transition metal esters and salts, aluminates, borates, and silicates. Silicates are the single most common precursors, and alkoxides, in general, are used more than any other starting material for the sol-gel process. The general usefulness of alkoxides results from their reactivity with water; the partially hydrolyzed alkoxides can then react together to form dimers, chains, and rings through condensation reactions which free additional water and allow further hydrolysis (Brinker and Scherer, 1990)

GROUP IV TRANSITION METAL ALKOXIDE SYSTEMS

The sol-gel process proceeds through the effect of hydrolysis, alcoxolation, olation, oxolation, alkoxy bridging, and other nucleophilic association mechanisms. Due to the lower electronegativity of these transition metals, the group IV transition metal alkoxides are more susceptible to hydrolysis and condensation than silicon alkoxides.

The suggested mechanisms for these reactions have been summarized in Figure 1 (Brinker and Scherer, 1990). At this point, it should also be noted that olation, as shown in Figure 1, only occurs when the coordination number of the metal has been expanded beyond its oxidation number.

1.4. METAL ALKOXIDES

It has already been noted that industrial applications of metal alkoxides (also named as metal esters) include sol-gel processing of ceramic and metalorganic powders, films, and fibers. However, these important metalorganic compounds are also used as cross-linking agents and catalysts for a variety of organic reactions. Of the group IV transition metal alkoxides, the titanates have undoubtedly been used most frequently for catalysis. Esters and polyesters (Weber, 1962; Jaruzelski and Sheppard, 1963; Stevens and Gardner, 1965; Case,1968; Marzocchi,1972; Haslam, 1958; and Temin and Baum, 1967), polysiloxanes (Gaillissen and Gancberg, 1956; Madaras, 1958; Kohn and Guez, 1961; Hartlein and Olson, 1972; Rauner and Tyler, 1962), polyolefins (Anderson et. al., 1958; Arnold and Foster, 1960; Coover, 1960; Dawes and Winkler,1964; Sianesi and Caporiccio, 1966; Orzechlowski and MacKenzie, 1967; Hogan and Witt, 1971; Hiroyuki, 1972), polyformamide (Beek and Pijpers, 1972), polycarbonate (Reynolds and Dunham, 1972), and polyurethanes (Lawham, 1965; Smelts, 1969) have all been made via titanate catalyzed reactions (Du Pont, TYZOR Bulletin).

The catalysis of ester formation from alcohols and carboxylic acids plays an important role in the processing of coating materials derived

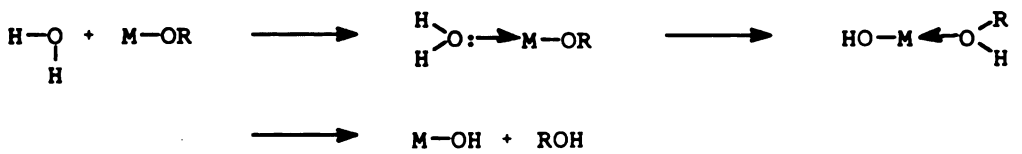

hydrolysis

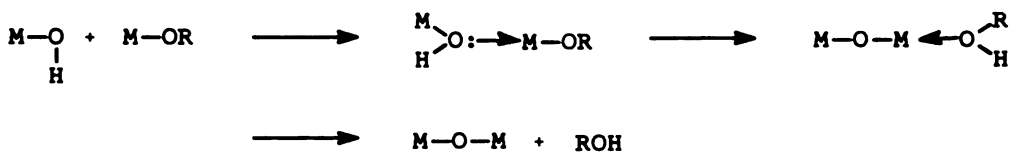

alcoholysis

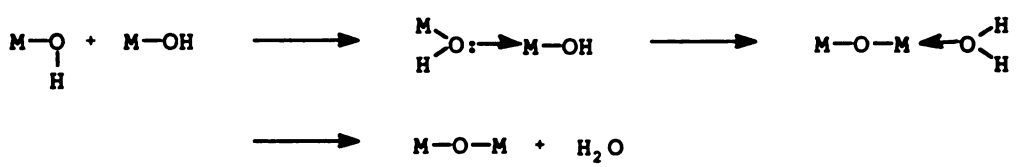

oxolation

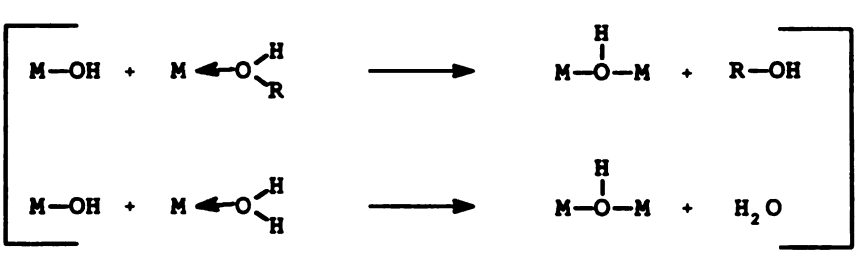

olation

Figure 1. Sol-gel reaction mechanisms (Brinker and Scherer, 1990).

from metal alkoxide carboxylates. It is especially important to note that along with the ester, water is generated which can further hydrolyze the metalorganic titanium.

Many group IV 'd' block transition metal alkoxides can be produced by reacting the metal chloride with an alcohol in the presence of ammonia:

$$MCl_4 + 4\,HOR + 4\,NH_3 \longrightarrow M(-OR)_4 + 4\,NH_4Cl.$$

One or more of the alkoxy groups can be changed on an alkoxide by an alcoholysis reaction which is often employed to synthesize alkoxides with long or bulky alkoxy groups; alkoxy groups can also be switched by transesterification, in which the new alkoxy group is supplied by an organic ester rather than a alcohol. The overall effect of alcoholysis,

$$M(-OR)_4 + HOR' \longrightarrow (R'O-)M(-OR)_3 + 4\,HOR,$$

or,

$$M(-OR)_4 + 4\,HOR' \longrightarrow M(-OR')_4 + 4\,HOR,$$

can be equivalent to the effect of transesterification:

$$M(-OR)_4 + 4\,CH_3COOR' \longrightarrow M(-OR')_4 + 4\,CH_3COOR.$$

When used in alkoxide synthesis, alcoholysis or transesterification is generally driven to completion by removing the product alcohol or ester by azeotropic distillation in an organic solvent. However, it is important to realize that these reactions take place to some degree whenever alcohols or esters are mixed with an alkoxide.

In comparing the isopropoxides of titanium, zirconium, and hafnium, it should be noted that the titanate is a liquid at room temperature,

whereas the zirconium and hafnium isopropoxides are solids. Among tertiary alkoxides, volatilities increase in the order Ti < Zr < Hf; due to the bulkiness of their alkoxy groups, these compounds exist as monomeric species -- showing a drastic reduction in the tendency toward coordination expansion and bridging associations (Bradley et. al., 1952 (b)). Normal alkoxides (Bradley et. al., 1953) and shorter chain secondary alkoxides (Bradley et. al., 1952 (c)) show higher values of molecular complexity (degree of oligomerization). The boiling points and degree of molecular association are shown in Table 3 for several alkoxides:

Table 3. Boiling points and degree of molecular association.

Alkoxide	Boiling point $^{o}C/5$ mm	Molecular Association
$Ti(OEt)$	138.3	2.4
$Ti(OPr^{i})$	91.3	1.4
$Ti(OBu^{t})$	93.8	--
$Ti(OAm^{t})$	142.7	1.0
$Zr(OEt)$	234.8	3.6
$Zr(OPr^{i})$	203.8	3.0
$Zr(OBu^{t})$	89.1	1.0
$Zr(OAm^{t})$	138.4	1.0

(Mehrotra, 1967)

When comparing alkoxides to determine the effect of the central metal on molecular complexity, zirconium and hafnium were found to produce a greater tendency toward oligomer formation than titanium. This was attributed to the larger size and maximum covalency of the heavier atoms since the oxygen-metal intermolecular binding is thought to be quite similar for these metals (Bradley et. al., 1953). The characteristics of the titanium, zirconium, and hafnium alkoxides have been studied and

reviewed by Bradley and coworkers in several early sources (Bradley and Wardlaw, 1951; Bradley et. al., 1952 (a, b, c), 1953, and 1978). Excellent reviews by Mehrotra (1967) and Livage and coworkers (1988) also contribute to this area.

1.5. METAL CARBOXYLATES

Metal carboxylates are also known as soaps. Titanium, zirconium, and hafnium carboxylates can be produced by reacting the carboxylic acid anhydrides with an appropriate metal alkoxide (Mehrotra, 1967). Generally, tetrasoaps cannot be obtained from the reaction of a carboxylic acid with these alkoxides because of the tendency to form oligomers. As alcohol is liberated, an ester and water are formed which initiates the oligomer formation. In the case of titanium, oxide-carboxylates tend to ultimately result from this reaction (Mehrotra, 1967).

Zirconium tetrasoaps can also be derived from the reaction of the metal chloride with a carboxylic acid. Since the carboxylates are bidentate ligands, the zirconium is expected to be eight coordinate. When allowed to react with zirconium isopropoxide, carboxylic acids produce a dimer by the following reaction (Mehrotra, 1967):

$$2Zr(OPr^i)_4 + 7RCOOH \rightarrow (RCOO)_3ZrOZr(OOCR)_3 + 7Pr^iOH + RCOOPr^i$$

Some interesting zirconium IV carboxylate complexes include $Zr(O_2CR)_4$, $ZrO(O_2CR)_2(H2O)_X$, and $ZrO(OH)(O_2CR)(H_2O)_X$. Not surprisingly, the

solubility decreases in water and increases in hydrocarbons as the alkyl chain-length increases (Mehrotra, 1983).

Evidently, Ti(IV) tetracarboxylates do not form easily since a large number of attempts to synthesize them had failed before success was eventually attained. Several mixed carboxylates have also been isolated: $(o\text{-}OC_6H_4CO_2)Ti(OPr^i)_2$, $(o\text{-}HOC_6H_4CO_2)_2Ti(OPr^i)(O_2CR)$, and $(o\text{-}HOC_6H_4CO_2)Ti(OPr^i)(O_2CR)_2$, where R=$C_{11}H_{23}$, $C_{15}H_{31}$, and $C_{21}H_{43}$. Heterocyclic Ti(IV) carboxylates have also been reported having a structure described by: $(Pr^iO)_{4-n}TiL_n$, where n=1-3 (Mehrotra, 1983). Both Ti(II) and Ti(III) carboxylates also exist, and many of these compounds are darkly colored (Mehrotra, 1983).

1.6. ALCOHOLS, CARBOXYLIC ACIDS, AND ESTERS

The reactions used to generate the alkoxide carboxylate coating solutions involve, as reactants or products, several organic compounds. These compounds are alcohols, carboxylic acids, and esters, and some of their important properties should be discussed.

It is commonly known that in aqueous solution the acidity of an alcohol decreases as the alkyl chain length increases. Although this phenomenon has been incorrectly attributed to an inductive effect in some older organic chemistry textbooks, it can more properly be explained by differences in the solvation energy of the anion. In dimethyl sulfoxide, a poor solvating agent for anions, the acidities are equivalent (Allinger et. al., 1976). It is also interesting to note the intrinsic acidity of alcohols in the gas phase shows that the acidity increases slightly with the length of the alkyl chain (Brauman and

Blair, 1968). A similar trend can be observed among carboxylic acids. The intrinsic acidity in the gas phase increases from acetic to propionic to butyric acid. While, in aqueous solution, acetic acid is strongest and propionic acid is weakest among the three acids (Jen and Thomas, 1975; Yamdagni and Kebarle, 1973). Furthermore, it is important to note that the insoluble metalorganic coating solutions are predominantly solvated by excess carboxylic acid and are not expected to act like aqueous solutions.

The structures, names, and boiling points of some common alcohols, carboxylic acids, and esters have been given in Table 4. The boiling

Table 4. Structures and normal boiling points for selected alcohols, carboxylic acids, and esters.

Name	Structure	Normal Boil Point
Methanol	CH_3OH	64.7
Ethanol	CH_3CH_2OH	78.3
n-propanol	$CH_3CH_2CH_2OH$	97.2
iso-propanol	$CH_3CH(OH)CH_3$	82.3
n-butanol	$CH_3(CH_2)_3OH$	117.7
iso-butanol	$(CH_3)_2CHCH_2OH$	107.9
sec-butanol	$CH_3CH_2CH(OH)CH_3$	99.5
t-butanol	$(CH_3)_3COH$	82.5
acetic acid	CH_3COOH	118.
propionic acid	CH_3CH_2COOH	141.
butyric acid	$CH_3(CH_2)_2COOH$	163.
valeric acid	$CH_3(CH_2)_3COOH$	187.
hexanoic acid	$CH_3(CH_2)_4COOH$	205.
octanoic acid	$CH_3(CH_2)_6COOH$	237.
n-propyl acetate	$CH_3COOCH_2CH_2CH_3$	101.6
iso-propyl acetate	$CH_3COOCH(CH_3)_2$	88.4
n-propyl n-valerate	$CH_3(CH_2)_3COOCH_2CH_2CH_3$	167.5
iso-propyl n-valerate	$CH_3(CH_2)_3COOCH(CH_3)_2$	--------

Data on alcohols and carboxylic acids taken from Allinger (1976); data on esters taken from Lange's Handbook of Chemistry, 11th ed. (1974).

points of the alcohols, carboxylic acids, and esters are of general importance to the synthesis of metal alkoxide carboxylates and polyalkoxoacylates because the unwanted reaction products and excess reactants are often removed by distillation. In our work, however, the metalorganic coatings were produced at ambient temperatures and no side products were removed.

1.7. METAL ALKOXIDE CARBOXYLATE DERIVED COATINGS

Among group IV transition metal alkoxide carboxylates, Ti complexes have been studied the most. Two Du Pont patents describe the chemistry involved when the carboxylic acids are mixed with the titanium alkoxides and allowed to react extensively, with or without the addition of water (Feld and Cowe, 1965). Without the addition of water, sufficient reaction leads to metalorganic polymers with 1, 3/2, or 2 carboxylate groups per titanium atom (Langkammerer, 1952):

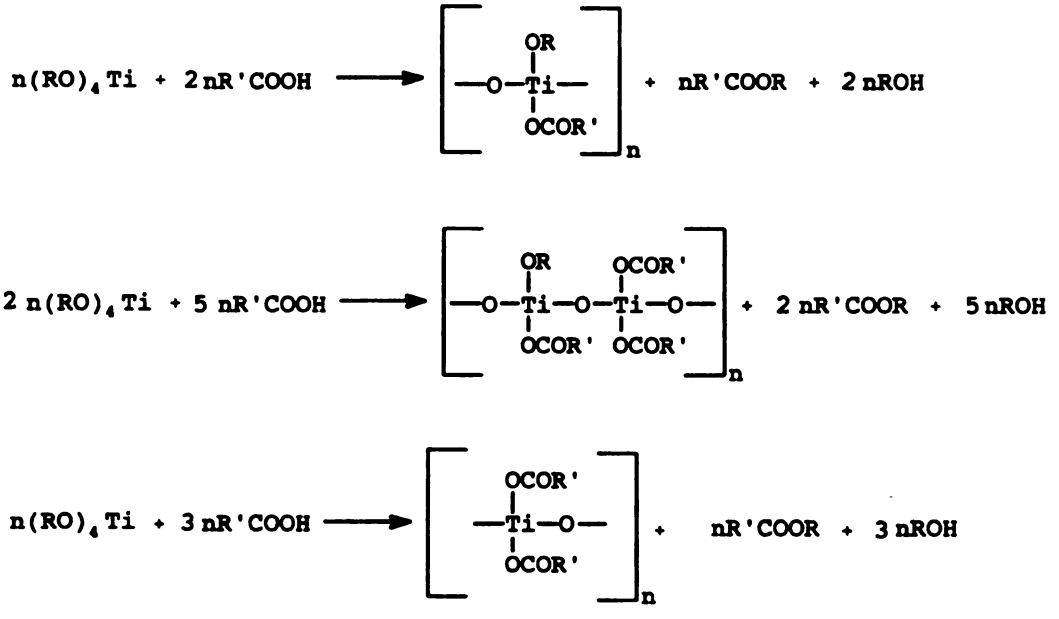

The ratio of the combined reactants determines the number of isopropyl groups to be replaced with carboxyl groups. With the addition of a sufficient quantity of water, only one carboxyl side group is retained per titanium atom and the isopropyl groups are replaced by hydroxyl groups (Haslam, 1952):

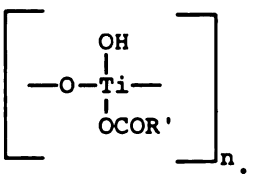

In both patents, higher chain-length carboxylic acids are preferred and the waxy products are soluble in organic solvents. When films are cast from these materials, the coating is transparent but soft. The films are easily scratched.

The interaction of titanium alkoxides with acetic acid has received special attention due to the interest in using the products as a TiO_2 coating precursor. These films have limited utility in direct applications requiring the unfired film to contact water or organic solvents; however, the films can be used with dry gases. Films made from alkoxide acetates are ideal for applications requiring easily removable or soluble membranes. The formation of these materials are often treated in the context of sol-gel chemistry in which the acetic acid is regarded as a modifier of the metal alkoxide precursor (Livage, 1986; Doeuff, et. al.,1987; Livage, et. al., 1990; Sanchez, et. al., 1988 (a, b) and 1990, Sanchez and Livage, 1990). The acetic acid expands the coordination number of the Ti to 5 and 6, where the acetate groups act as bridging and chelating bidentate ligands (Sanchez, C., et. al., 1988 (a)). Sanchez and coworkers postulate the formation of the

$Ti(OR)_4(AcOH)$ transition state from the nucleophilic addition of the acid followed by the subsequent removal of an alcohol molecule, leaving $Ti(OR)_3(OAc)$ (Sanchez et. al., 1988 (a)). The presence of acetic acid favors polycondensation rather than particulate sol formation. Since the alcohol group is more easily removed by hydrolysis than the acetate group, a greater number of acetates leads to a slower rate of hydrolysis. The first stage of hydrolysis may remove -OR groups while the second stage breaks bridging acetate bonds to form chelating bidentate and monodentate ligands. The final stage of hydrolysis would leave only -OH groups and monodentate acetate groups on the polymer backbone (Doeuff, et. al.,1987).

The formation of complex oxo-alkoxides also proceeds from the reactions of alkoxides and acetic acid. These oxo-alkoxides are thought to develop as side-reaction byproducts which do not participate in the polymerization process (Sanchez et. al., 1990). One such structure which has been isolated and crystallized from the reaction of Ti isopropoxide and acetic acid is $Ti_6(\mu\text{-}O)_2(\mu_3\text{-}O)_2(\mu_2\text{-}OAc)_4(\mu_2\text{-}OPr^i)_4(OPr^i)_6$. This compound is believed to originate from the $Ti_3O(OPr^i)_9(OAc)_3$ trimer which is then believed to release a CH_3COOPr^i molecule leaving $Ti_3(OPr^i)_8(OAc)_2$. The further removal of a $-OPr^i$ by hydrolysis would then be followed by oxolation in which two $Ti_3(OPr^i)_7(OAc)_2OH$ species combine to release two isopropanol molecules and the final oxo-alkoxide product (Sanchez, et. al., 1990). The structure of the product is shown in Figure 2. These studies demonstrate the type of chemistry which can be involved in alkoxide and carboxylic acid reactions.

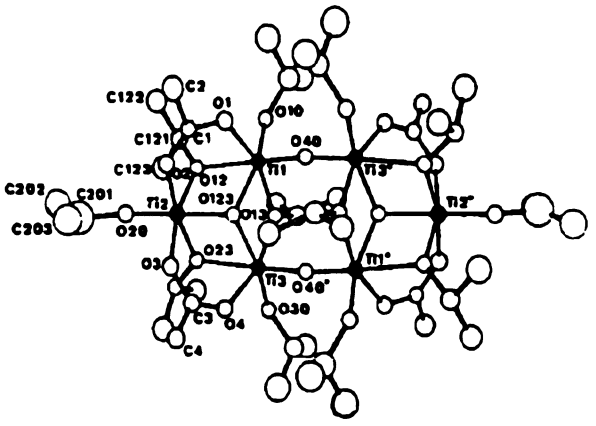

Figure 2. The structure of $Ti_6(\mu\text{-}O)_2(\mu_3\text{-}O)_2(\mu_2\text{-}OAc)_4(\mu_2\text{-}OPr^i)_4(OPr^i)_6$.

1.8. COATING METHOD

The coating solutions are applied to dry, chemically cleaned glass or quartz (Micro cleaning solution) and spun dry at approximately 1100 rpm. This spin-coating technique has been used to produce excellent films from valeric and butyric acid-based coating formulations, as previously described (Gagliardi, et. al., 1990).

In general, spin-coating is often used to make thin films from sol-gel materials, and a basic review of the technique is given in Sol-Gel Science (Brinker and Scherer, 1990).

CHAPTER 2.

MEMBRANES: REVIEW OF BACKGROUND INFORMATION

In very broad terms, "membrane" refers to a "region of discontinuity interposed between two phases" (Hwang and Kammermeyer, 1975). In this very general sense, polymer films cast onto a solid substrate may be considered membranes, regardless of the permeability of the substrate. However, it should be understood that membranes are usually applied between two phases to act as semipermeable barriers to a species which could permeate both phases (Hwang and Kammermeyer, 1975); one usually speaks of permeation 'through' a membrane and not merely 'into' the membrane material. Membranes applied to highly impermeable and rigid substrates do offer many advantages when studying the properties of the membrane material, which is usually very thin and fragile. Diffusion into a film bounded by an impermeable barrier is relatively easy to model, and the membranes are much easier to work with when attached to a rigid substrate (Hwang and Kammermeyer, 1975).

2.1. PERMEATION OF SOLUTES

When a membrane contacts a solution surface, the bulk solution differs from that in immediate contact with the membrane, known as the boundary layer. Diffusion through boundary layers, and adsorption and desorption of solute on the membrane surface can lead to high boundary layer resistance in liquid solutions. Defining a phenomenological

permeability provides a means of expressing the overall permeation in terms of measurable, bulk variables. The only difficulty with this approach is that the permeability is not a property of the membrane, but of the membrane-solvent-solute system. The membrane-solution interfaces are shown in Figure 3 for a membrane between two solutions. The presence of the boundary layer resistance reduces the concentration gradient within the membrane. Γ and C refer to bulk and membrane concentrations, respectively (Hwang and Kammermeyer, 1975).

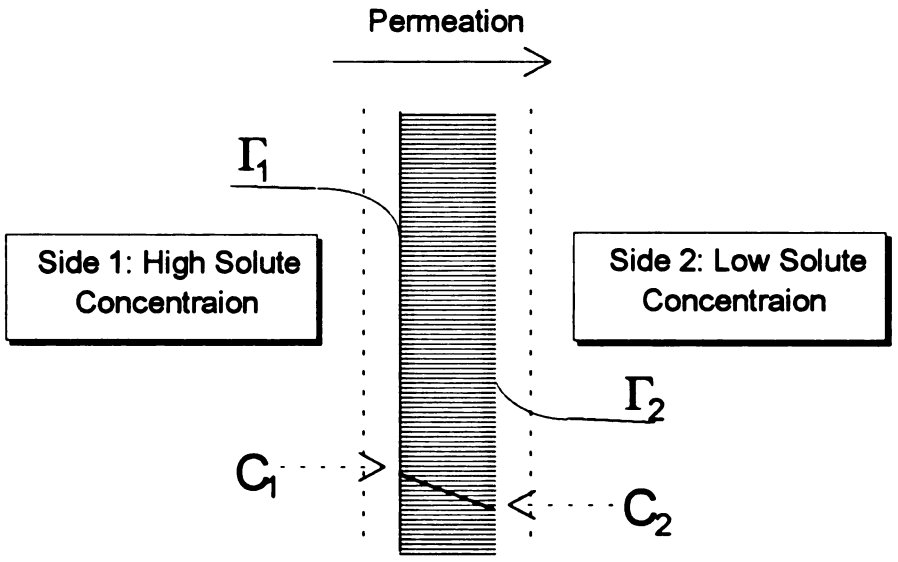

Figure 3. Concentration gradients through membrane and boundary layers.

In general terms, transport through a membrane is driven by differences in chemical potential (μ), electrical potential, temperature, and pressure (Lakishminarayanaiah, 1969). However, many processes appear to be dominated by changes in chemical potential and pressure. For the case of a thin membrane applied to an impermeable

substrate, transport of an uncharged solute within a liquid solution will be primarily a concentration-driven process. Electric field, temperature (Soret), and pressure effects can all be ignored (Lakishminarayanaiah, 1969). The boundary layer resistance and Fickian diffusion through the membrane are all that is needed in general, and in films with very high diffusion resistance, the boundary layer resistance can also be ignored (Lakishminarayanaiah, 1969). However, in rigorous membrane calculations, the expressions of Fick's laws must account for the presence of the membrane. The following two equations rigorously describe Fickian diffusion through membranes (Hwang and Kammermeyer, 1975):

$$N_A = -D\frac{\partial C_A}{\partial x} - \frac{D}{2C_M}\frac{\partial C_A^2}{\partial x} \tag{1}$$

$$\frac{\partial C_A}{\partial t} = \frac{\partial}{\partial x}\left(D\frac{\partial C_A}{\partial x}\right) + \frac{\partial}{\partial x}\left(D\frac{C_A}{C_M}\frac{\partial C_A}{\partial x}\right) \tag{2}$$

where

- N_A = permeation flux for A
- D = diffusion coefficient
- C_A = concentration of A
- C_M = concentration of membrane
- t = time
- x = position (in direction of diffusion)

In cases where C_M is relatively large and C_A is very small, the second term in each equation may be legitimately ignored .

Two aspects of a membrane appear to be critical to almost any application: structure and morphology, and chemical composition of the surface (Kesting, 1985).

2.2. STRUCTURE

Most membranes are heterogeneous in structure (Lakishminarayanaiah, 1969). The heterogeneity can result from preferential orientation of molecular functional groups, uneven pore distribution and shape, and intentionally asymmetric composite construction (Paul and Morel, 1978). Several structures are shown in Figure 4 (Paul and Morel, 1978).

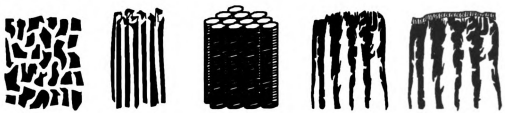

Figure 4. Sample membrane structures: (a) sponge-like, isotropic; (b) approximate co-axial capillary; (c) co-axial capillary; (d) anisotropic; (e) skinned, composite.

Many membrane materials have a sponge-like structure (Paul and Morel, 1978), shown in Figure 4(a), as opposed to the co-axial capillaries, Figure 4(b,c), found in certain ceramic membranes, in polymer films treated by radioactive bombardment, and in ionotropic gel membranes (Paul and Morel, 1978). The diameters can remain relatively constant

throughout the membrane for isotropic structures, Figure 4(a,b,c), or they can increase dramatically from one surface to the other, providing an anisotropic structure as shown in Figure 4(d,e). Composite membranes are also widely used; many incorporate a very thin, small-pore skin applied to the surface of a larger-pored material as shown in Figure 4(e) (Paul and Morel, 1978).

The thickness of the membrane and the size distribution and structure of the pores strongly determine the pressure required to force a particular fluid through the membrane in a pressure driven process. The pore-size distribution also effects diffusion rates and solute size selectivity (Lakishminarayanaiah, 1969).

Membrane materials are often classified as porous or non-porous materials. However, it must be understood that 'non-porous' is not meant in a completely literal sense. Many dense, 'non-porous' metallic or ceramic materials may have a considerable number of pores in the size range of 5-10 Å (Hwang and Kammermeyer, 1975), and virtually all dense polymeric membranes have some porosity; yet, the total volume occupied by pores in these materials is relatively small. A membrane is typically considered porous only when the microvoids begin to interconnect, usually requiring void fractions of about 50% (Kesting, 1985). In membrane separation processes, 'ultrafiltration' designates filtration of species in the 10-1000 Å range while 'microfiltration' filters species between 1000 Å and 10 μm (Mohr, et. al., 1989). These membranes are microporous materials, with effective pore sizes smaller than the filterable species. Knowing the pore size and structure of a membrane is essential to mathematically modeling the permeation of a species through the membrane, since different transport phenomenon will

predominate under different conditions (Kesting, 1985; Lakishminarayanaiah, 1969).

2.3. CHEMICAL COMPOSITION

When transport is induced by changes in chemical potential, the process is frequently referred to as "concentration driven." It is important to note that the chemical composition of the membrane surface affects the adsorption and desorption of the solute, which strongly affects the boundary layer resistance and the chemical potential gradient within the membrane (Hwang and Kammermeyer, 1975). Sourirajan, a codeveloper of the Loeb-Sourirajan desalination membrane, stresses the importance of adsorption at the membrane surface. For a good desalination membrane which passes purified water, the water is strongly adsorbed while the solute is negatively adsorbed or repelled from the surface (Loeb and Sourirajan, 1981).

2.4. GUEST-HOST MEMBRANES

These are a class of membranes distinguished by the non-covalent bonding of solute molecules (guests) into cavities or sites (hosts) within the membrane. These membranes are of importance because they mimic the ability of biological membranes and enzymes to gather reactants together in specific microenvironments (Fendler, 1982). Several systems exemplify this behavior. Linear and macrocyclic polyethers can host cationic guests, and cyclodextrins can host aromatics, amino acids, nucleotides, small ions, and gases (Fendler, 1982).

CHAPTER 3.

PORPHYRINS: REVIEW OF BACKGROUND INFORMATION

Porphyrins have been studied extensively. Many molecules of this class occur in nature, while others only exist from laboratory synthesis (Dolphin, 1978). Some basic information on porphyrins, especially iron porphyrins, is essential for understanding many of the problems associated with this project.

3.1. BASIC NOMENCLATURE

PYRROLES

Pyrroles are basic structures from which porphyrins can be formed, and reference is often made to the four pyrrole rings of the porphyrin molecule. Several pyrrole structures and the ring numbering system are shown in Figure 5. The molecules 1-pyrroline and pyrrolidine are samples of reduced pyrroles (Bonnett, 1978).

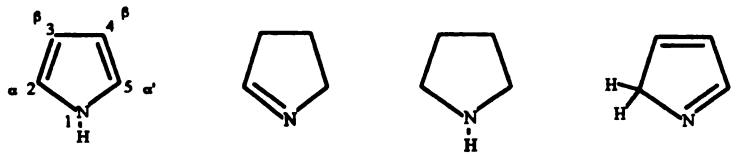

pyrrole 1-pyrroline pyrrolidine 2H-pyrrole

Figure 5. Pyrrole ring structures.

FISHER NOMENCLATURE

Parent Systems

Of the many parent systems used in Fisher nomenclature, only the porphine and chlorin structures will be described. These structures are numbered as shown in Figure 6.

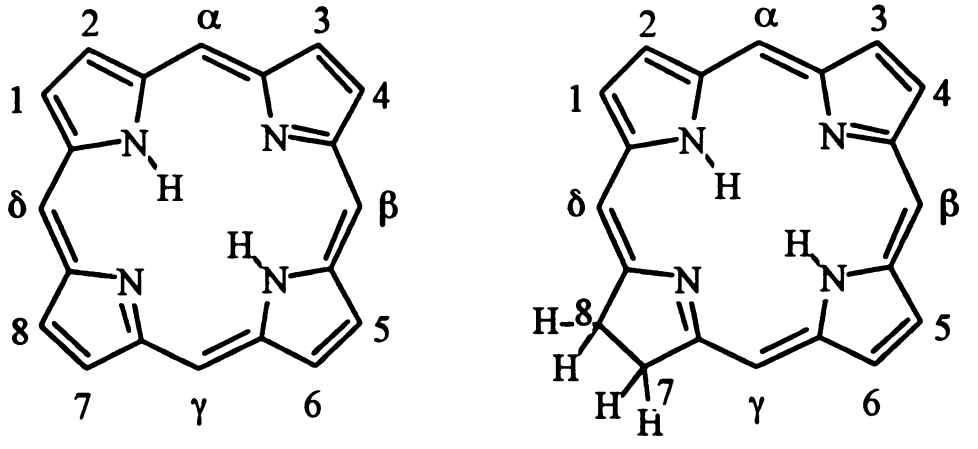

Porphine Chlorin

Figure 6. Porphine and chlorin parent systems for Fisher nomenclature (Bonnett, 1978).

Type Nomenclature

The type nomenclature uses Roman numerals to designate the various isomers which are possible for some simple substituted-porphyrin systems. To simplify the presentation of the structures, a shorthand notation is employed which shows only the β-β' bonds on the four pyrrole rings with all substitution occurring at the 3 and 4 positions of these pyrrole rings (Bonnett, 1978).

The most basic case of this nomenclature occurs when there are two different substituents, one of each on each pyrrole ring, resulting in four unique isomers (Bonnett, 1978):

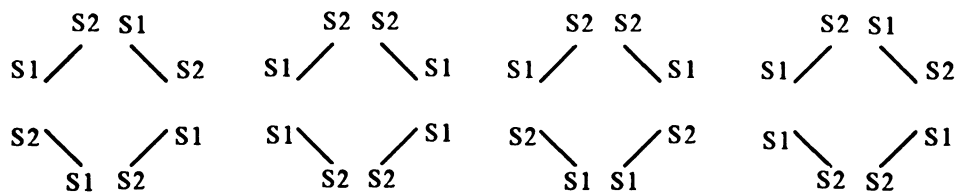

The next case involves three different substituents, S1, S2, and S3. Each pyrrole ring has one of type S1; two of the four pyrrole rings each have one of type S2, and the remaining two positions have type S3. This arrangement leads to 15 unique structural isomers. The structures for this and other increasingly complex systems have been described by Bonnett (1978).

A REVISED NOMENCLATURE

The many parent structures of the Fisher system are replaced by a single parent system which is shown in Figure 7. In this nomenclature, porphine is renamed porphyrin and a new numbering system is introduced (Bonnett, 1978).

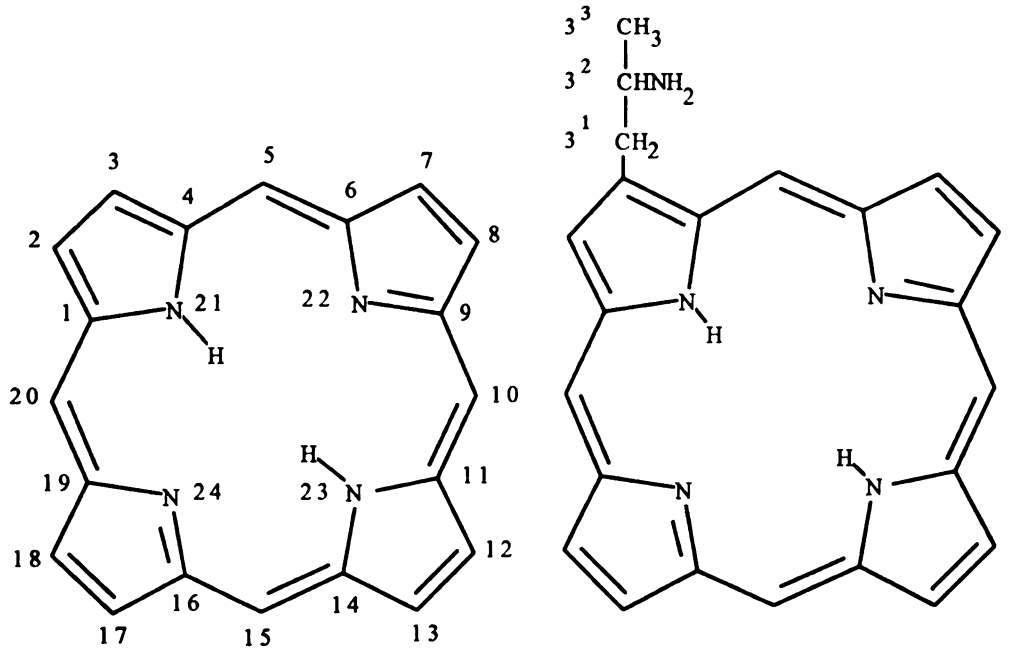

Figure 7. The porphyrin parent system: (a) porphyrin substitution assignments, and (b) side-chain numbering (Bonnett, 1978).

The type nomenclature for isomers is only retained for the base case systems with only two substituents. The trivial name for the most important isomer of a more complex system is still acceptable in some cases, but the Roman numerals are discarded; the less important isomers should be described relative to the parent system to avoid confusion (Bonnett, 1978). If the chlorin were to be named relative to the parent porphyrin system, it would be called 17,18-dihydroporphyrin (Bonnett, 1978).

3.2. IRON PORPHYRINS

Iron porphyrins have retained an extensive trivial nomenclature, and the recommended usage does not always agree with the historical

names. For example, the term 'heme' has been recommended for an iron porphyrin complex of unspecified oxidation state (Bonnett, 1978), and yet the term historically refers to only Fe(II) complexes (Buchler, 1978). To avoid unnecessary confusion, special comment will be made whenever an ambiguous term is used.

RECOMMENDED USAGE OF TRIVIAL NAMES

The revised nomenclature for iron porphyrin complexes includes the terms described in Table 5. The ferro- and ferri- prefixes are intended to unambiguously describe the oxidation state of the iron, and the -ochrome suffix specifies the low-spin state; hemin and hematin are names given to two important classes of ferrihemes (Bonnett, 1978). Guidelines governing the application of IUPAC rules to metalloporphyrins have also been described by Bonnett (1978).

Table 5. Trivial names for iron complexes in the revised nomenclature.

Term	Description of porphyrin complex
Heme	Iron porphyrin
Ferroheme	Fe(II) porphyrin
Ferriheme	Fe(III) porphyrin
Hemin	Chloro(porphyrinato) Fe(III)*
Hematin	Hydroxo(porphyrinato) Fe(III)*
Hemochrome	Low-spin iron porphyrin with one or more strong field ligands.
Ferrohemochrome	Fe(II) hemochrome
Ferrihemochrome	Fe(III) hemochrome

*Note: when the porphyrin is described as an anionic ligand, it is given the name porphyrinato.

IMPORTANT CHARACTERISTICS

Ferrohemes (Fe(II) Porphyrin Complexes)

These molecules have a d^6 electronic configuration, and can have 0, 1, or 2 axial ligands (L) (Buchler, 1978). Except for the case in which two ligands have equal π-acceptor characteristics, these complexes are known historically as 'hemes' which can be subdivided into three categories: 'bare', square pyramidal, and hexacoordinate. 'Bare' hemes, as the name implies, are Fe(II) complexes with no ligands. Their configuration is simply Fe(P), where P represents the porphyrin. They are the most reactive of the 'hemes' and react irreversibly with dioxygen, normally yielding hematin-type, μ-oxo complexes (oxygen acts as bridging ligand) (Buchler, 1978). Square pyramidal hemes are ferrohemes which have a single axial ligand, Fe(P)L. Hexacoordinate hemes have two ligands attached to the Fe(II) porphyrin complex which must have very different π-acceptor characteristics, and thus can be designated as L and L' (Buchler, 1978).

Ferrohemochromes are low-spin ferrohemes which have one or more strong field axial ligands. When there are two, equal donor ligands, these complexes are historically called 'hemochromes' (Buchler, 1978).

Ferrihemes (Fe(III) Porphyrin Complexes)

In the presence of dioxygen, ferrohemes readily oxidize to ferrihemes. Thus, iron porphyrins are often stored as ferrihemes and reduced in-situ to ferrohemes only when the Fe(II) complex is needed. Ferrihemes have a d^5 electronic configuration. Two important types of

iron porphyrins within this category are hemins and hematins (Buchler, 1978).

Hemins are chloro(porphyrinato) Fe(III) complexes, Fe(III)(P)Cl. The term 'hemin' historically included complexes with univalent anion adducts (X) other than just Cl^-, having the general form Fe(III)(P)X (Buchler, 1978).

A hematin refers to a hydroxo(porphyrinato)Fe(III) complex, usually isolated as a binuclear, μ-oxo complex of the form $[Fe(P)]_2O$. The traditional usage of this term refers to the same binuclear complexes (Buchler, 1978).

METHODS OF REDUCTION

Many reducing agents are satisfactory for reducing the iron without also reducing the porphyrin ring. The porphyrin must be thoroughly deoxygenated prior to reduction. Direct reduction involves adding the reducing agent to the deoxygenated metalloporphyrin solution (Falk and Smith, 1975). An alternative method of reduction involves adding only trace amounts of photoactive initiator which can generate a suitable reducing agent upon exposure to UV light (Ward and Chang, 1982).

Hydrazine (Chang, 1992) and sodium dithionite (Falk and Smith, 1975) are soluble in aqueous solution and can be used for the direct reduction of water soluble porphyrins. Benzophenone or acetophenone, used in conjunction with isopropanol, are useful in the photoreduction of nonaqueous or aqueous ferriheme solutions, respectively (Ward and Chang, 1982).

PORPHYRIN RING SUBSTITUENTS

The substituents on the outer positions of the porphyrin ring can strongly influence the behavior of the porphyrin. They affect both the solubility of the molecule and the strength of the porphyrin-metal bonds (Buchler, 1978). Electron withdrawing substituents increase the π-acceptor capacity of the porphyrin, increasing the stability of the metalloporphyrin complex (Buchler, 1978). This is especially important when photoreduction is used to generate the ferroheme complex, since UV light can cause demetallation (Buchler, 1978).

CO LIGANDS

Increased π-bonding between the metal and the porphyrin ring due to electron-withdrawing substituents decreases the π-bonding between the metal and any carbonyl ligands. Thus, the CO ligands become more labile as electron-withdrawing substituents are added to the outer ring of the ferroheme. This is exemplified by comparing basic tetraaryl and octaalkyl ferrihemes: the CO is more labile on the tetraaryl complexes due to the increased π-bonding between the metal and the porphyrin ring (Buchler, 1978).

MEMBRANE APPLICATIONS

Porphyrins have been used to study energy and electron transfer and charge separation in reversed micelles. Zn-tetramethyl pyridinium porphyrin sensitized electron transfer with diphenylthiol as the electron donor. The porphyrins act as reduction catalysts. The

photoreduction of protoporphyrin has also been studied in monolayers (Fendler, 1982).

Another application involved the photoejection of CO from Ru(II) and Os(II) complexes within a monolayer membrane. Dimerization and Cu^{2+} insertion studies have been performed in monolayer assemblies for a number of porphyrins (Fendler, 1982).

3.3. SPECTROSCOPY OF PORPHYRINS

Electronic adsorption spectroscopy is a sensitive technique which is often applied in the characterization of porphyrins. Infrared adsorption and Raman scattering spectroscopies are also used in porphyrin characterization. However, due to the abundance of strong, infrared-active transitions, subtle changes in the porphyrin may be difficult to detect and interpret. When Raman scattering is performed using an excitation wavelength which coincides with a significant electronic absorption band, the Raman signal is selectively intensified by a factor of 10^3-10^4 due to the coupling between the electronic and vibrational transitions; this enhanced Raman scattering technique is known as resonance Raman spectroscopy, and it has proven to be a very powerful technique in porphyrin characterization (Felton & Nai-Teng Yu, 1978).

UV-VIS ABSORPTION

Regular Porphyrins

In metalloporphyrins, the lowest energy π-π^* exited singlet transition and its associated vibronic envelope create the two Q-bands

which occur in the visible region between 500-600 nm. The letter 'Q' denotes quasi-allowed transitions. The lower energy band is labelled α or Q(0,0), and the higher energy band, which includes one mode of vibrational excitation, is β or Q(1,0) (Gauterman, 1978). The Soret band, a highly intense band which occurs in the violet region between 380-420 nm, corresponds to the second excited singlet state. This is the primary B-band, B(0,0). The vibronic envelop occurs about 1250 cm^{-1} further to the blue and is designated B(1,0). The letter 'B' denotes a band for a highly allowed transition (Gauterman, 1978). There are also several weak bands, denoted N, L, and M, which occur at slightly higher energies than the Soret band (Gauterman, 1978).

Freebase porphyrins have a lower degree of symmetry, resulting in two primary Q-bands designated $Q^x(0,0)$ and $Q^y(0,0)$, each with a vibronic envelope. In order of increasing energy, the four bands are $Q^x(0,0)$, $Q^x(1,0)$, $Q^y(0,0)$ and $Q^y(1,0)$ (Gauterman, 1978).

Irregular Porphyrins

There are two categories of irregular metal porphyrins: hypsoporphyrins and hyperporphyrins. The optical properties of normal porphyrins are predominantly determined by the π electrons of the porphyrin ring. For irregular porphyrins, there is extensive interaction between the porphyrin ring π electrons and the electrons of the metal and its ligands. Such interaction of electrons complicates the porphyrin spectra and their interpretation (Gauterman, 1978).

Hypsoporphyrins have UV-VIS spectra which are qualitatively like the spectra of normal porphyrins except that the features are shifted to

lower wavelength or 'blue-shifted'. This irregularity is caused by a stronger metal perturbation on the π-π^* transitions (Gauterman, 1978).

Hyperporphyrins are distinguished by the presence of extra bands in the electronic absorption spectra, at wavelengths greater than 320 nm, which do not originate from π-π^* transitions. Some of these porphyrins may be further distinguished as p-type or d-type, which were collectively known as allo-porphyrins. The characteristic colors of these porphyrins are olive green and brown whereas normal porphyrins are usually red or orange in solution. The extra bands in all hyperporphyrins appear to originate from charge transfer (CT) between the porphyrin ring and the metal (Gauterman, 1978).

The p-type hyperporphyrins are found with the lower oxidation states of the main group metals, e. g., Sn(II), Pb(II), As(III), Sb(III), and Bi(III). These are the most thoroughly understood of the hyperporphyrins, with CT bands corresponding to $a_{2u}(np_z)$(metal) $\rightarrow$ $e_g(\pi^*)$(ring) transitions (Gauterman, 1978).

The d-type occur with transition metals having d^m structure, where $1 \leq m \leq 6$, with holes in the $e_g(d_\pi)$ orbitals and relatively stable lower oxidation states. The CT bands are attributed to $a_{1u}(\pi)$,$a_{2u}(\pi)$(ring) $\rightarrow$ $e_g(d_\pi)$(metal) transitions. Hyper iron porphyrin complexes belong to this category (Gauterman, 1978).

Chlorins

Due to the reduced pyrrole, there is no difference in symmetry between freebase and metalated chlorins; consequently, changes in the spectra due to metallation are less dramatic, and the $Q^x(0,0)$, $Q^x(1,0)$, $Q^y(0,0)$ and $Q^y(1,0)$ bands may all be apparent in both cases.

The absorbance spectra of chlorins are notable for an intense, far-red band. This band may have an intensity even greater than the Soret band. In chlorins, the $Q^y(0,0)$ band has lower energy than the $Q^x(0,0)$ band (Gauterman, 1978).

Iron Porphyrins

Of all metalloporphyrins, iron porphyrins have the most complicated absorption spectra. The spin state, S, can be $\frac{1}{2}$, $\frac{3}{2}$, or $\frac{5}{2}$ for ferrihemes, and 0, 1, or 2 for ferrohemes. The spin state for a given porphyrin can be affected by both the ligand and the solvent. The complexity of the porphyrin-metal interactions is partly due to the existence of d levels with energy comparable to top-filled π and lowest-unfilled π^* orbitals. Both hypso and hyper iron porphyrins exist. The iron hyperporphyrins have $S \neq 0$; the hypsoporphyrins have $S = 0$, a state favored by the presence of carbonyl ligands (Gauterman, 1978).

INFRARED ABSORPTION

Infrared (IR) spectra of porphyrins show a great abundance of peaks which are useful in the identification of substituents. The vibrational absorption band assignments for many porphyrins have been made, and the peak locations for most substituents are well established (Alben, 1978).

The internal bonding in ligands can also be studied with IR spectroscopy. For example, the absorption bands for free CO and for bound CO in deuteroporphyrin IX and protoporphyrin IX dimethyl ester Fe(II) complexes are 2143, 1975.1, and 1976.6 cm^{-1}, respectively. The

shift in the CO absorption band due to complexation is large and fairly consistent for the two ferrohemes (Alben, 1978).

Although IR spectroscopy has been beneficial in certain applications, the general usefulness of the technique is greatly limited by the extreme complexity of the spectra and its poor sensitivity to many subtle changes in the porphyrin. As an analytical tool, electronic absorption has been more widely used in porphyrin characterization (Felton & Nai-Teng Yu, 1978).

RESONANCE RAMAN

Although IR may not be as popular or as easy to use as UV-VIS absorption, the two types of information are very different; the abundance of functional group information provided by vibrational spectroscopy cannot be supplied by electronic absorption (Alben, 1978). When IR is ineffective or undesirable, Raman spectroscopy is often an excellent alternative for acquiring vibrational information. Resonance Raman is even more desirable due to a more easily detected, enhanced signal which contains coupling information not available in normal Raman spectroscopy. The resonance Raman spectra of porphyrins are typically easier to read and interpret than the corresponding IR spectra (Felton & Nai-Teng Yu, 1978).

In addition to the identification of substituents, resonance Raman has also been used to study the aggregation of porphyrins, e. g., chlorophyll a and b. The bonding of ligands to iron porphyrin complexes has also been studied, e. g., the axial stretch for Fe-X in FeOEP(X), where X=F, Cl, or Br (Felton & Nai-Teng Yu, 1978).

CHAPTER 4.

ANALYTICAL TECHNIQUES

4.1. SPECTROSCOPY

Intense UV-vis absorption (Gauterman, 1978) allows the porphyrin to be used effectively as an optically probed recognition species for various ligand-forming compounds such as carbon monoxide. Because this analytical technique is very widely used (Skoog and West, 1980), only a very brief description will be given. As analysis tools, Raman and IR spectroscopies have been very useful in characterizing the coating solution. In this section a brief introduction will be provided for these powerful and complimentary vibrational spectroscopy techniques.

UV-VIS ABSORPTION

Ground state electronic absorption spectroscopy involves transitions from the electronic ground state of a molecular species to various electronic excited states (Skoog and West, 1980). These transitions can also involve changes in the vibrational state of the molecular species, producing 'vibronic' bands (Long, 1977; McQuarrie, 1983). Certain wavelengths of electromagnetic radiation in the ultraviolet and visible (UV-vis) range are absorbed by the sample when they coincide with the energy of the electronic and vibronic transitions of the mole-

cules. Thus, pure electronic transitions and electronic transitions coupled with an excited vibrational state generate the absorption bands which comprise the UV-vis spectrum (McQuarrie, 1983).

INFRARED ABSORPTION

When light is absorbed in the infrared (IR) region, the energy of the absorbed radiation coincides with the energy required for rotational and vibrational transitions (Atkins, 1986). When observing vibrational transitions in fluid samples, the vibrational bands appear broadened by the closely spaced rotational transitions which occur at each vibrational state (Atkins, 1986; McQuarrie, 1983).

IR spectroscopy is widely used in the identification of organic compounds. The various functional groups have characteristic absorption bands which aid chemists in determining the structure of an unknown molecular species (Skoog and West, 1980).

Attenuated total reflectance (ATR) spectroscopy allows an IR absorption spectrum to be taken at the surface of an ATR crystal or internal reflection element (IRE) (Harrick, 1967). The IR light passes through the crystal, being "internally reflected" back and forth between opposing faces. However, with each "internal reflection", the light protrudes slightly from the surface allowing it to sample the external environment. The depth of the light's penetration depends upon the entry angle and the relative indices of refraction for the ATR crystal and the surrounding medium (Harrick, 1967). This is a very useful

technique for examining many samples which would otherwise be difficult to analyze. The theory of ATR spectroscopy and practical information about various ATR configurations can be found in a text by Harrick (1967).

RAMAN AND RESONANCE RAMAN SCATTERING

Raman spectroscopy is still less common than either UV-vis or IR absorption, so it will be discussed in somewhat greater detail. Raman scattering provides information which is qualitatively similar to IR absorption: the bands correspond to rotational and vibrational transitions (Long, 1977). However, some of the transitions which are quantum mechanically allowed for IR absorption are not allowed for Raman scattering, and vice versa. Thus, the two techniques can be regarded as complimentary rather than redundant (Atkins, 1986). This is especially true for simple, centrosymmetric molecules because their selection rules are mutually exclusive; no transition which is active for one of these two spectroscopy techniques is also active for the other (Atkins, 1986).

Raman experiments require a very bright monochromatic light source which is ideally provided by a laser (Akins, 1986; Long, 1977). Fluid samples are usually illuminated with a light beam oriented 90° with respect to the path toward the collection optics; solid samples are often studied in a 180°, backscattering configuration. Typically, the scattered radiation is directed through a scanning monochrometer to a sensitive detector, such as a photo multiplier tube (PMT), connected to a recording device

(Long, 1977). Alternatively, the scattered light is taken through a narrow band pass filter (such as a double monochrometer with gratings in subtractive dispersion), then dispersed to illuminate an optical multichannel array (OMA) detector which can analyze the entire spectral region illuminating its surface (Long, 1977).

The wavenumbers of the incident radiation ($\tilde{\nu}_o$), a Raman band ($\tilde{\nu}'$), and the associated molecular vibrational transition ($\tilde{\nu}_M$) are related such that $\tilde{\nu}' = \tilde{\nu}_o \pm \tilde{\nu}_M$. When $\tilde{\nu}'$ is greater than $\tilde{\nu}_o$, $\tilde{\nu}'$ is an anti-Stokes band; otherwise $\tilde{\nu}'$ is a Stokes band (Tu, 1982; Atkins, 1986). Stokes Raman scattering is generally much more intense than anti-Stokes because the Stokes transitions originate from the well-populated ground state; whereas anti-Stokes scattering originates from vibrational excited states which are poorly populated at room temperature in the absence of electromagnetic stimulation (Long, 1977). Raman scattering occurs due to an oscillating molecular dipole which is induced by the incident light. Raman active vibrational transitions occur when the vibration involves a change in the polarizability tensor $\boldsymbol{\alpha}$ (Long, 1977). The induced dipole moment, $\mathbf{P}$, depends upon the electric field of the incident radiation, $\mathbf{E}$, and $\boldsymbol{\alpha}$ such that $\mathbf{P} = \boldsymbol{\alpha} \cdot \mathbf{E}$ (Long, 1977). If Q_k represents the k^{th} normal coordinate, then the k^{th} normal mode will be Raman active only if

$$\left(\alpha'_{ij}\right)_k = \left(\frac{\partial \alpha_{ij}}{\partial Q_k}\right)_o \neq 0, \qquad (3)$$

for some element α_{ij} of $\boldsymbol{\alpha}$ (Long, 1977). The subscript 'o' denotes evaluation at the equilibrium position, and the term

$(\alpha'_{ij})_k$ represents an element in the derived polarizability tensor for the k^{th} normal coordinate, a_k' (Long, 1977).

Resonance Raman scattering occurs when the incident radiation is coincident with an electronic absorption band of the sample. The resulting enhanced signal is 10^3-10^4 times more intense than normal Raman scattering. An explanation of this phenomena using Kramers-Heisenberg-Dirac dispersion theory has been reviewed by Felton and Nai-Teng Yu (1978).

A highly simplified but very helpful comparison of Raman and resonance Raman phenomena within the framework of classical mechanics (Tu, 1982) is given in Figure 8. In normal Stokes Raman scattering, the inelastic collision between the photon and a sample molecule momentarily results in an unstable union having some 'virtual state' elevated energy level. The photon then separates having $\Delta\nu$ less energy as the molecule enters an excited vibrational condition within the ground electronic state (Tu, 1982). In resonance Raman Stokes scattering, the momentary and unstable union has a much higher energy level, coincident with the energy of an absorbed electron. Through coupling with the electronic transition, the scattering event becomes more probable and there is an increased intensity of scattered light (Tu, 1982). As in the case of normal Stokes Raman scattering, the molecule enters a vibrationally excited ground electronic state as the photon dissociates itself from the molecule. In both Raman events, the light is changed in energy by $\Delta\nu$, corresponding to the vibrational transition of the molecule (Tu, 1982).

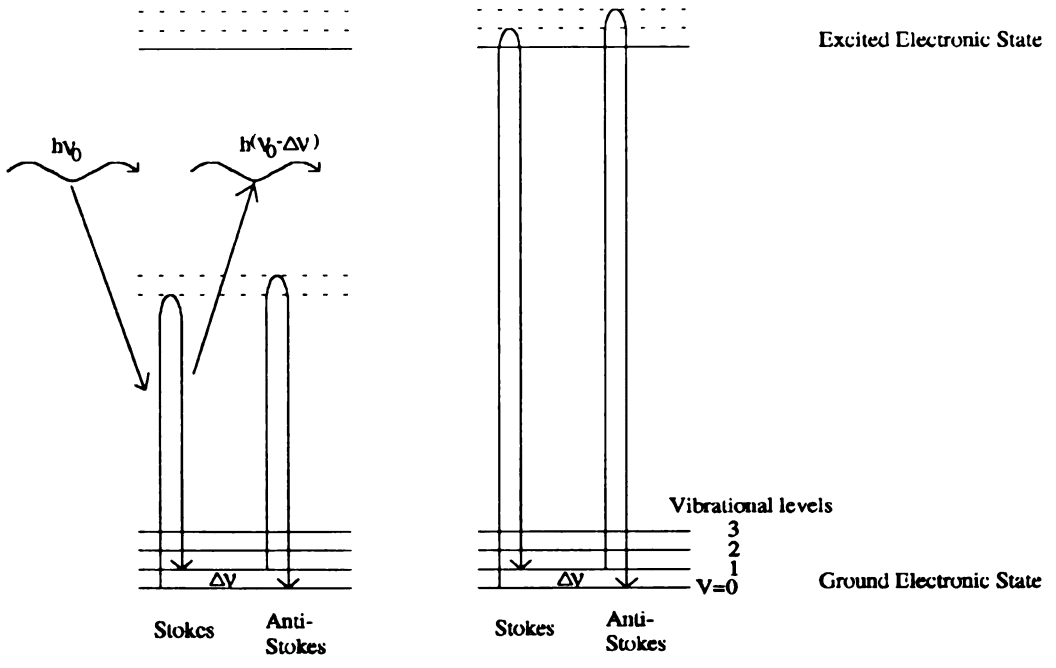

Figure 8. Comparison of (a) Raman and (b) resonance Raman scattering (Tu, 1982).

4.2. ELECTRON MICROSCOPY AND RELATED TECHNIQUES

SEM

The scanning electron microscope (SEM) images primarily the surface features of a sample. The normal imaging process detects secondary electrons which are displaced from outer orbitals of atoms within the sample by the electron beam. Many of these low-energy electrons are reabsorbed by the sample. The electrons reaching the detector are generated from only a shallow depth at the surface; the depth from which the electrons can escape becomes more shallow as the density of the material increases (Flegler, et. al., 1989).

The maximum resolution for a normal SEM is 30 - 60 Å under the best circumstances (Flegler, et. al., 1989). If the sample is not sufficiently conducting, charging effects can distort and blur the

image. To increase conductivity, the samples are often coated with a thin layer of gold (Flegler, et. al., 1989). Under the electron beam, especially at higher operating voltages, considerable sample deterioration may take place. Samples must be carefully dried of any volatile components prior to SEM examination or they will experience rapid and often destructive drying under the electron beam. To avoid this problem, uncoated, wet samples can be examined using special cryo attachments (Flegler, et. al., 1989).

TEM

In contrast with the SEM, the transmission electron microscope (TEM) produces an image from the entire depth of a very thin, very small sample. Internal structure and surface features both contribute to the image generated by the transmitted electrons. Sample thickness can strongly affect the image since the effects of internal features throughout the entire thickness of the sample become superimposed (Flegler, et. al., 1989).

A good TEM can achieve a maximum resolution of about 2 Å under the proper conditions (Flegler, et. al., 1989). However, for some less robust materials, sample damage can be a problem when working at high voltages. Sample thickness can range from 400 - 1500 Å. The thinner samples are required for denser materials (Flegler, et. al., 1989).

Sample preparation is usually considered the most difficult aspect of acquiring TEM data. Thick samples must first be microtomed or thinned by some process such as ion milling, and these processes can leave undesirable artifacts (Flegler, et. al., 1989).

STM

The scanning tunneling microscope (STM) allows atomic-scale surface imaging of conductive samples. The technique involves applying a small bias voltage between the sample and an atomically sharp probe positioned ~8–10 Å above the surface (Hammers, 1991). The resulting tunneling current is ~1 vA, a sensitive function of the separation gap between sample and probe (Hammers, 1991). By controlling the probe height to provide a constant tunneling current, the surface can be scanned and the relative probe height can be recorded as a function of x and y coordinates. The technique is especially useful for studying metals and semi-conductors (Hammers, 1991). When attempting to resolve the atomic-scale structure, avoiding oxide layers and adsorbed contaminating species is essential. However, the technique can also be used to image slightly larger features, in which case oxide layers do not pose a significant problem. For sufficiently large features, the surface of non-conducting samples can be coated with a thin layer of conducting material, such as gold (Hammers, 1991). Using a low energy technique such as low-pressure thermal evaporation, many surfaces can be coated without significant damage. However, a monolayer of gold can be applied only to surfaces which can be 'wet' by the gold. Other surfaces require that the grains of gold build up until they interconnect to from a continuous conducting surface resulting in gold layers which are 70 Å thick, or more (Hwang, 1991).

AFM

The atomic force microscope (AFM) represents a modification of the STM which avoids the use of a tunneling current. Consequently, this

instrument can be used to image non-conductors as easily as conductors (Pool, 1990). The probe is lowered to "touch" the sample which is scanned while controlling the probe height to maintain a constant force between the probe and sample. Actually, the instrument is sensitive enough so that the electron density from the probe interacts with the electron density of the sample, without much interpenetration. For hard samples, the microscope has a resolution of 1-2 Å (Pool, 1990). However, for softer materials such as proteins, resolution is limited to ~ 50 Å, and for very soft materials such as blood cells, the limiting resolution is ~ 100-200 Å . Improved imaging of softer materials may be achieved by examining very low-temperature samples (Pool, 1990).

4.3. FILM THICKNESS DETERMINATION

Film thickness can be measured mechanically by dragging a sensitive stylus across a small ledge formed by scratching a section of the film off the substrate. This situation is shown in Figure 9. One instrument capable of such measurements is the DEKTAK IIA, manufactured by Sloan, Inc. According to the manufacturer, the instrument can scan samples up to 20 mm thick, measuring film thicknesses between 200 - 655,000 Å with a maximum vertical resolution of 5 Å.

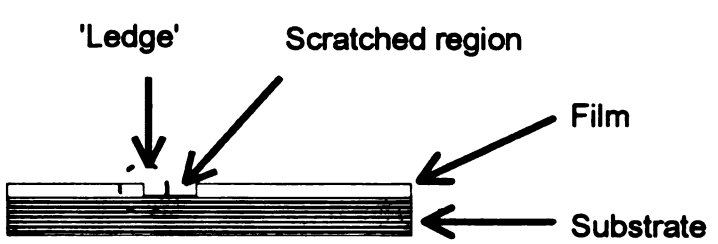

Figure 9. Scratched film for film thickness measurement.

The DEKTAK IIA was equipped with the standard 12.5 μm radius stylus, and the instrument was accompanied by a standard reference provided by the manufacturer for calibration. The depth of the step etched in the silicon reference was 933 Å ± 5%.

CHAPTER 5.

EXPERIMENTAL EQUIPMENT, MATERIALS, AND METHODS

The equipment, materials, and methods used for inert atmosphere work, spin-casting films, preparation of solutions, porphyrin reduction, diffusion experiments, and chemical and structural analysis will be briefly described in this chapter.

5.1. EQUIPMENT FOR INERT ATMOSPHERE EXPERIMENTS

SAMPLE CELLS

Iron porphyrins must be isolated from oxygen before they can be effectively reduced to the Fe(II) state, and a variety of sample cells were used to effectively protect the various types of samples from the atmosphere. The most basic of these cells was a cuvette with a 14/30 ground quartz joint which could be sealed with a rubber septum or fit with a ground glass stopper. This cell, shown holding a slide in Figure 10 (left), was used to examine both films and solutions. When sealed with a septum, the cell was slowly contaminated by diffusing oxygen making it unsuitable for air-sensitive applications of very long duration. When greater protection from oxygen was required, a cuvette connected to two high vacuum valves, also shown in Figure 10 (right), was used for solutions. Another apparatus with high vacuum valves was used for films (not shown) which was similar to that used for liquids except that the cuvette was attached with a 14/30 ground glass joint.

The round bottom flask allowed liquids to be deoxygenated with the freeze-pump technique and then transferred to the cuvette.

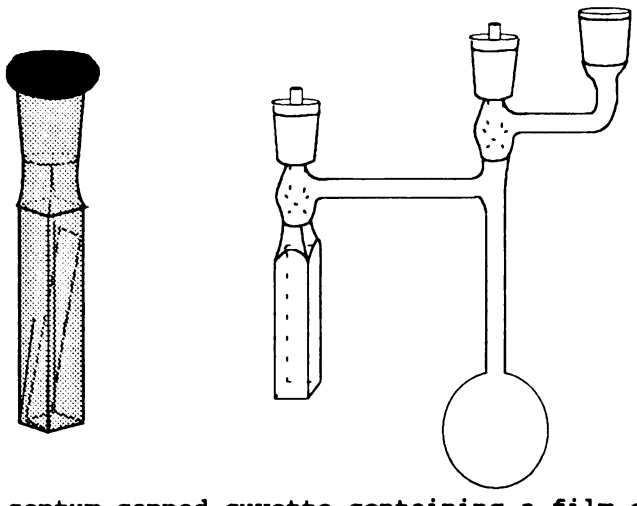

Figure 10. A septum capped cuvette containing a film-coated slide (left), and a cuvette with two high vacuum valves and an attached flask (right).

VACUUM LINE

When working with air-sensitive compounds it is often helpful to use combined vacuum and inert gas manifolds (Shlenk lines) to efficiently purge the sample of oxygen and provide an inert gas atmosphere. The apparatus used for this work is shown in Figure 11. The vacuum was provided by a Cenco Hyvac 4 pump driven at 1725 rpm by a 1/3 HP motor. The vacuum pump was connected to a vapor trap which was submerged in a dewer of liquid nitrogen whenever the pump was operating. The argon was run through a drying column before entering the manifold.

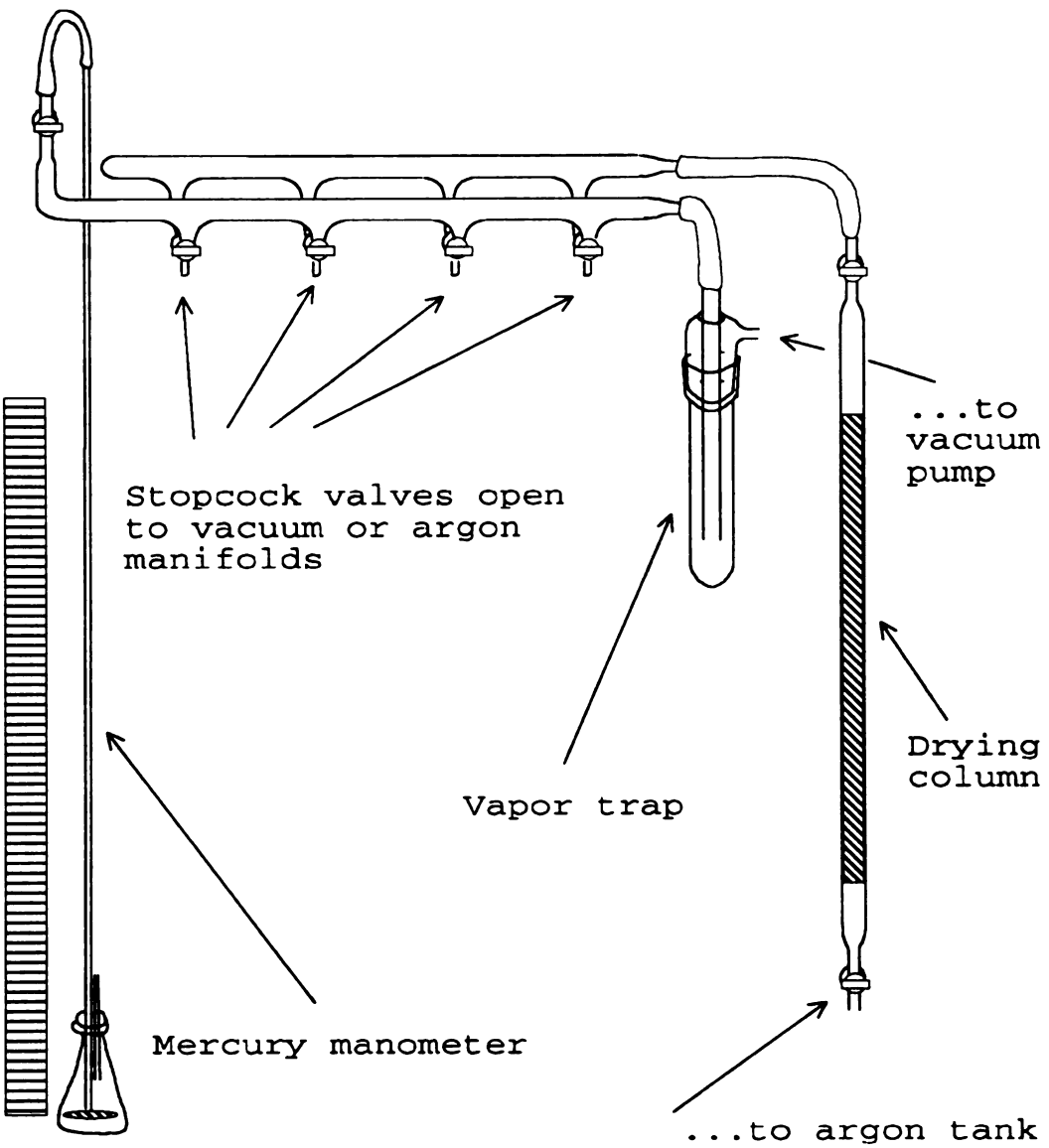

Figure 11. Vacuum line and argon manifolds.

5.2. SPECTROSCOPY EQUIPMENT

The UV-vis experiments were carried out primarily on a Perkin-Elmer Lambda 3A Spectrophotometer with a R 100A Recorder. Experiments were also conducted on a Perkin-Elmer Lambda Array 3840 Spectrophotometer driven by a 7300 Professional Computer.

Infrared spectra were collected on a Perkin-Elmer 1750 Fourier Transform Spectrometer, accompanied by a 7700 Professional Computer and a Model PP-1 Plotter Printer. This FTIR spectrometer was also equipped with a Spectrotech ATR and Perkin-Elmer Cylindrical Internal Reflection (Circle® cell) accessories. The ATR accessory was used with a germanium, 45° entry-angle ATR crystal, and the Circle® cell was equipped with a cylindrical, zinc selenide crystal.

The Raman spectra were collected with a SPEX 1877 spectrometer, fitted with 600, 1200, 1800, or 2400 gr/mm gratings in the spectrographic stage and 1200 or 1800 gr/mm gratings in the filter stage. All Raman results reported in this work were acquired with the "macro" illumination stage, although the instrument was also equipped with a Zeiss-Microscope, micro-Raman accessory. The detector was an EG&G 1460 optical multichannel analyzer (OMA) with a 1024 channel array.

Three different lasers were used as light sources in Raman experiments. The 514.5 nm line was generally supplied by the Spectra Physics 164-5 argon ion laser. Other lines were generated by either the Innova 200 argon or the Innova 90 krypton ion lasers manufactured by Coherent. The lasing lines for both Coherent lasers are shown in Table 6.

Table 6. Lasing lines for Coherent argon and krypton ion lasers.

Argon Laser Lines (nm)	Krypton Laser Line (nm)
Single line visible:	Single line visible:
528.7	647.1
514.5	646.4
488.0	568.2
457.9	530.9
Single line UV:	520.8
363.8	482.5
357.7	476.2
351.1	468.0
335.9	415.4
334.5	413.1
333.6	406.7

A standard cuvette holder and 90° scattering was used for all liquid samples, and a grazing angle arrangement was used when taking Raman spectra of the films. The films were attached to rotatable turret, and the rotation was set to maximize the Raman signal. When examining the reduced porphyrin-doped films, glass and Tygon rubber spacers were used to hold the films securely within 2 mm from the wall of the cuvette, and the cuvette was held horizontally along the rotatable turret as shown in Figure 12.

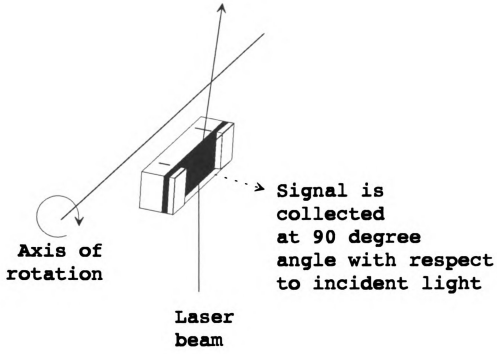

Figure 12. Orientation of film in cuvette during Raman experiment.

5.3. ELECTRON AND ATOMIC FORCE MICROSCOPES

The scanning electron micrographs were taken on a JEOL JSM-35CF at 15 kV. The samples were mounted in resin without a gold coating.

The transmission electron micrographs were acquired on a JEOL JEM-100CX II electron microscope capable of 120 volts of accelerating voltage. The coating solution was applied to copper grids which were then placed in a stream of rapidly moving air to remove most of the material -- leaving only a thin film covering a few grid openings.

The atomic force microscope was the NanoScope III manufactured by Digital Instruments. The D head was used to scan the surface of the film in air. The cantilevers were made of silicon nitride with force constants of 0.12 and 0.58 N/m.

5.4. CHEMICALS

Carboxylic acids were purchased from Aldrich Chemical Co. and used without further purification, as was the *titanium isopropoxide*. The *porphyrins*, shown in Figures 13 and 14, were previously synthesized and purified in the laboratory of Dr. Chris Chang (Chang and Ebina, 1981; Sotiriou and Chang, 1988; DiNello and Chang, 1978). The argon was 99.99% pure from AGA Gas, Inc., and the CO was Ultra High Purity (99.99% pure) from Matheson Gas Products. The glass substrates were made from standard, pre-cleaned microscope slides (VWR Scientific Inc.). The glass cleaning solution was Micro (International Products Corporation). All water was de-ionized, with a resistance of 18 Mohm.

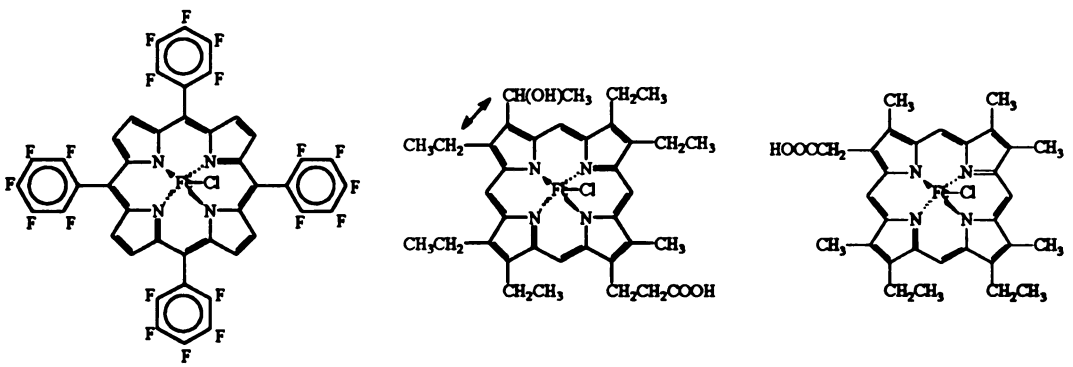

Figure 13. Structures for three porphyrins (P1, P2, and P3) which have been incorporated into the titanium metalorganic films. (a) P1 is 5,10,15,20-tetrakis(pentafluorophenyl)porphyrin Fe(III) chloride. (b) P2 has both a hydroxyl and a carboxyl group. The structure shown is one of two structural isomers present in a 1:1 ratio of P2; the other isomer is formed by exchanging the two groups indicated by the arrow. (c) P3 has a single carboxyl group.

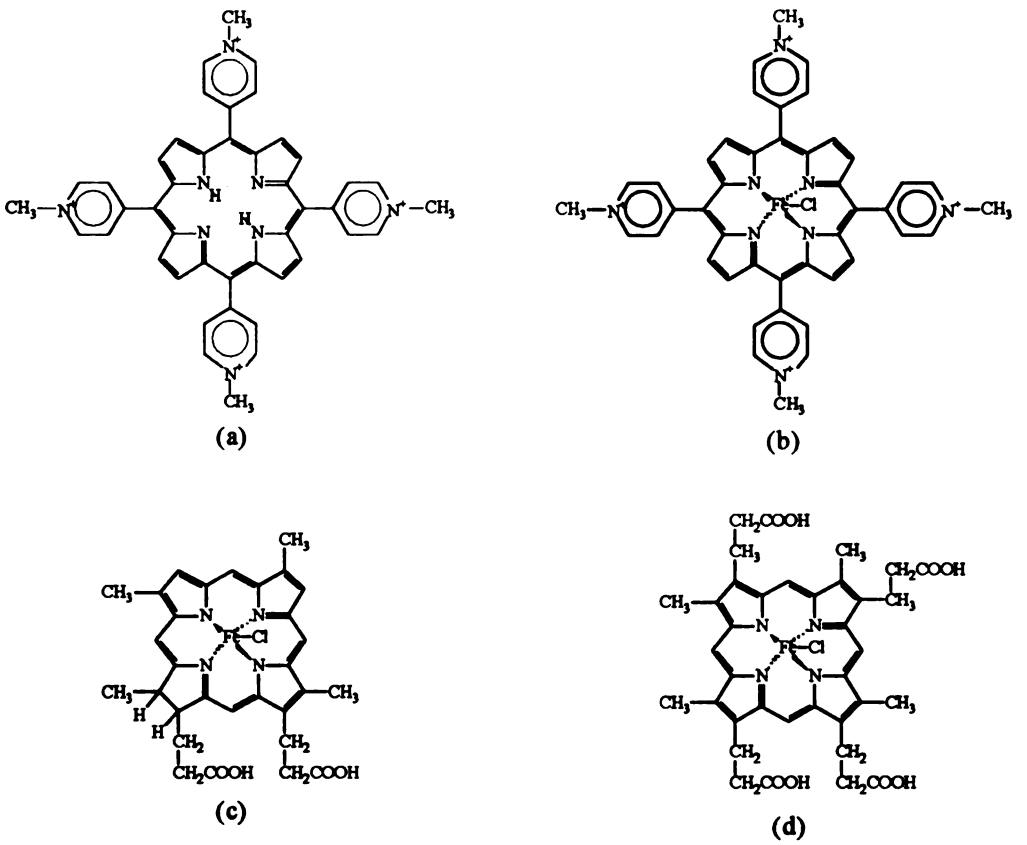

Figure 14. Additional porphyrins which have been used in studying porphyrin-film compatibility. (a) Water soluble 5,10,15,20-Tetrakis(1-methyl-4-pyridyl)-21H,23H-porphine, tetra-p-tosylate salt, P4; (b) 5,10,15,20-Tetrakis(1-methyl-4-pyridyl)-21H,23H-porphine Fe(III) chloride salt, P5; (c) a dicarboxylic acid chlorin, P6; and (d) a tetracarboxylic acid porphyrin.

5.5. SPIN-CASTING FILMS

The glass substrates were standard microscope slides which were cut into strips to easily fit a 10 mm pathlength cuvette. Before coating the slides, the glass was cleaned for 30 minutes in a sonic bath while submerged in Micro cleaning solution, rinsed in distilled water, and air dried. The coating solution containing the porphyrin, aged from 2-4 days, was then applied to the surface of the substrate, and spun-dry at approximately 1,100 rpm. The newly cast films were then dried with a heat gun for 2 minutes to drive off the majority of the residual solvent and then aged for at least three days.

5.6. PREPARATION OF SOLUTIONS

STOCK CO SOLUTIONS

Two saturated aqueous solutions were prepared at atmospheric temperature and pressure -- one with argon, the other with carbon monoxide. The apparatus for deoxygenating and saturating the water with gas consisted of a stoppered Erlenmeyer flask fitted with a thermometer, a gas dispersion tube, and gas inlet and outlet tubes. The bottom of the flask was modified by the addition of a short tube covered with a septum to allow samples to be withdrawn by syringe. The gas outlet tube was connected to a bubbler to prevent the back-diffusion of oxygen into the solution. This apparatus is shown in Figure 15.

Initially, both gas-saturation devices were connected in series and flushed with argon for 24 hours to thoroughly deoxygenate the water. The gas inlet of one unit was then transferred to a tank of high purity carbon monoxide while the other unit remained on argon. Gas was allowed

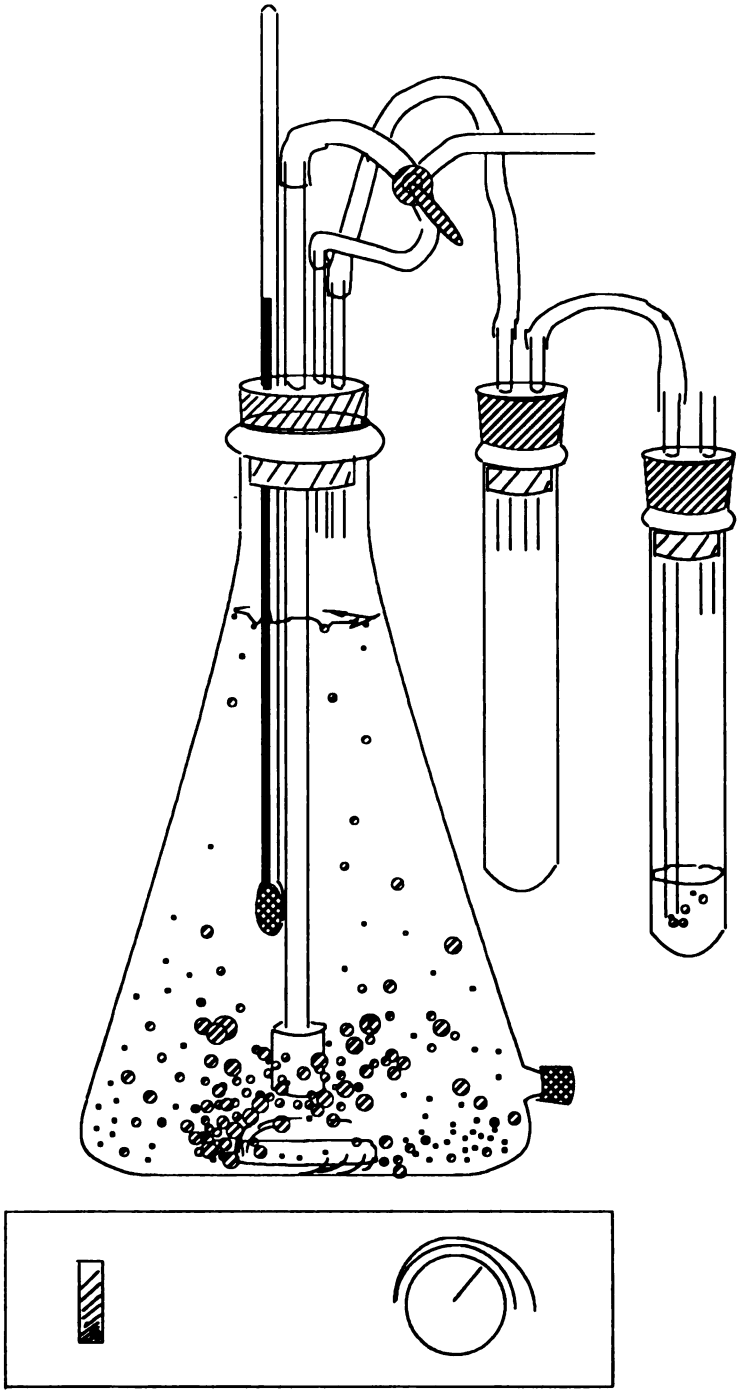

Figure 15. Apparatus for deoxygenation and gas saturation.

to bubble through the gas dispersion tubes until one hour before withdrawing a sample, at which time the gas flow was redirected to bypass the dispersion tube, circulating directly through the head-space above the liquid in the flask. Magnetic stir bars were used to mix the solution during both phases of this saturation process.

The solubility of CO in water as a function of total pressure and temperature has been thoroughly investigated and high precession Henry coefficients have been calculated between 5 and 50 °C at the saturation pressure of the solvent (Rettich et. al., 1982). The Poynting correction, P, can be used to adjust the Henry coefficient, H, for pressures significantly above the solvent saturation pressure, P_s. Although Henry coefficients are defined at infinite dilution, they are thought to remain highly accurate for partial pressures up to one atmosphere for CO, and they can be useful for moderately higher pressures (up to ~10 atm). The calculated coefficients were fit to two smoothing functions which allowed for the calculation of $H(T,P_{s,H_2O})$ for any temperature between 5 and 50 °C, where T is temperature and P_{s,H_2O} represents the saturation pressure of water. The mole fraction of CO in solution is then given by:

$$x_{CO} = \frac{f_{CO}}{H_{CO,H_2O}} = \frac{\phi_{CO} y_{CO} P}{H_{CO,H_2O}} \cong \frac{P_{CO}}{H_{CO,H_2O}}, \tag{4}$$

$$H_{CO,H_2O}(T,P) = H_{CO,H_2O}\left(T,P_{S,H_2O}\right)\cdot P, \tag{5}$$

$$P = e^{\int_{P_{S,H_2O}}^{P}\left[V_{CO}^{\infty L}(T,P)/RT\right]dP} \cong e^{V_{CO}^{\infty L}\left(P-P_{S,H_2O}\right)/RT}. \tag{6}$$

The symbol H_{CO,H_2O} represents the Henry coefficient for an infinitely dilute solution of CO in water; f_{CO} is the fugacity of CO in the vapor phase; $V_{CO}^{\infty L}$ is the partial molar volume of CO in the liquid phase at infinite dilution; and R is the ideal gas constant (Rettich et. al., 1982).

DILUTED CO SOLUTIONS

The CO solutions were mixed directly within a disposable syringe, shown in Figure 16. A small stir bar was placed within a 20 ml syringe and the argon solution was drawn into the syringe followed by the expulsion of all air bubbles. The solution was ejected and the syringe was refilled with fresh argon saturated water, and then the ejection and refilling was repeated. The syringe needle was quickly replaced by a small septum which is then momentarily pierced by a small needle through which any trapped air and contaminated water can be immediately expelled. After withdrawing the needle from the septum, the filled syringe was weighed to determine the mass of the water. (The empty syringe, stir bar, and septum must have been previously weighed.) A known volume of saturated CO solution was then injected into the syringe through the septum and the solution was mixed with the magnetic stir bar until needed.

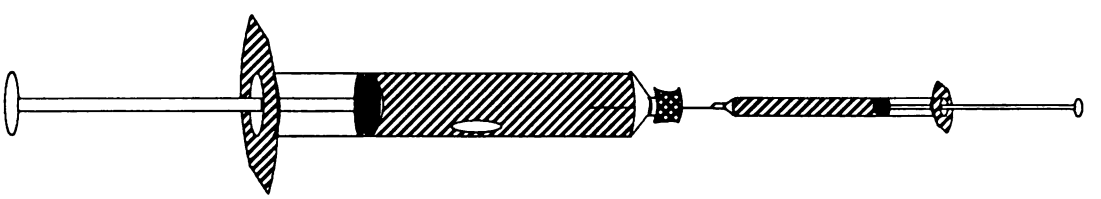

Figure 16. Disposable syringe mixing cell used for the preparation of dilute solutions for air-sensitive experiments.

5.7. REDUCTION OF PORPHYRIN

REDUCTION IN SOLUTION

To reduce a porphyrin in solution, the oxygen was first removed by bubbling argon through the liquid or by repeatedly freezing the liquid, pumping it down, and thawing the liquid. The reducing agent was added to the solution or it was photoreduced. To photoreduce the porphyrin, a trace amount of acetophenone or benzophenone and some isopropanol was added to the solution, which was then irradiated with UV light until no further change occurred in the absorption spectrum, as described by Ward and Chang (1982). To effectively reduce the solution with sodium dithionite, the solution must solvate the reducing agent. When the porphyrin solution could solvate a sufficient amount of water, a hydrazine hydrate solution was often used to carry out the reduction.

REDUCTION WITHIN THE FILM

The film was placed in a cuvette of deionized water and capped with a septum, as shown in Figure 10. Argon was then bubbled through the water for thirty minutes prior to the reduction of the porphyrin by one of three methods: hydrazine, sodium dithionite, and photoreduction.

When using hydrazine to reduce the iron porphyrin, 0.1 ml of aqueous hydrazine hydrate was injected into the cuvette, and the solution was allowed to sit for a half-hour. The liquid is drained under argon atmosphere through a needle attached to a short tube with its end submerged in water to prevent the back diffusion of oxygen.

Sodium dithionite was less convenient to use since it was a powdered solid rather than a liquid. However, the reduction could be accomplished by adding an excess of the compound to the deoxygenated solution within the cuvette, and then recapping the cuvette to resume the deoxygenation. Just as with hydrazine, the solution should be drained from the cuvette under argon after contacting the film for approximately 30 minutes .

Photoreduction was perhaps the cleanest of the reduction techniques. The acetophenone was either directly incorporated into the film or added to the solution along with the isopropanol. Argon was bubbled through the solution for 20 minutes. The film was exposed to short wave UV radiation for several minutes and its absorption spectrum was taken to monitor the completion of the reduction. Argon purging (for at least five minutes) and the radiation exposure were repeated until no further changes in the absorption bands were apparent. The liquid could then be drained under argon as described with the other reduction methods.

5.8. EXPOSING FILM TO CO SOLUTION

The syringe containing the CO solution was fitted with a needle and ~1 ml of solution was ejected to purge the syringe of any oxygen contamination which may have occurred during removal of the septum and installation of the needle. The remaining CO solution was then injected into the cuvette through the septum. The argon gas and the excess CO solution were allowed to leave the cuvette through the same needle and bubbler used when flushing the cell with argon. When the needles were

withdrawn, the cell was entirely filled with the CO solution and no bubbles were apparent.

CHAPTER 6.

CHEMICAL CHARACTERIZATION STUDIES

6.1. ACHIEVING PORPHYRIN-FILM COMPATIBILITY

It is difficult to introduce a sufficient quantity of Fe(III) porphyrin into the coating solution without disrupting the optical clarity or integrity of the film or the chemical reactivity of the porphyrin. For a given coating solution and application, the functional groups substituted on the porphyrin ring must be carefully selected since they effect both the solubility of the porphyrin in the solution and the sensitivity of the absorption bands to porphyrin-solute interaction. The earliest metalorganic coating formulations we used (Gagliardi and Berglund, 1989) were aqueous solutions. The water soluble freebase porphyrin, P4, shown in Figure 14(a), was highly compatible with these mixtures. When P4 was metalated with copper, it was still highly compatible with the solutions, and the resonance Raman spectra of the porphyrin, shown in Figure 17, indicated that the film had not comprised the integrity of the porphyrin. When P4 was metalated with Fe(III), shown as P5 in Figure 14(b), the porphyrin was still compatible with the films, although the compatibility was much less than for the copper complex. In general, the ferriheme is much less soluble in the coating solution than the corresponding freebase porphyrin or copper complex.

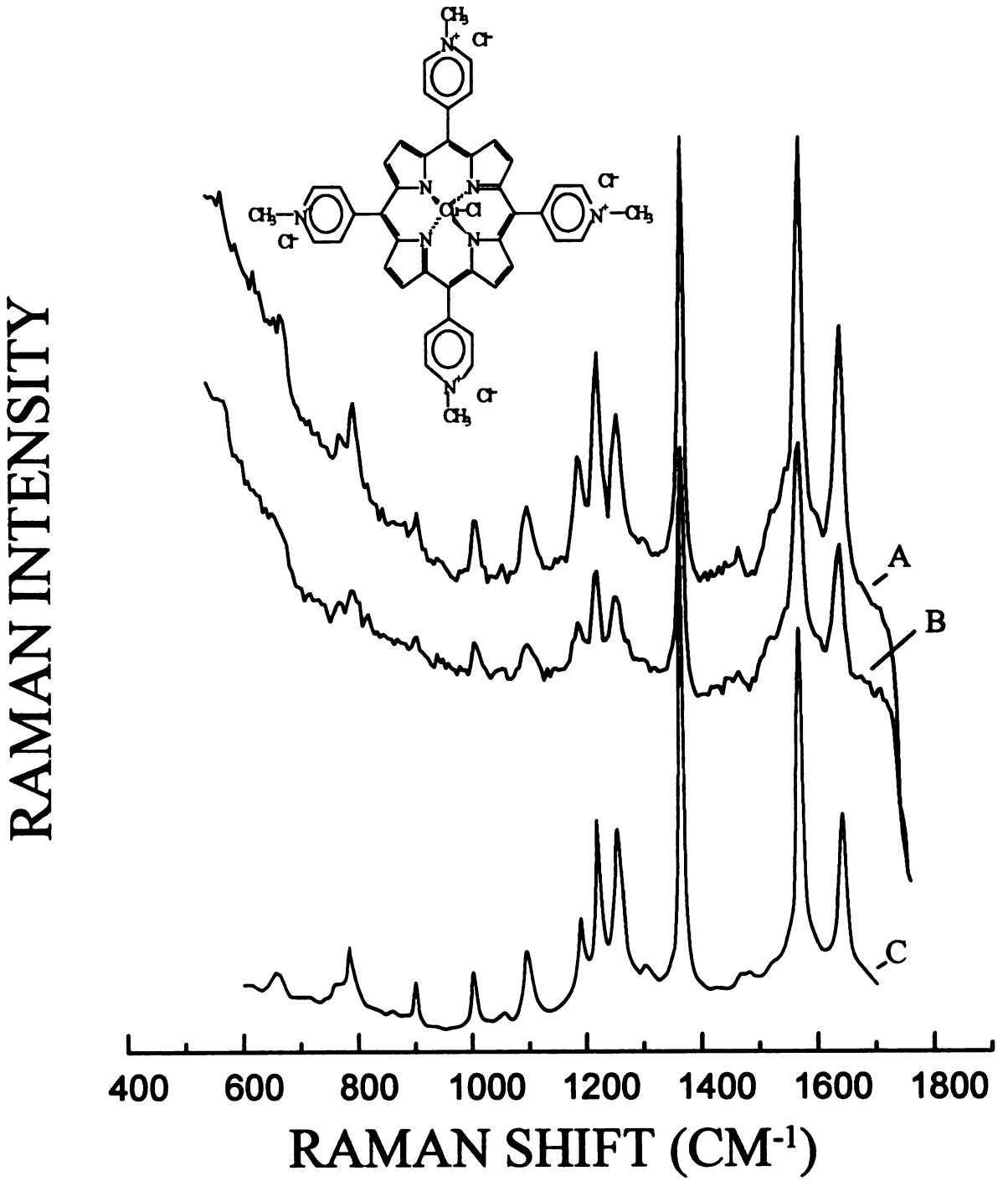

Figure 17. Resonance Raman spectra of copper metalated P4, acquired with an λ_{ex} of 413.1 nm, in: (A) Hf-based water soluble film, (B) Ti-based water soluble film, and (C) aqueous solution.

As improvements in the film solutions led to drastically different formulations containing much less water (Gagliardi, et. al., 1990), the amount of P5 which could be incorporated into the film became inadequate, and new porphyrins were needed. In the new preferred coating solution, without the use of ethanol as a dispersing agent, the three components of the coating mixture are valeric acid, titanium isopropoxide, and water -- valeric acid being most abundant and acting as both reactant and solvent. When ethanol is used as a dispersing agent, it is the most abundant solvent present, with a (solvent:alkoxide) volumetric ratio of 8:1. Porphyrins which were soluble in valeric acid and ethanol could be incorporated into the films. Subsequently, it was found that carboxyl, hydroxyl, and fluorinated phenyl substituents can be used to enhance the incorporation of the porphyrin within the film solution. The three porphyrins (P1, P2, and P3), shown in Figure 13, have been introduced into the titanium alkoxide valerate solutions at sufficiently high concentrations, reduced *in-situ*, and used to provide adequate sensitivity to CO.

6.2. RAMAN CHARACTERIZATION OF PORPHYRIN-FILM INTERACTIONS

Given that porphyrins having hydroxyl, carboxyl, or fluorinated phenyl groups possess superior compatibility with the film solution, determining the nature and extent of the film-porphyrin interaction is still of importance. It is fairly certain that porphyrins having one or more hydroxyl or carboxyl groups chemically react with the coating solutions. This reactivity is supported by the literature, and porphyrins and other guest molecules having multiple hydroxyl or carboxyl groups have been

observed to cause gelation in mixtures which otherwise have never been observed to gel. The extent and nature of reactivity for the fluorinated phenyl groups on P1 is somewhat less certain. The resonance Raman (RR) spectra of the reduced porphyrin in the film and in ethanol solution, shown in Figure 18 (b, c), are similar but not identical. The RR spectra of tetraphenyl porphyrins are known to show bands associated with the phenyl rings, and this has been attributed to significant conjugation with the porphyrin π-system (Spiro, 1983). The band at 727.1 cm^{-1} is within the expected frequency range for aromatic rings (Colthrop, et. al., 1990) and its disappearance when the porphyrin is in the film probably indicates that phenyl groups are reacting in some way with the film material -- perhaps by the displacement of one or more fluorines on the phenyl ring.

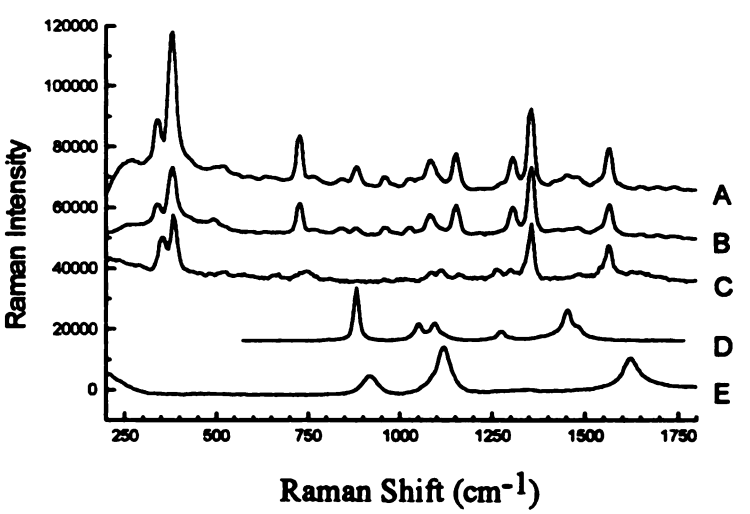

Figure 18. Raman spectra of P1. (A) P1-Fe(III) in EtOH, (B) P1-Fe(II) in EtOH with hydrazine, (C) P1-Fe(II) in film in aqueous hydrazine solution, (D) EtOH, (E) hydrazine.

The reactivity between the porphyrin and the film was clearly a welcome benefit, so long as the porphyrin's ability to react with the

solute of interest was not impaired. If the porphyrins were merely entrapped within the film, they would be likely to leach out (to some degree) if the films were soaked in a solvent such as ethanol. The bound rather than entrapped porphyrin would result in a more solvent resistant coating.

6.3. RAMAN CHARACTERIZATION OF COATING SOLUTION

Titanium isopropoxide reacts exothermically with carboxylic acids. Spectroscopically, the reaction appears to be very similar for carboxylic acids ranging in length from three to eight carbons. The spectra for these alkoxide-carboxylic acid mixtures are shown in Figure 19.

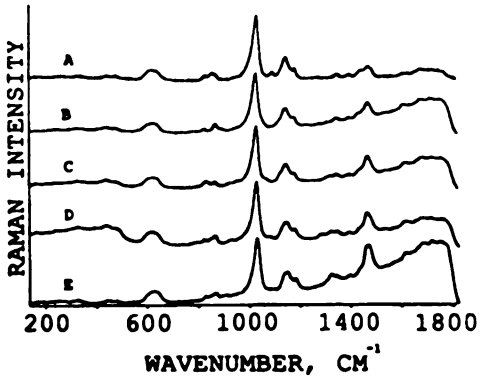

Figure 19. Raman spectra of titanium alkoxide-carboxylic acid mixtures with an acid-to-alkoxide molar ratio of 10. Acids used: (a) propionic, (b) butyric, (c) valeric, (d) hexanoic, and (e) octanoic.

Although the spectral features of these mixtures are quite similar, the quality of the films varies greatly as a function of acid chain length. The data shown in Table 7 clearly indicates that valeric and

Table 7. Composition of coating solutions and description of resulting films[a].

Acid	R_a[b]	R_w[c]	Film Description
Propionic	2.5	0.0	extensive cracking, flaking
Propionic	10.0	0.0	extensive cracking, flaking
Butyric	2.5	0.0	extensive cracking, flaking
Butyric	10.0	0.0	moderate cracking, flaking on edges
Valeric	2.5	0.0	extensive cracking, flaking
Valeric	10.0	0.0	moderate cracking, flaking on edges
Hexanoic	2.5	0.0	extensive cracking, flaking
Hexanoic	10.0	0.0	slight cracking, slight shrinkage at edges, soft
Octanoic	2.5	0.0	slight cracking, moderate shrinkage at edges, soft
Octanoic	10.0	0.0	never hardens, evaporates over time
Propionic	2.5	1.4	extensive cracking, flaking
Propionic	10.0	1.4	moderate cracking, slight flaking on edges
Butyric	2.5	1.4	extensive cracking, flaking
Butyric	10.0	1.4	no cracking, good uniformity and adhesion
Valeric	2.5	1.4	extensive cracking
Valeric	10.0	1.4	no cracking, very good uniformity and adhesion
Hexanoic	2.5	1.4	no cracking, extensive shrinkage at edges, soft
Hexanoic	10.0	1.4	never hardens, evaporates over time
Octanoic	2.5	1.4	slight cracking, moderate shrinkage at edges, soft
Octanoic	10.0	1.4	never hardens, evaporates over time

[a]The described characteristics appear much more quickly for the solutions without water. [b]Ra is the molar ratio of carboxylic acid to alkoxide. [c]Rw is the molar ratio of water to alkoxide.

butyric acids produce the best films, with valeric acid performing slightly better than butyric. Subtle differences in chemistry can undoubtedly have drastic effects on the end performance of the film materials. The superiority of valeric and butyric acids may result from their effect on the extent of polymerization and on the suitability of their size within the polymer network. These coatings are molecular composites in the sense that a brittle inorganic network is being reinforced with flexible alkyl chains on a molecular level, and the relative amount of organic material and the length of the alkyl chain should have a profound influence on the strength and hardness of the material. It is quite likely that the organic molecules are acting like fiber reinforcements in conventional composites. This view is supported by evidence that although low acid-to-alkoxide molar ratios produce poor films with valeric acid, the same molar ratio can produce excellent films if some of the valeric acid is replaced by lauric acid. If only lauric acid is used the resulting films are soft and waxy.

The vibrational band assignments for TiPT have been discussed in several previous papers (Berglund, et. al, 1986; Zeitler and Brown, 1957; Bradley and Mehrotra, 1978). However, due to coupling between C-O and C-C vibrational modes, the band assignments have been difficult to make (Bradley and Mehrotra, 1978). The strongest TiPT peaks occur at 1026 cm^{-1} and 1182 cm^{-1}. The peak at 1026 cm^{-1} has been associated with the (C-O)Ti stretching vibration (Berglund, et. al, 1986). The infrared assignment for this stretch was given as 1005 cm^{-1} (Bradley and Mehrotra, 1978). The band at 1182 cm^{-1} has been taken as predominantly a skeletal stretch similar to the IR peak reported at 1170 cm^{-1} (Zeitler and Brown, 1957). It is likely that both the 1026 cm^{-1} and 1182 cm^{-1}

bands represent coupled vibrational modes; therefore, they should not be expected to agree exactly with literature values for the pure vibrational modes. Discrepancies between the IR and Raman peaks can also be expected due to the different selection rules. The peaks of intermediate intensity at 565 cm^{-1} and 612 cm^{-1} may be taken as the symmetric and antisymmetric stretch of Ti-O, respectively (Berglund, et. al, 1986; Bradley and Mehrotra, 1978). The weak peaks at 1129 cm^{-1} and 852 cm^{-1} agree closely with the reported IR values of 1131 cm^{-1} and 851 cm^{-1} for a coupled C-O stretch and skeletal vibration, and a pure skeletal stretch, respectively. The band at 1182 cm^{-1} diminishes with increasing amounts of acid, and the isopropanol peak at 819 cm^{-1} begins to appear as the iPr-O- groups on the titanium are displaced by carboxylate ligands. The symmetric Ti-O stretch at 565 cm^{-1} also decreases, leaving the other Ti-O stretch at 612 cm^{-1} undiminished.

The relative peak intensities of the 565 cm^{-1} and 612 cm^{-1} vibrations appear to change more with the addition of lauric acid than with shorter chain-length acids. This could also partly account for the stabilizing effect of adding small amounts of lauric acid to the other coating mixtures. The spectra showing increasing amounts of lauric acid appear in Figure 20.

When water is added to the carboxylic acid-titanium isopropoxide mixture, the first Raman observable manifestation of hydrolysis is the disappearance of the Ti(O-R) band at 1023 cm^{-1}. This structural transformation occurs on a very short time scale. Various stages of this reaction, as shown in Figure 21 for the case of the titanium alkoxide valerate solution, can be resolved with the aid of a rapid mixing cell (Payne, 1986) and a variable speed syringe pump; the faster the reactants are pumped through the cell, the shorter the time between

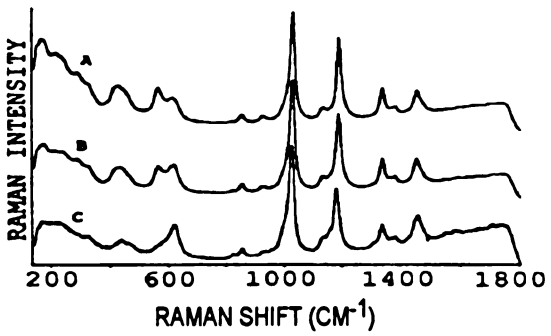

Figure 20. Raman spectra showing the effects of increasing amounts of lauric acid on titanium isopropoxide (TiPT). (A) Pure TiPT, (B) TiPT + lauric acid, R_a=0.12, (C) TiPT + lauric acid, R_a= 0.62. (R_a = the acid-to-alkoxide molar ratio).

mixing and observation. From these experiments, it is estimated that this reaction takes place within 0.4 seconds of mixing. It is also interesting to note that simultaneous transformations occur in the lower frequency region between 150 and 750 cm^{-1} where the broadening of the band near 600 cm^{-1} and the formation of a band near 385 cm^{-1} can be observed.

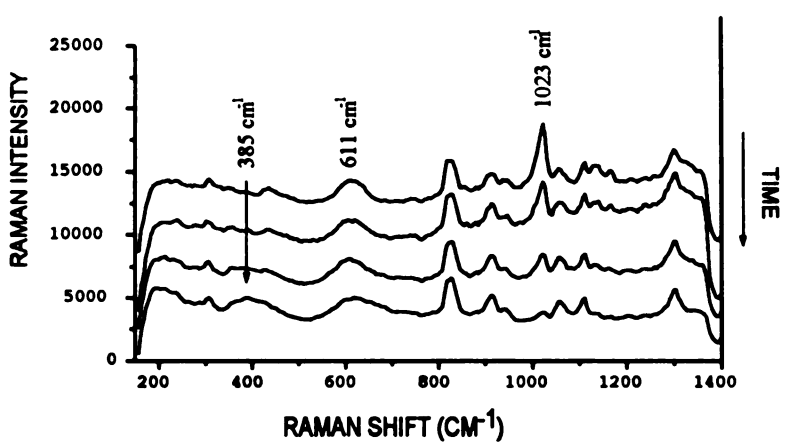

Figure 21. Changes in the Raman spectra during the initial stage of hydrolysis resolved by varying the flow rate in a quartz rapid mixing cell. The top spectrum shows the titanium isopropoxide valerate solution before any appreciable hydrolysis has occurred, and the spectra below show an increasing degree of hydrolysis. The stage of hydrolysis shown in the bottom spectrum is reached within 0.4 seconds after complete mixing.

6.4. STABILITY STUDIES OF COATING SOLUTION

Depending on the relative concentrations of reactants, chemical changes can continue to occur in the coating solutions for more than 130 hours or the solutions may stabilize in less than eight hours. The systems studied showed no tendency toward gelation, and the stabilized solutions provided no evidence of detectable colloidal particles. It is no surprise that the initial effect of hydrolysis is the removal of an isopropoxy group, and from the literature, one might also expect that the slower observable transformations would be due to condensation reactions. The modification of titanium alkoxides by acetic acid aids in 'decoupling' the hydrolysis and condensation reactions (Sanchez and Livage, 1990), and it has been noted that sol-gel product characteristics depend upon the relative rates of hydrolysis and condensation, where fast hydrolysis followed by slow condensation produces a polymeric sol (Livage, et. al., 1988). The systems studied here are certainly polymeric in nature, if not merely a solution of oligomers. However, the slow condensation reactions are not necessarily the only slow reactions taking place. Figure 22 shows Raman spectra for aged titanium isopropoxide valerate solutions with various amounts of added water. While the Raman bands above 800 cm^{-1} show no transformation, the growth and reduction of bands at 397 cm^{-1} and 663 cm^{-1} show the creation and consumption of a reaction intermediate. The growth of the bands can be seen for R_w=1.0, where R_w is the water to alkoxide molar ratio. For larger amounts of water (R_w: 1.5 - 3.0), the concentration of the intermediate is already decreasing at the time of the first observation. Thus, the rate of the depletion of the

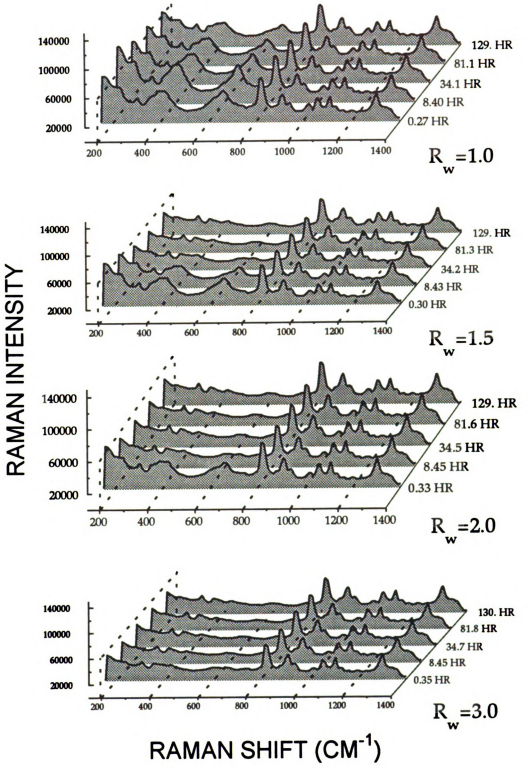

Figure 22. Raman spectra of aged titanium isopropoxide valerate solutions with alkoxide to water ratios (R_w) of 1.0, 1.5, 2.0, and 3.0. Sample age ranged from 0.27 to 130 hr.

intermediate increases with increasing water concentration, suggesting that the intermediate is being hydrolyzed.

A comparison of various carboxylic acids (propionic, butyric, valeric, and hexanoic) with R_w = 1.5, shown in Figure 23, indicates that the hydrolysis of the intermediate is somewhat faster for propionic acid than for the other acids. The stability results are summarized in Table 8.

Table 8. Summary of solution stability

Carboxylic Acid	R_w	Period of Chemical Change
Propionic	1.0	N. A. (precipitates)
	1.5	35 hr
	2.0	9 hr
	3.0	0.45 hr
Butyric, Valeric & Hexanoic	1.0	130 hr
	1.5	80 hr
	2.0	35 hr
	3.0	9 hr

In addition to the chemical changes indicated by the growth and reduction of the bands, there also appears to be reproducible changes in the amount of Rayleigh scattering produced by the sample. These changes may be associated with the formation and depletion of colloidal particles formed by the reaction intermediate(s) which may have bonding patterns similar to those of the hexameric clusters previously isolated for acetic acid systems (Sanchez and Livage, 1990). However, the only incontrovertible evidence of particle formation occurs for the lowest water condition (R_w=1.0) with propionic acid, which produces a cloudy

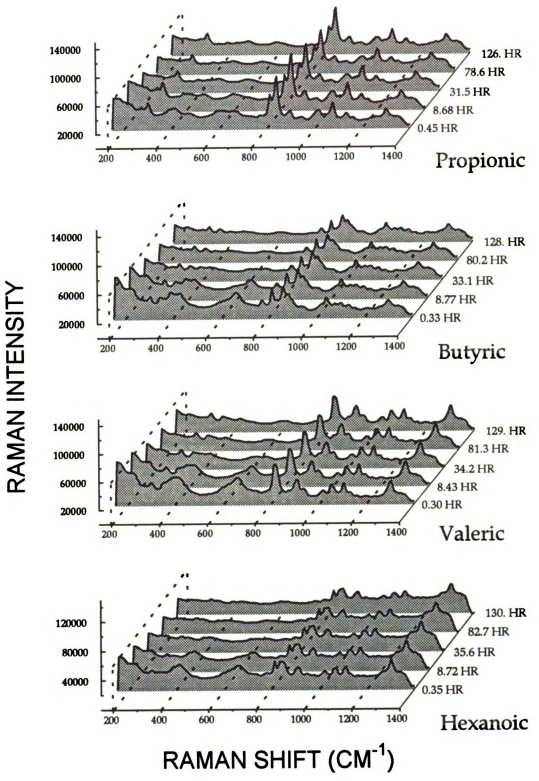

Figure 23. Raman spectra of aged titanium isopropoxide carboxylate solutions with an water to alkoxide ratios (R_w) of 1.5. From top to bottom, the carboxylic acids used were propionic, butyric, valeric, and hexanoic — all with an acid to alkoxide ratio (R_a) of 15.

precipitate. More water or longer acid chains produce clear solutions with no particles detectable with a Coulter N4 particle size analyzer (10 nm - 10,000 nm).

This Raman spectroscopic investigation of long-term solution reactions indicates that the coating solutions achieve a significant degree of stability for moderate levels of water addition ($R_w \leq 3.0$). Because of the limited degree to which the modified alkoxide can react with water, it is not critical for long-term results that the hydrolysis be 'controlled' by avoiding a local excess of water. Regardless of how the water is introduced, the end result is the same. Furthermore, if sufficient water is added ($R_w \geq 1.5$) the Raman spectra after 130 hours appear to be identical regardless of how much water was added (R_w=1.5, 2.0, or 3.0); within this concentration range, the amount of added water controls the rate of transformation but not the end product characteristics.

6.5. INFRARED CHARACTERIZATION OF SOLUTION AND FILM

The Circle® cell attachment was used to acquire spectra of liquid samples while the Germanium ATR crystal was used to examine the spectra of the films. These studies were especially useful in comparing the chemical states of the solutions and films since standard Raman and resonance Raman spectroscopy could not be used to analyze the film material which was an exceptionally poor Raman scatterer. Spectra for valeric acid-titanium isopropoxide derived coating solutions and films, made with and without water are presented to show the effect of acid and water concentrations on the chemistry of the system. It should be noted

that these films were not made with ethanol, so their chemistry may differ somewhat from that of the porphyrin-doped films.

In Figure 24, the spectrally observable effect of increasing valeric acid concentration on the no-water coating solution was primarily to strengthen the liquid valeric acid component of the spectrum. The growth of the bands, from (a) to (b) to (c), can be primarily attributed to increasing concentrations of unreacted valeric acid. When these solutions are cast as films, the spectra are almost exactly the same, as shown in Figure 25, except that a titanium isopropoxide band at 1130 cm^{-1} is still slightly apparent for the lowest concentration of valeric acid. However, when water is present, the effect of varying amounts of valeric acid becomes more critical. In Figure 26, the characteristic differences between the symmetric and asymmetric carboxylate vibrations can be used to show changes in the relative concentration of chelating and bridging carboxylate ligands. The narrow separation between symmetric and asymmetric bands would correspond to the chelating ligand, while the slightly broader separation would be associated with bridging ligand. Since the exact values of these characteristic separations are different for each acid-metal system, and since the separations for the chelating and bridging ligands are generally not too different, it would be difficult to accurately distinguish between these two ligand configurations if they were not both present. However, it should be mentioned that there is also a strong similarity between characteristic frequency separations of the free carboxylate ion and the bridging ligand. In any case, the increasing strength of the peaks corresponding to the larger separation are due to either an increasing relative concentration of the bridging

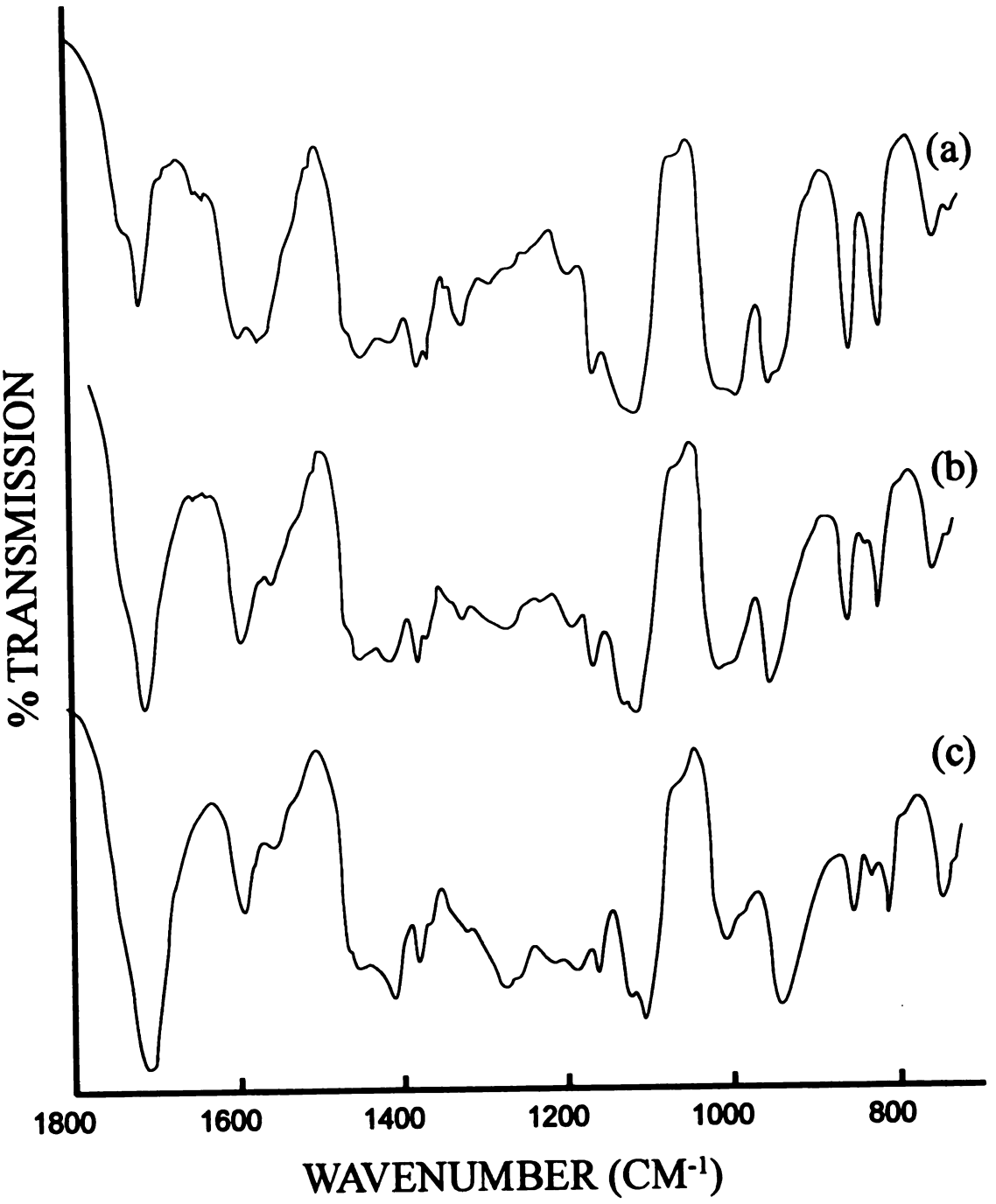

Figure 24. FTIR Circle® cell spectra of titanium isopropoxide-valeric acid coating solutions without added water for acid-to-alkoxide ratios of (a) 2.5, (b) 5.0, and (c) 10.0.

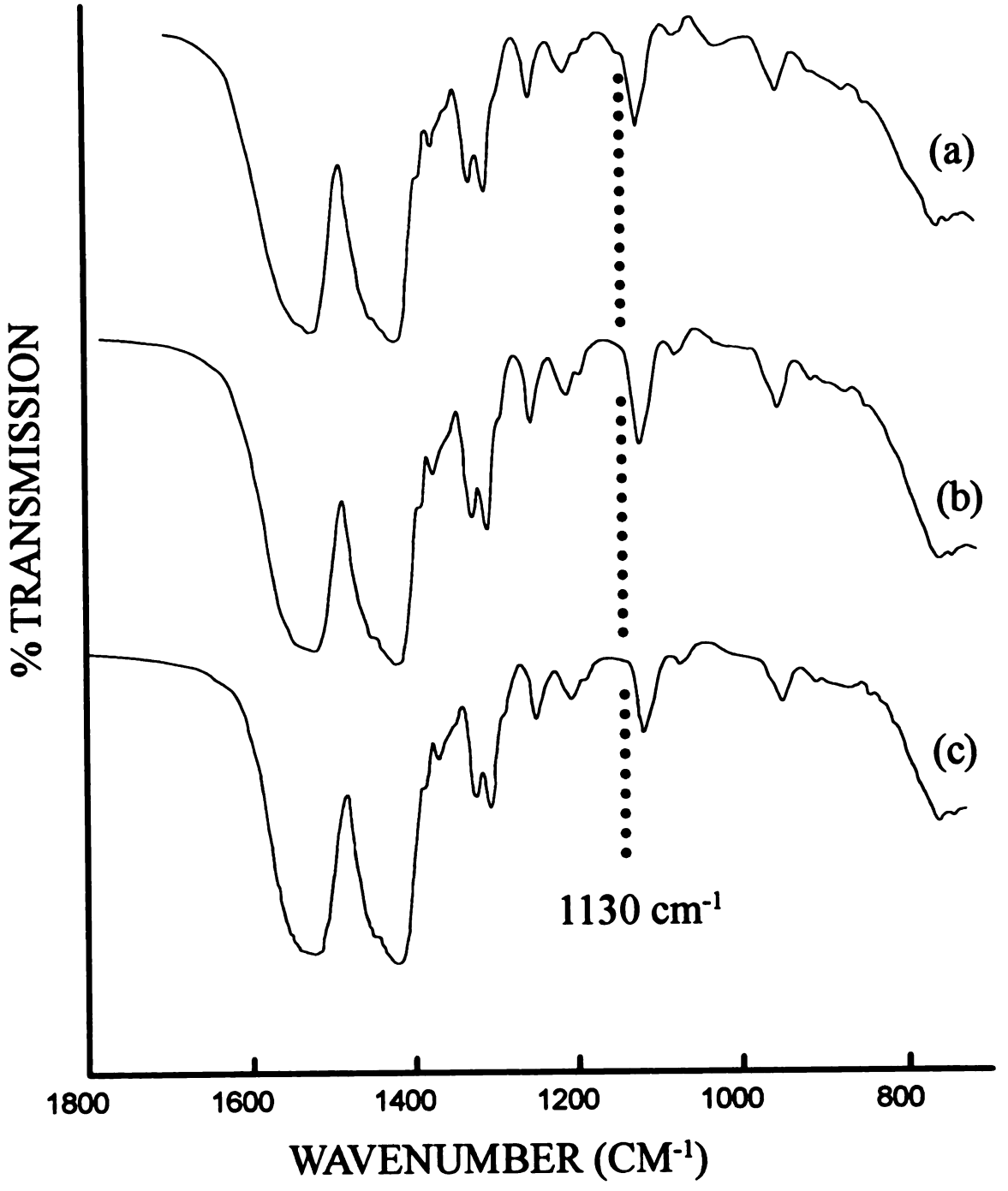

Figure 25. FTIR germanium ATR crystal spectra of titanium isopropoxide-valeric acid films made without added water for acid-to-alkoxide ratios of (a) 2.5, (b) 5.0, and (c) 10.0.

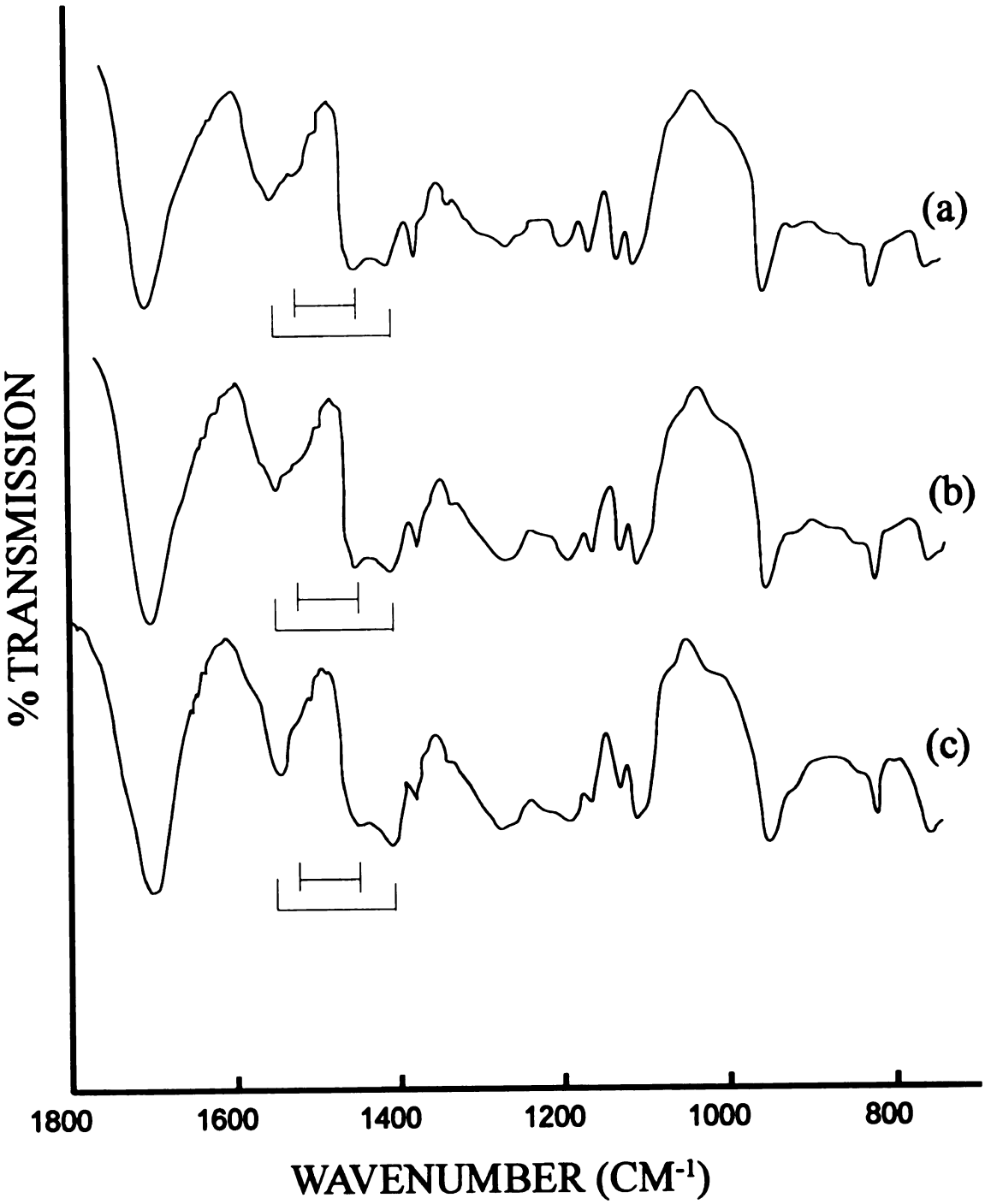

Figure 26. FTIR Circle® circle cell spectra of titanium isopropoxide-valeric acid coating solutions with added water for acid-to-alkoxide ratios of (a) 2.5, (b) 5.0, and (c) 10.0.

carboxylate ligand of the free carboxylate ion (which may form in the presence of the added water). When the added-water coating solutions are cast into films on a germanium crystals, the film spectra were obtained as shown in Figure 27. It is interesting to note that the band at 1130 cm^{-1}, associated with the titanium isopropoxide, was now apparent in all three spectra, decreasing in intensity with increasing concentration of valeric acid. Perhaps for the no-water film, this vibration of the alkoxy groups decreases due to μ-oxo bridging formations such as noted by Sanchez and Livage for acetate systems (1990) rather than by displacement of the alkoxy groups. This would allow for the bands to reappear with the addition of water, which may break the μ-oxo bridging. In any case, it appears that these non-aged, no-ethanol films retain some alkoxy bonds. It also appears that as the valeric acid concentration was increased, there was also a small increase in the proportion of bridging carboxylate ligands. These IR spectra support the structure recently proposed for these species (Van Vlierberge-Torgerson, 1992).

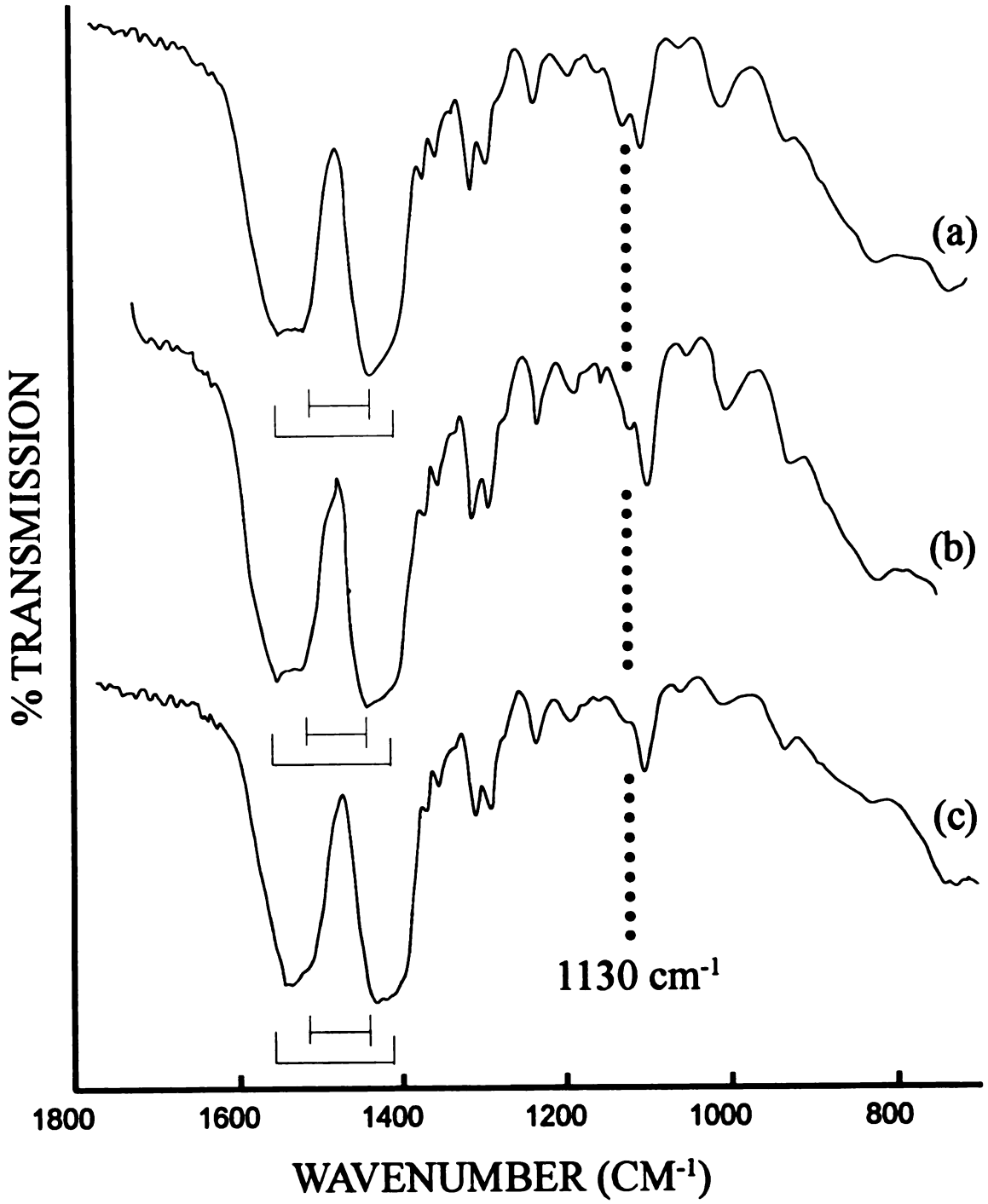

Figure 27. FTIR germanium ATR crystal spectra of titanium isopropoxide-valeric acid films made with added water for acid-to-alkoxide ratios of (a) 2.5, (b) 5.0, and (c) 10.0.

CHAPTER 7.

STRUCTURAL CHARACTERIZATION STUDIES

7.1. GRAVIMETRIC ANALYSIS

Mass measurements of plain and coated slides were taken with an electronic balance (Mettler AE50) to estimate the densities of the films. While the mass measurements could be made with good precision, there is considerable uncertainty due to distribution of the coating material. Since the films are very thin, any excess material deposited on or near the edge of the slides can cause significant error since the thickness of the film. For this reason, the density calculations should be taken as estimates for the upper bounds of the true values. The 99% confidence intervals for the measurements themselves are given in Table 9, and Table 10 gives the calculated densities. In calculating the 99% confidence intervals, the true value (μ) was calculated to exist within ($\bar{x} - k$, $\bar{x} + k$), where $\bar{x}$ is the mean measurement and k is expressed as $k = (2.576\sigma) / \sqrt{n}$, σ is the standard deviation, and n is the number of measurements (Kreyszig, 1988).

Table 9. The 99% confidence intervals for the various mass measurements used to estimate the film densities on 1" x 3" glass slides.

Plain Slide (g)	Coated Slide (g)	Difference (g)
Normal unheated fresh films:		
6.04584±0.00012	6.04668±0.00006	0.00084±0.00018
Normal unheated aged films[a]:		
6.04584±0.00012	6.04666±0.00007	0.00082±0.00019
Normal heated film:		
5.82145±0.00007	5.82203±0.00006	0.00057±0.00013
Ethanol modified unheated fresh films:		
5.82452±0.00004	5.82568±0.00010	0.00116±0.00014
Ethanol modified unheated aged films[b]:		
5.82452±0.00004	5.82564±0.00010	0.00112±0.00014
Ethanol modified heated films:		
6.04743±0.00007	6.04811±0.00012	0.00068±0.00019

[a]Aged 8 days. [b]Aged 10 days.

Table 10. The density of films made under various conditions.

Mass-Volume Density [g/cm^3]	Mass-Area Density [g/cm^2]
Normal unheated fresh films:	
1.45±0.31	(4.34±0.93)E-05
Normal unheated aged films[a]:	
1.41±0.32	(4.24±0.96)E-05
Normal heated film:	
0.99±0.22	(2.97±0.67)E-05
EtOH modified unheated fresh films:	
1.91±0.24	(5.72±0.71)E-05
EtOH modified unheated aged films[b]:	
1.93±0.24	(5.79±0.71)E-05
EtOH modified heated films:	
1.17±0.33	(3.52±0.98)E-05

[a]Aged 8 days. [b]Aged 10 days.

7.2. FILM THICKNESS DETERMINATION

The thickness measurements were made by scratching the films with a razor and then studying the contour of the scratch with an a Dektak IIA

profilometer (Sloan, Inc.). The standard 12.5 μm radius stylus was used, which should allow the probe to reach the full depth of the scratch. Except for the calibration run, the depth of the scratch was sampled every 0.5 μm with a rated accuracy of 5 Å.

The instrument was calibrated with a standard reference of etched silicon, 933 Å ± 5%, provided by the equipment's manufacturer (Sloan, Inc.). A typical calibration scan is shown in Figure 28(a), taken immediately prior to the acquisition of data. A typical scratch profile is shown in Figure 28(b). There is some uncertainty associated with the extent to which the glass itself may accidentally become scratched along with the film. However, it is usually assumed that no part of the scratch extends into the glass. The sample shown in Figure 28(b) shows a region, 200 μm into the scan, which may represent such a scratch into the glass. Another artifact which may affect film thickness measurements is the raised area or mound with often occurs on one side of the scratch. It is important to scan a large enough region to allow for the detection of such an artifact.

Typical film thicknesses for the titanium-based metalorganic films made with ethanol are shown in Table 11. For the multilayer coatings, each layer received a two minute drying under a heat gun. It should be noted that such multiple heat treatments significantly damage the porphyrin, making these films unsuitable for use in porphyrin based sensors, and they are included only for reference.

Table 11. Typical film thickness measurements for Ti-based films with ethanol.

One Layer	Two Layer	Four Layer
850±250 Å	2250±500 Å	5000±1000 Å

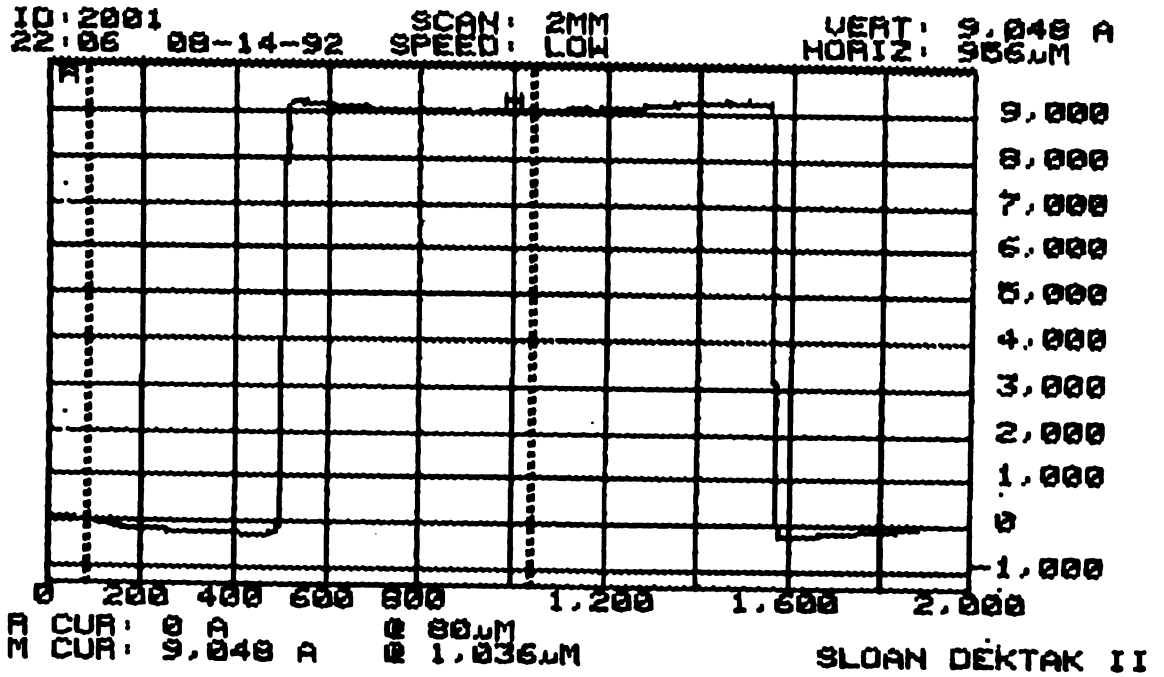

(a)

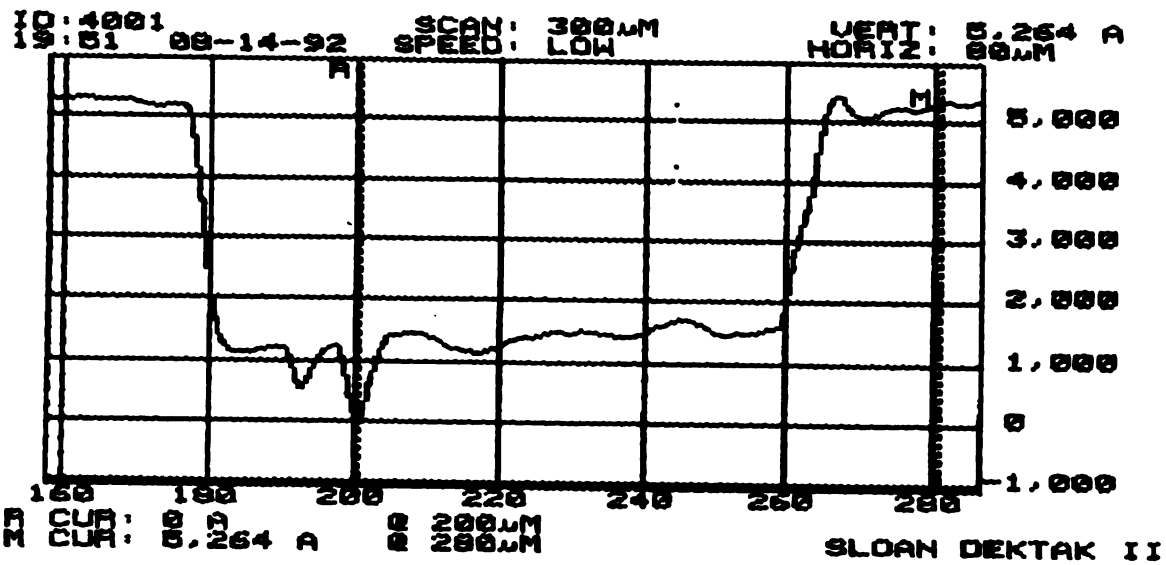

(b)

Figure 28. Sample profiles for (a) the silicon standard, and (b) a four layer film.

7.3. TRANSMISSION ELECTRON MICROSCOPY

The electron micrographs provide qualitative information about the structure of the film. The micrographs represent features distributed throughout the entire depth of the film -- a composite image of all features within the path of the electron beam. Consequently, when looking at a TEM of a very homogenous amorphous material containing very small features, it can be extremely difficult to determine the exact structure of the individual features from the image. A micrograph of a thin layer of coating material, shown in Figure 29, demonstrates an apparently random pattern of dark and light patches. The dark areas are more electron dense and the lighter areas are more electron transparent. For equal concentrations of carbon, oxygen, and titanium, the titanium would appear considerably darker than the oxygen and carbon. Although it is impossible to accurately calculate the average pore size from such a micrograph, is does serve to characterize the nature of the material. The micrograph provides direct evidence that the film is probably composed of a sponge-like network of very small structural components, and it indicates that the pores may well be in the 10-100 Å size range.

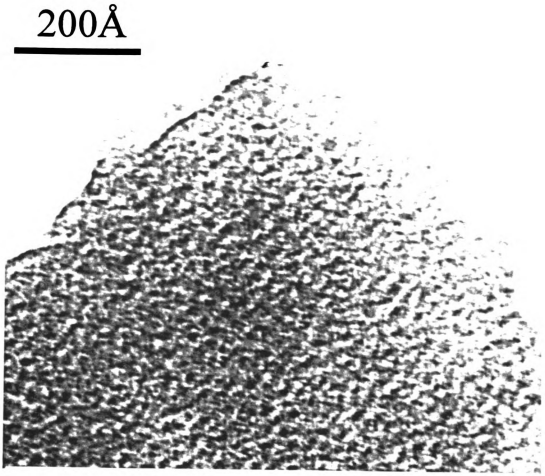

Figure 29. Transmission electron micrograph (TEM) of the film material applied directly to a copper grid and dried under strong air flow.

7.4. ATOMIC FORCE MICROSCOPY

While the transmission electron microscope provides a collective transmitted image of all the miniscule features within the thickness of the film, it does not clearly image the individual features themselves. When coated with a thin layer of gold (70 Å), the surface features of the film were entirely obliterated, and both scanning tunneling microscopy (STM) and scanning electron microscopy (SEM) showed only the image of the gold distributed on the surface of the film. Any patterns in the surface could only be attributed to the gold.

However, with atomic force microscopy (AFM), surface conductivity is neither necessary nor even beneficial. The tiny probe can easily image the surface features on a scale ranging from microns down to angstroms. A major limitation of this technique is that the atomically sharp probe is mounted on a rather obtuse pyramidal structure which is incapable of accurately imaging a deep and abrupt drop in the surface. Consequently, an abrupt hole in the surface may appear as a much more shallow and gradual depression than actually exists in the sample. This problem could be somewhat remedied by the use of high aspect ratio tips.

In spite of this drawback, a great deal of useful information may still be acquired with this instrument. Some of the larger surface features of a titanium-based metalorganic film are shown in Figure 30. As shown in the depth key, the lighter areas represent the high points on the surface while the darker areas represent depressions or holes. In this atomic force image, the surface appears like an aerial view of a continuous mountain range. The apparent valleys representing either gradual depressions or actual holes acting as the mouth of larger pore

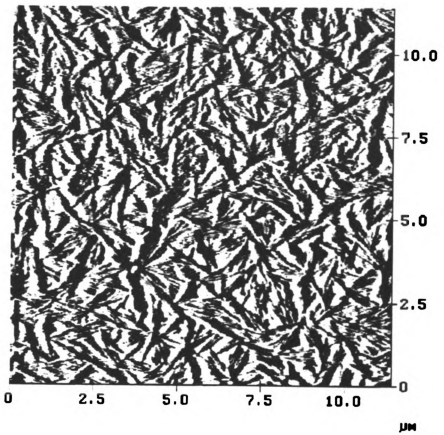

Figure 30. Atomic force micrograph (AFM) showing the larger scale surface features of a titanium-based metalorganic film.

channels. The interconnected ridges could well represent the surface of the structures from which the entire body of the film is composed. These ridges appear to be composed of segments which are generally 0.5 to 1.5 μm in length and represent the large scale features of the film.

Further magnification shows a network of features which might represent tiny hills and ridges in an otherwise continuous surface or they might be caused from an actual network of polymer strand- and fiber-like structures comprising the building blocks of the film material. These fiber-like structures can be clearly seen in Figure 31.

When one of these larger features is enlarged upon, a new world of structural information unfolds. The image displayed in Figure 32 shows these smaller structural features. Here again are a series of ridges and holes, although here the holes appear more rounded than the oblong valleys seen in the previous figure. The information contained in these AFM images strongly supports the theory of dual-scale pore structure.

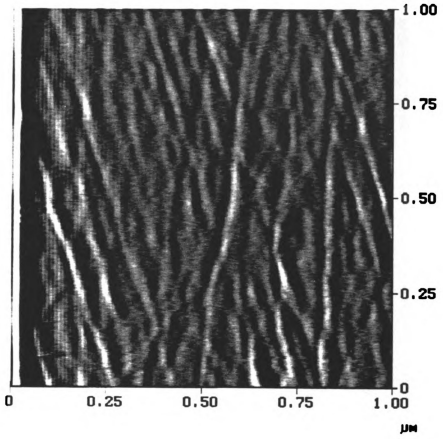

Microscope	NSIII AFM
Z range	0.5 nm
Scan size	1.0 µm
Number of samples	512
Scan rate	15.3 Hz
Setpoint	-1.5 V
Data type	Deflection

Figure 31. Atomic force micrograph (AFM) showing fiber-like structure under intermediate magnification.

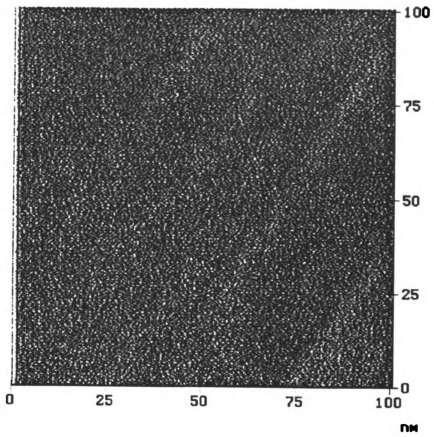

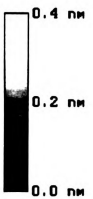

Microscope	NSIII AFM
Z range	0.4 nm
Scan size	100.8 nm
Number of samples	512
Scan rate	8.7 Hz
Setpoint	0.0 V
Data type	Deflection

Figure 32. Atomic force micrograph (AFM) showing the smaller scale surface features of a titanium-based metalorganic film.

CHAPTER 8.

DIFFUSION STUDIES

8.1. INSITU REDUCTION OF PORPHYRIN

The three porphyrins shown in Figure 13 have all been reduced within the titanium metalorganic film with hydrazine, sodium dithionite, or (photochemically) with UV light in a dilute solution of isopropanol and acetophenone. Hydrazine is the most convenient reducing agent since it is obtained as a ready-to-use aqueous solution. The sodium dithionite is more difficult to use, provided in the form of an air-sensitive solid. These two reducing agents must diffuse into the film before reducing the porphyrin. To photoreduce an Fe(III) porphyrin within the film, acetophenone and isopropanol must also be allowed to permeate the film prior to exposure to UV light. However, by mixing a small amount of acetophenone and benzophenone into the coating solution before the film is even made, the films need only be treated with isopropanol solution during UV exposure. The use of acetophenone, benzophenone, and isopropanol in the photoreduction of metal porphyrins has been previously reported (Ward and Chang, 1982). However, since the film material strongly absorbs in the UV region, the success of the photoreduction within the film was not entirely predictable. The absorption spectra showing the reduction, the formation of the carbonyl ligand, and the re-oxidation are shown in Figures 33 - 34.

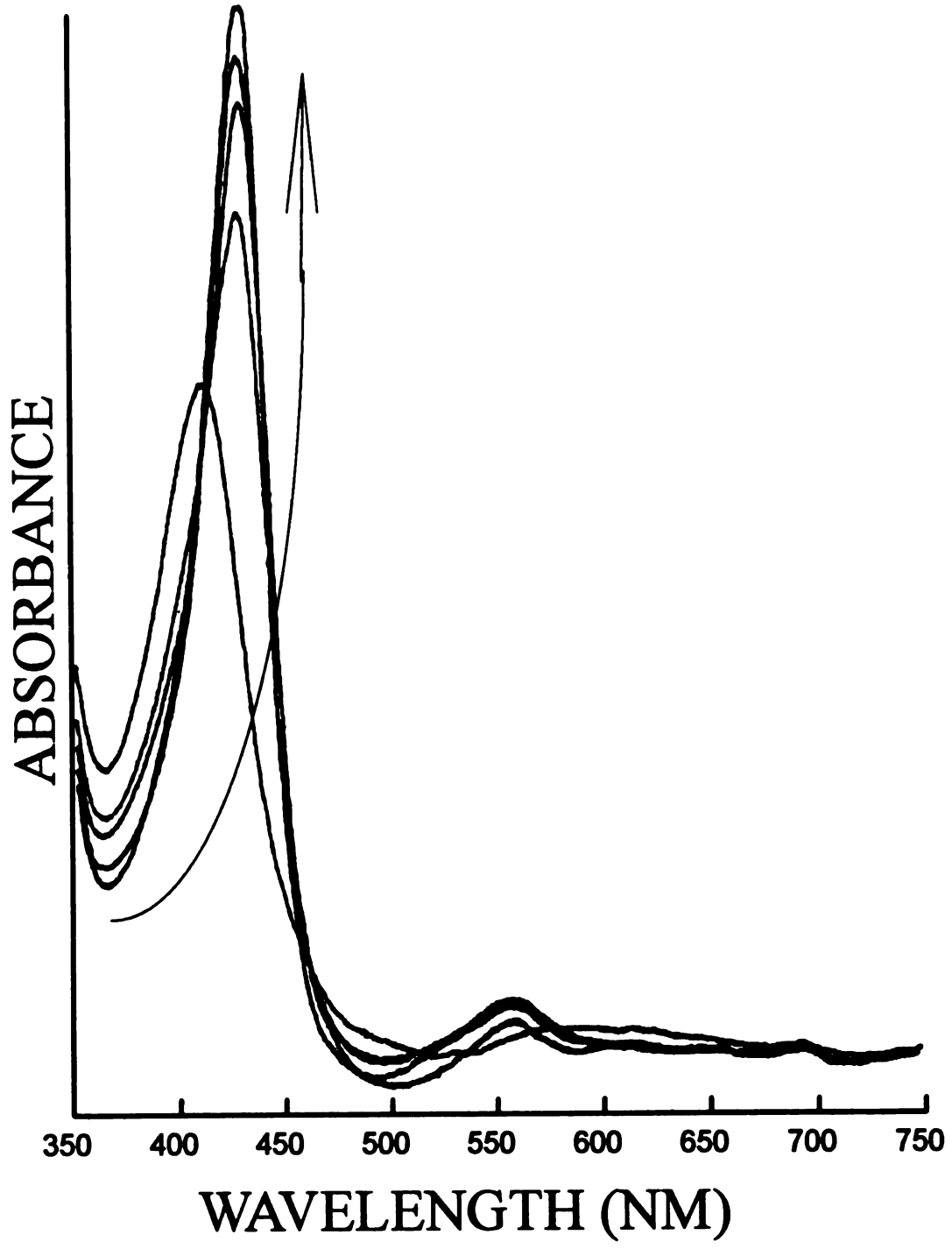

Figure 33. Absorption spectra of P1 in a titanium metalorganic film showing the photoreduction of P1 by 254 nm light in an aqueous solution of acetophenone and isopropanol. The arrow shows the progression over time, starting with the Fe(III) porphyrin.

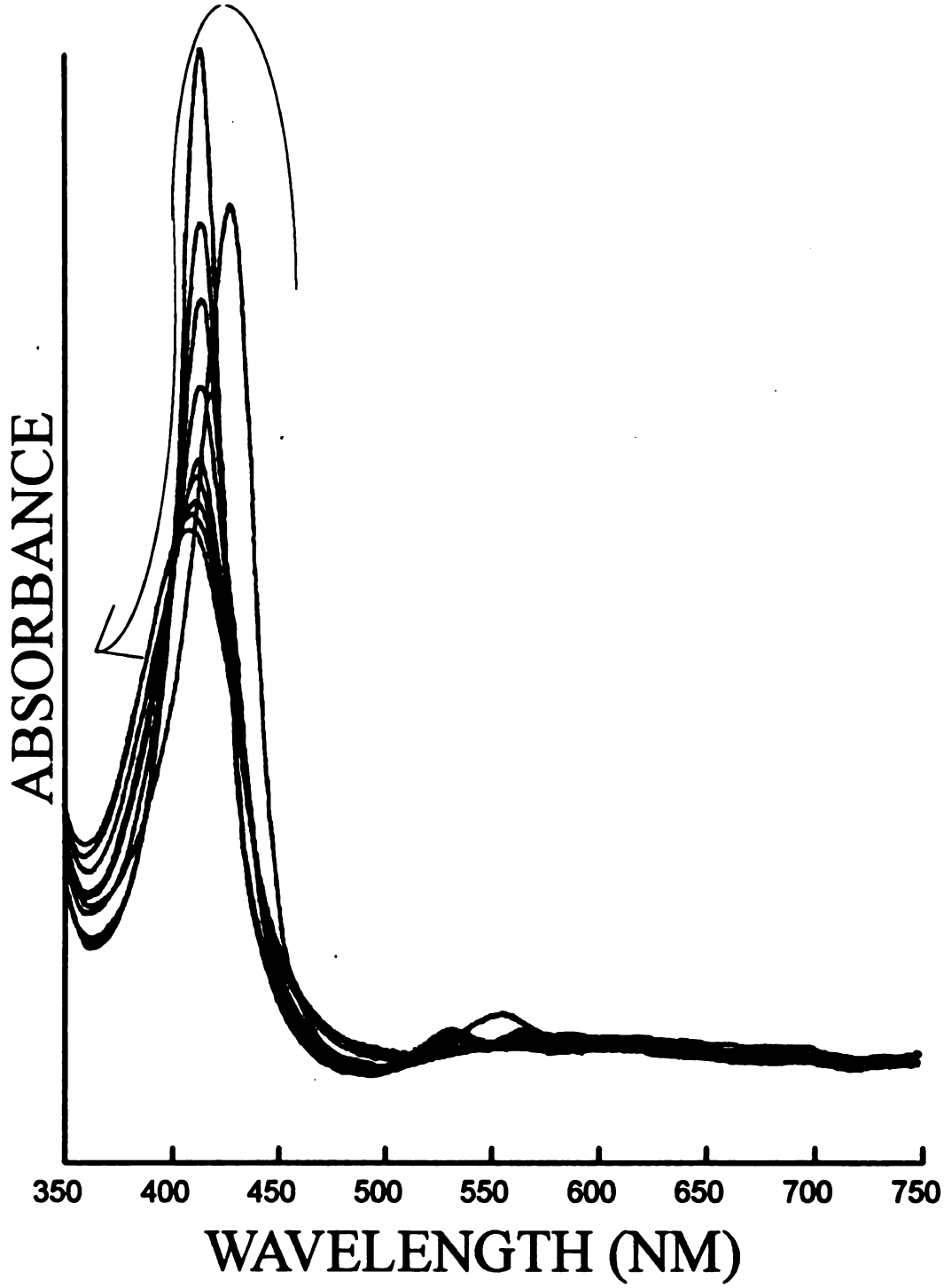

Figure 34. Absorption spectra of P1 in a titanium metalorganic film showing the effects of exposure to CO and re-oxidation by solvated O_2. The arrow shows the progression from the photoreduced Fe(II) porphyrin, to the Fe(II)-CO complex, to the Fe(III) state.

8.2. DIFFUSION OF CARBON MONOXIDE

The results of the diffusion study are shown in Figures 35 - 37. The Soret band (~ 415 nm) of P1 in the film is shown for various CO concentrations. The relative intensities and positions of the Soret band for the Fe(III), Fe(II), and Fe(II)-CO states reveal the extent of carbonyl ligand formation after approximately twenty minutes exposure to the CO solutions. The hydrazine not only reduces the Fe(III) P1, it also is weakly retained by the porphyrin as a ligand. Even CO concentrations as low as 70 ppb (Figure 5 (c)) show an increase in the Soret band magnitude and a measurable shift to lower wavelength.

To quantify the changes in the absorption spectrum due to the formation of the carbonyl ligand, it was necessary to normalize the data taken from different films. The baseline corrected absorbance intensity (BCAI) was measured at 414 nm (I^*_{414}) and 419 nm (I^*_{419}) after 30 minutes of film exposure to the hydrazine solution (the asterisk will be used to denote measurements in the presence of hydrazine). Then, after exposure to the CO solution, the BCAI was monitored at 414 nm (I_{414}), the Soret band position for P1 Fe(II)-CO complex. The normalized response to CO was then calculated as $R(t) = R_{PI}(t) - R_O$, where $R_{PI} = I_{414} / I^*_{419}$ and $R_O = I^*_{414} / I^*_{419}$. Figure 35 shows the development of R(t) over a period of ~1 hr for various CO concentrations. From this figure, it is apparent that the initial rate of response to CO changes abruptly prior to the collection of data, and it is also apparent that this initial period accounts for a large percentage of the total response. This would indicate that the porphyrin is not uniformly accessible within the film. The diffusion of benzoate through the film was previously shown to have a diffusivity of

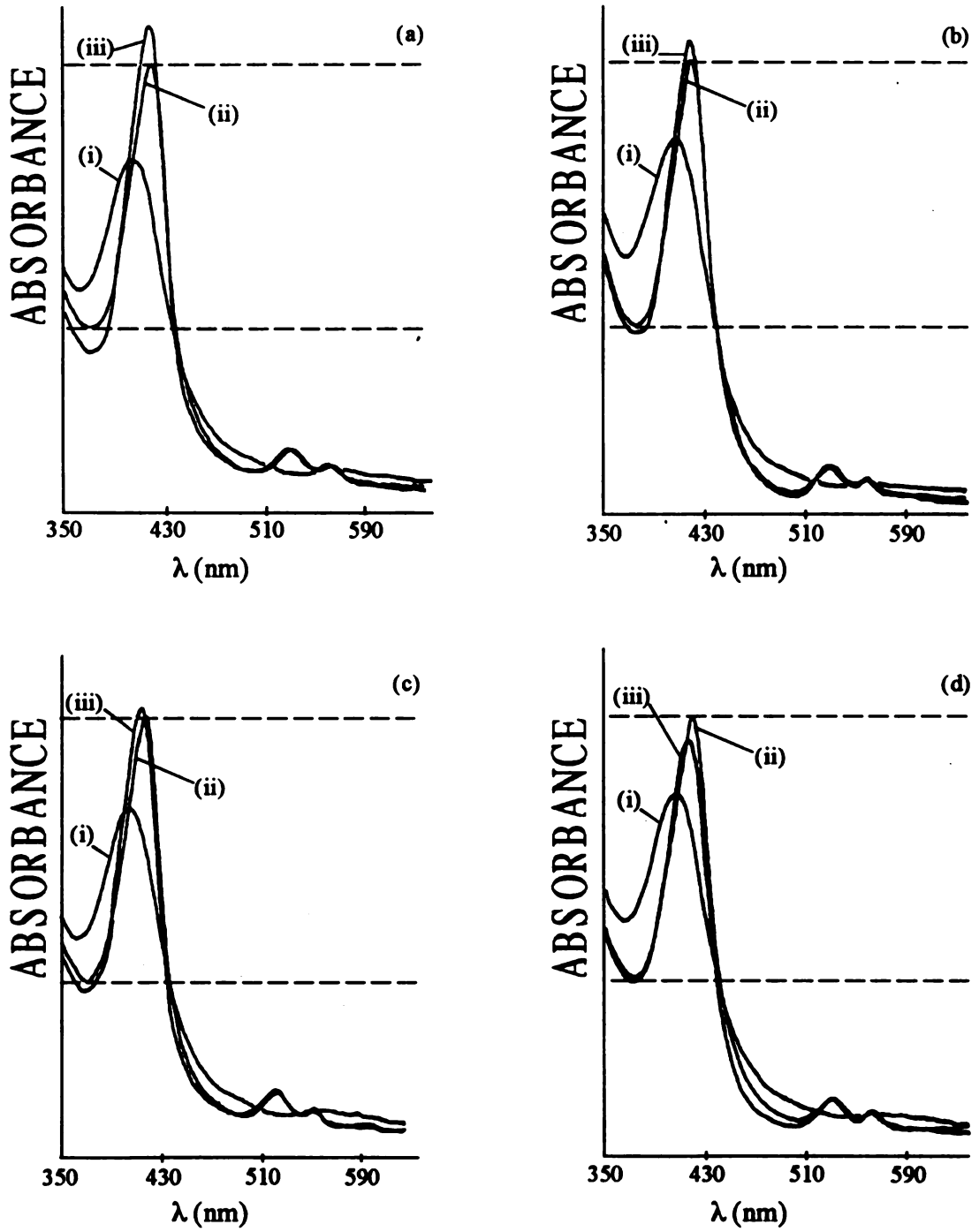

Figure 35. Absorption spectra showing the response of P1-doped titanium metalorganic films to various concentrations of carbon monoxide in aqueous solution: (a) 1000 ppb, (b) 170 ppb, (c) 70 ppb, (d) 0 ppb. Absorbance spectra were taken (i) before reduction with hydrazine, (ii) after reduction, and (iii) after removal of hydrazine solution and exposure to the carbon monoxide solution.

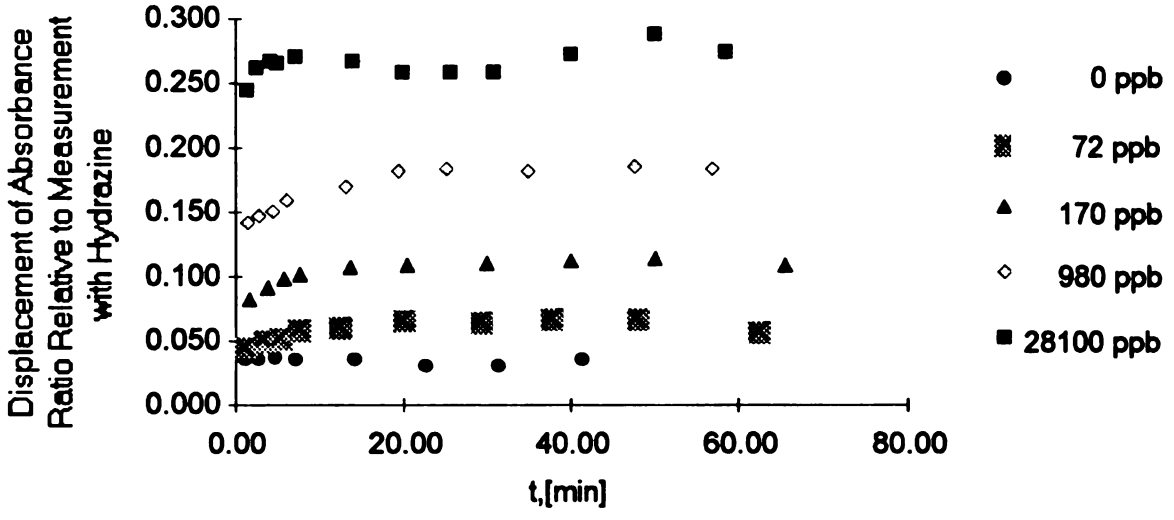

Figure 36. Carbon monoxide diffusion into P1-doped titanium metalorganic films. The displacement ($R(t) = R_{PI}(t) - R_O$) of the absorbance ratio ($R_{PI}(t)$) relative to measurement with hydrazine (R_O) is shown for t between 0 and 60 minutes.

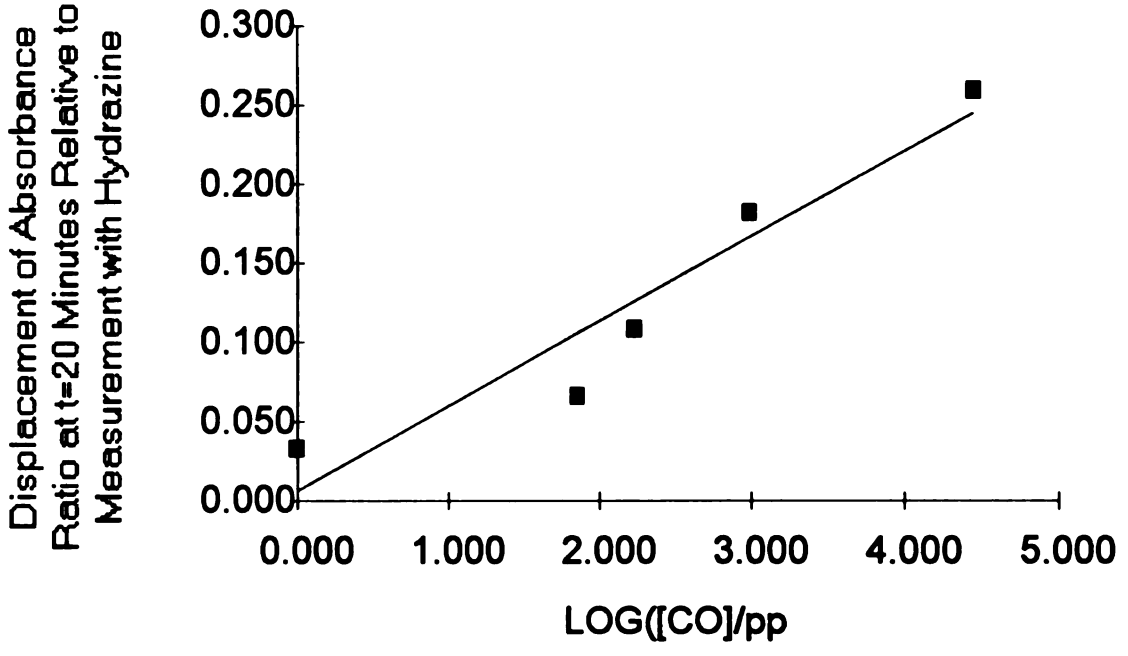

Figure 37. Response of P1-doped titanium metalorganic films to various CO concentrations after 20 minutes of exposure to the CO solution. The displacement ($R(20) = R_{PI}(20) - R_O$) of the absorbance ratio ($R_{PI}(20)$) relative to measurement with hydrazine (R_O) is shown for CO solutions ranging from 0 to 28,100 ppb.

no less than $1x10^{-12}$ cm^2/s (Dulebohn et. al., 1990). Ignoring the initial response, the diffusivity of CO appears to be on the order of $1x10^{-14}$ cm^2/s, which is comparable to diffusion in dense solids. A likely explanation for these results is that there is a large pore size distribution within the material; many porphyrin molecules are directly accessible to larger pore channels, while some of the porphyrin remains isolated within less permeable, smaller-pore regions.

In Figure 36, the CO response after 20 minutes of exposure was compared for various CO concentrations. The response was shown to vary linearly with the log[CO], with a correlation coefficient of 0.91. Although this is only an empirical correlation, it indicates that the films can be calibrated over a very wide concentration range. The correlation also shows that saturation of sensing properties requires relatively high CO concentrations.

8.3. MULTILAYER FILM SYSTEMS

It has been noted in previous studies (D. Dunuwila, to be published) that transport of cyanide through a single film is not noticeably slower than transport through a film coated with a clear layer not containing any porphyrin. To explain this phenomenon, in conjunction with the fact that a portion of the porphyrin sites seem to react immediately while the remainder react very slowly, it is necessary to realize that not all porphyrin sites have equal accessibility within the film. To address this condition, we have proposed the large-pore dense-fiber model which will be discussed in the next chapter.

The films used in the CO diffusion studies have been dried with a heat gun. If a non-doped but otherwise identical film were to be cast over the first and also dried with a heat gun, the cumulative thermal degradation of the porphyrin would become noticeable. Thus, it is not possible to perform multilayer diffusion studies on film assemblies made in this way. It has, however, been verified that diffusion of CO through a non-heated second coating is not noticeably slower than through a non-coated film.

CHAPTER 9.

MODELING SYSTEM RESPONSE

9.1. FUNDAMENTAL CONCERNS

To interpret the results of the diffusion of CO into the metalorganic membrane, it is necessary to understand the range of phenomena which can affect these results. An understanding of the relative magnitude of these effects can then be developed through system modeling.

Factors to consider include the hindrance of solute due to interaction with the pore wall, the tortuosity of the pores, the kinetics and equilibria of the porphyrin Fe(II)-CO interaction, the distribution factor of the CO between the solution and the membrane, and the boundary layer resistance. The morphology of the membrane material, the thickness of the film, and the concentration of immobilized porphyrin also affect the response of the porphyrin to the CO.

The hindrance of the solute depends upon the nature of the chemical interaction existing between solute and membrane material and on the ratio of the solute and pore diameters. The chemical interaction must be either repulsive, inert, or attractive, and the nature of the interaction becomes increasingly important as the ratio of solute to pore diameters increases toward unity. The chemistry of the interaction affects the distribution factor and strength of adsorption (if any) of the solute to the membrane. In our system, very little is known about

the CO-membrane interaction. The interaction of the solvent and the membrane is also important since it affects the wetability of the material, which may, in turn, affect the effective pore size. Water (the solvent) is highly repelled by the hydrophobic membrane, and the hydrophobicity may effectively decrease the size of the pores through which the CO diffuses. It should also be mentioned that since the degree of hydrophobicity is determined by the amount and nature of the organic material in the membrane, and since the degree of carboxylate retention can be reduced by heating, it follows that the hydrophobicity can be controlled through heating.

The distribution factor is defined by $K \equiv C_{bulk}/C_{mem}$ where C_{bulk} and C_{mem} are the bulk and membrane solute concentrations at equilibrium, respectively (Crank, 1975). The hindrance due to collisions with the pore wall has been described by the Rankin equation (Cussler, 1984):

$$\frac{D}{D_o} = 1 + \frac{9}{8}\lambda \ln\lambda - 1.51 + O(\lambda^2) \qquad (7)$$

where

$$\lambda = \frac{2R_o}{d}$$

D_o = original diffusion coefficient

D = effective diffusivity

R_o = molecular radius of solute (1.11 angstroms)

d = pore diameter

The Rankin equation is usually valid within 2% error for $\lambda < 0.2$. By measuring the effective diffusivity of the solute in the membrane, the effective pore diameter can be estimated. The atomic radii for triply

bonded carbon (0.60 Å) and oxygen (0.51 Å) yielded a molecular radius, R_o, of 1.11 Å (Lang's Handbook, 1974). Thus, the Rankin equation should be accurate to within 2% for pore diameters, d, greater than 11.10 Å. The effect of the molecular and pore diameter ratio on effective diffusivity is shown in Table 12. From the tabulated values, it is apparent that the maximum reduction in diffusivity which can be accurately predicted (within 2%) by this equation corresponds to a factor of 1/3.

Table 12. The effect of the molecular and pore diameter ratio on diffusivity, D (D_o is the unhindered diffusivity).

Molecular diameter / pore diameter	D/D_o
0.2	0.33
0.1	0.587
0.01	0.933
0.001	0.991

The tortuosity, τ, adjusts the diffusivity to account for pore lengths which are longer than the thickness of the membrane due to bending and branching of the pores. The effective diffusivity is given by $D_{eff}=D/\tau$ (Cussler, 1984).

Over a dilute concentration range, any adsorption of carbon monoxide to the membrane material can be assumed to occur with a linear isotherm. One could assume the mechanism would be physical rather than chemical adsorption and the effect on diffusion would be to effectively lower the diffusivity of the solute with the membrane. The linear isotherm can be represented as A=RC, where A is the adsorbed solute concentration, C is the free solute, and R is a constant. Then, the diffusion equation

$$\frac{\partial C}{\partial t} = D \frac{\partial^2 C}{\partial x^2} - \frac{\partial A}{\partial t} \quad (8)$$

becomes

$$\frac{\partial C}{\partial t} = \left(\frac{D}{1 + R}\right) \frac{\partial^2 C}{\partial x^2} = D' \frac{\partial^2 C}{\partial x^2} \quad (9)$$

Hence, any adsorption of the carbon monoxide on the membrane material would have the effect of lowering the effective diffusivity by a factor of (1/(1+R)). Furthermore, if the adsorption was very great, an extremely poor response would be expected for dilute carbon monoxide, which is not observed. Thus, the effect of CO adsorption on the membrane material can be expected to have relatively little impact on the overall behavior of CO diffusion.

In addition to the possible physical adsorption of carbon monoxide to the membrane, the system has definite chemical adsorption of the solute to the discrete Fe(II)-porphyrin sites. The differential model for diffusion is then given by:

$$\frac{\partial C}{\partial t} = D \frac{\partial^2 C}{\partial x^2} - \frac{\partial S}{\partial t} \quad (10)$$

$$\frac{\partial S}{\partial t} = \mu C P - \sigma S \quad (11)$$

where

μ = the forward rate constant
σ = the reverse rate constant
$S = P_o - P$ = adsorbed solute concentration
P_o = initial concentration of adsorption sites
P = current concentration of adsorption sites
C = solute concentration

In cylindrical coordinates, the equations are expressed as

$$\frac{\partial C}{\partial t} = D \frac{\partial}{r \partial r}\left(r \frac{\partial C}{\partial r}\right) - \frac{\partial S}{\partial t} \qquad (12)$$

$$\frac{\partial S}{\partial t} = \mu CP - \sigma S \qquad (13)$$

Solutions to this system of nonlinear equations can be estimated by first linearizing the equations, and then solving analytically or numerically.

9.2. LARGE PORE-DENSE FIBER MODEL

The diffusion data is consistent with a large pore-dense region model of the membrane material. If we assume the geometry of these dense regions to be in the form of cylindrical polymer strands, then we could model the system with a large pore-dense fiber model. The chemistry of the system should favor linear growth of the polymer molecules and certain AFM images shown in Figures 30-32 may also indicate the existence of strand-like features on the surface of the film. However, the true geometry and existence of such regions has not yet been conclusively demonstrated.

In viewing the system in this way, the relative times for diffusion in the porous and dense regions are of significant importance. If the time scales are sufficiently different, the two processes can be treated independently, rather than as a single coupled problem.

To prove the two processes are highly uncoupled, it is not even necessary to solve the differential equations which describe the CO diffusion through porphyrin-doped media. The rate of the fast diffusion through large pore regions can be bounded by solving the problem for adsorption with a linear isotherm. This solution will show diffusion

behavior which is slower than for limited-site adsorption, and may therefore serve to bound the more complicated problem. Since this solution is needed to provide an upper bound for the time required for the large pore diffusion process, estimated parameters should all be chosen to yield the slowest diffusion possible. Even with very heavy adsorption, pore hindrance for a solute only 20% smaller in diameter than the pore, and a tortuosity of 10, the effective diffusivity would probably not be smaller than 10^{-7} cm/s. Reducing this further by two orders of magnitude and assuming a film thickness of 3000 Å (which is more than three times the mean value), the diffusion process still requires only 10 s to allow permeation of the film. The calculation is shown in appendix B.

Next, consider the diffusion into the denser regions of the material. The concentration of porphyrin is 0.058 M, which would indicate that if the porphyrin were uniformly distributed throughout the volume of the film, the average inter-porphyrin distance would be 31 Å; if the porphyrin were distributed evenly on a mass rather than volume basis, the average inter-porphyrin distance would be even smaller since the volume of the void space would now be excluded. For example, if the material were composed of polymer strands that were 25 nm in diameter, packed with 15 % void space, the average inter-porphyrin distance would be reduced slightly to 29 Å. The radius of the strand would be 145 Å, and 19 % of the porphyrin contained in the strand would be in the outer 10 % of the radius or 14.5 Å, followed by 17 % in the second 1/10th radius layer, etc. Returning to the rectangular coordinate system and thinking in general terms, if the distance which characterized the denser region diffusion ranged from 50-300 Å and the characteristic

time was approximately 15 minutes to complete the process, then the diffusion coefficient would range between 3E-15 and 1E-13 cm^2/s, which corresponds to typical values for solid-state diffusion. The justification for this line of reasoning is treated in appendix C.

Although the data acquired for the diffusion of CO into the films does not allow for the accurate deconvolution of the Soret band contributions from the Fe(II) and Fe(II)-CO porphyrins, it does demonstrate that the equilibrium constant for the CO-ligand formation within the film is probably between 10,000 and 100,000 M^{-1}. Values for the concentration of Fe(II) and Fe(II)-CO porphyrins are labeled [P] and [S], respectively; some values of [P] and [S] are shown in Table 13 as functions of initial CO concentration and equilibrium constant. Given that the initial concentration of P_o=0.058 M, the percentage of ligand formation can be calculated from [S], as shown in the last column of Table 13. When Keq=100000, the progression from 70 to 170 to 980 ppb is accompanied by 20%, 37%, and finally 77% ligand formation. Each time the concentration is increased, the % of ligand formation is almost doubled. When Keq=10,000, the same progression through increasing initial CO concentrations yields 2.4%, 5.7%, and then 26% ligand formation. The first increase more than doubles the ligand formation and the second increase raises ligand concentration by more than 4.5 times. From Figure 36 it is apparent that the behavior of the CO-Fe(II)-porphyrin system lies between the response calculated for Keq values of 100,000 and 10,000 M^{-1}. Thus, it is likely that these values bracket the value for Keq within the film.

Table 13. Effect of Keq on extent of ligand formation.

initial [CO], M	Keq, 1/M	[P], M	[S], M	[S]/[P]	$[S]/[P]_o$
2.50E-06	10000000	0.00252	5.548E-02	2204.21%	95.66%
(70 ppb)	1000000	0.01766	4.034E-02	228.43%	69.55%
	100000	0.04663	1.137E-02	24.38%	19.60%
	10000	0.05659	1.410E-03	2.49%	2.43%
	1000	0.05786	1.446E-04	0.25%	0.25%
	100	0.05799	1.446E-05	0.02%	0.02%
	10	0.05800	1.446E-06	0.00%	0.00%
	1	0.05800	1.446E-07	0.00%	0.00%

initial [CO], M	Keq, 1/M	[P], M	[S], M	[S]/[P]	$[S]/[P]_o$
6.07E-06	10000000	9.888E-04	5.700E-02	5764.56%	98.28%
(170 ppb)	1000000	8.522E-03	4.948E-02	580.61%	85.31%
	100000	3.635E-02	2.165E-02	59.56%	37.33%
	10000	5.469E-02	3.310E-03	6.05%	5.71%
	1000	5.765E-02	3.498E-04	0.61%	0.60%
	100	5.796E-02	3.519E-05	0.06%	0.06%
	10	5.800E-02	3.520E-06	0.01%	0.01%
	1	5.800E-02	3.521E-07	0.00%	0.00%

initial [CO], M	Keq, 1/M	[P], M	[S], M	[S]/[P]	$[S]/[P]_o$
3.50E-05	10000000	1.667E-04	5.783E-02	34691.06%	99.71%
(980 ppb)	1000000	1.625E-03	5.638E-02	3469.54%	97.21%
	100000	1.296E-02	4.504E-02	347.53%	77.66%
	10000	4.299E-02	1.501E-02	34.92%	25.88%
	1000	5.604E-02	1.961E-03	3.50%	3.38%
	100	5.780E-02	2.023E-04	0.35%	0.35%
	10	5.798E-02	2.029E-05	0.03%	0.03%
	1	5.800E-02	2.030E-06	0.00%	0.00%

SUMMARY AND RECOMMENDATIONS

The most important features of this investigation are summarized in the following statements:

1) Ferriheme concentrations of 0.058 M were achieved in highly porous, optically clear, metalorganic films. The films were derived from mixtures of titanium isopropoxide, valeric acid, water, and ethanol.

2) The porphyrins were securely incorporated using carboxyl, hydroxyl, and pentafluorophenyl substituents which chemically bind to the film material.

3) The Fe(III)-porphyrins could then be reduced insitu to the Fe(II) state which is capable of binding with carbon monoxide.

4) The chemistry of the film solutions was studied and the presence of a reactive intermediate was observed using Raman and infrared spectroscopies. It is likely that the intermediate has bonding patterns similar to the species which has been isolated and crystalized from titanium isopropoxide-acetic acid systems by Sanchez and Livage (1990). The slow hydrolysis kinetics are observed under a variety of water concentrations and for various carboxylic acids in addition to valeric acid.

5) The physical structure of the films was studied with TEM and AFM techniques, showing both internal and topographical features. The interpretation of the AFM images is especially difficult because the technique is still so new. The fiber-like features which were clearly resolved on the film surface could be due to either a wavy unevenness in an otherwise continuous surface or to actual strand- or fiber-like components which may comprise the substance of the film. At higher magnification, a secondary structure of fine depressions or holes was also observed which was visually similar to the patterns seen with the TEM. However, it must be stressed that the fiber-like features are not contradictory to or incompatible with the TEM images.

6) The carbon monoxide diffusion studies showed the Fe(II)-porphyrin-doped films could be used for sensing applications, which was the primary purpose for the development of the films. The films responded to aqueous CO levels below 70 ppb.

7) The diffusion results indicated that not all the porphyrin was equally accessible to the CO, indicating that the internal structure of the membrane contained both porous and dense regions. The diffusion through the large-pore regions was too fast to measure with the apparatus and methods used. However, the diffusion into the denser regions required up to twenty minutes to cover very small distances, indicating an effective diffusivity on the order of 10^{-14} cm^2/s. The equilibrium coefficient for the CO-ligand formation within the film was also estimated to be on the order of 10,000-100,000 M^{-1}

During the course of the current investigation, several observations were made concerning additional experiments which would be of significant value. The recommendations for future work includes the following items:

1) Explore the effects of drying freshly made films under high vacuum at ambient or moderate temperatures which will not damage the iron porphyrin. Increased removal of organic material makes the films less hydrophobic, and lower drying temperatures may result in less shrinkage of pores. This process may result in films with a negligible percentage of high density material, thereby providing a cleaner, more step-like response to a detectable solute.

2) Explore effect of adding inert solvents such a n-pentane, n-hexane, or n-heptane to film solutions followed by high-vacuum drying. This may result in thinner, lower-density films.

3) The role of the film in stabilizing or destabilizing the Fe(II) state of the porphyrin should be carefully studied. In particular, the redox chemistry and photochemistry of the material may affect the uptake, storage, and release of oxygen which would strongly influence the stability of the Fe(II) state.

4) Multilayer assemblies should be made using the high-vacuum drying technique, and a larger solute, such as t-butylisocyanide should be used to study the diffusion through 2, 3, and 4 layer systems (with only one porphyrin-doped bottom layer).

5) The temperature dependence of sensing molecules with two or more film-anchoring groups, such as -COOH, should be tested. The expansion or contraction of the film may provide enough molecular distortion to cause a change in compound's adsorption spectrum.

6) The general methods of securely attaching an iron porphyrin within the film material (via carboxyl, hydroxyl, and pentafluorophenyl groups) should be applied to catalysts. A good candidate for such a study would be ferrocene modified by the addition of a carboxylic acid substituent.

7) The Fe(II) porphyrin-doped films seem ideal for highly sensitive low-level oxygen detection, and their sensitivity should be quantified. The films may well be orders of magnitude more sensitive to oxygen than to carbon monoxide.

APPENDIX A

Tabulated Diffusion Data

This appendix contains sample UV-vis absorption data for various runs. The temperature, pressure, and concentration of the CO saturated stock solutions, as well as the dilution (if any) used in the diffusion study are listed above each table. The column headings 419, 414, 376, and 482 refer to wavelengths in nanometers at which the absorbance was measured after various periods of exposure to the CO solution. The headings 419c and 414c refer to baseline corrected absorbance readings at 419 nm and 414 nm respectively, where the baseline was estimated by linear interpolation between the absorbance readings at 376 nm and 482 nm. The bottom line labled 'reference' shows absorbance data while the film is still exposed to the hydrazine solution; 'time' here indicating the duration of this exposure.

Run #1: saturated CO solution
745.0 mmHg
22.5 deg celcius
Stock CO concentration: 28.11 ppm
CO solution as used: 28.11 ppm

time		time(min)	419	414	376	482	419c	414c
1	30	1.50	0.2715	0.2515	0.1685	0.0890	0.1353	0.1115
2	30	2.50	0.2725	0.2530	0.1680	0.0890	0.1365	0.1133
4	00	4.00	0.2730	0.2535	0.1680	0.0890	0.1370	0.1138
5	00	5.00	0.2735	0.2535	0.1680	0.0895	0.1373	0.1136
7	00	7.00	0.2738	0.2538	0.1680	0.0890	0.1378	0.1141
14	00	14.00	0.2735	0.2535	0.1680	0.0890	0.1375	0.1138
19	50	19.83	0.2730	0.2520	0.1670	0.0890	0.1376	0.1130
25	30	25.50	0.2735	0.2525	0.1680	0.0890	0.1375	0.1128
30	38	30.63	0.2735	0.2525	0.1680	0.0890	0.1375	0.1128
40	00	40.00	0.2735	0.2525	0.1660	0.0880	0.1391	0.1145
50	11	50.18	0.2745	0.2535	0.1650	0.0880	0.1407	0.1161
58	30	58.50	0.2755	0.2545	0.1680	0.0895	0.1393	0.1146
1 12	50	72.83	0.2735	0.2525	0.1655	0.0880	0.1394	0.1148
reference:								
0 45	00	45.00	0.2500	0.2345	0.1800	0.0930	0.1053	0.0857

Run #2: diluted CO solution
745.0 mmHg
22.5 deg celcius
Stock CO concentration: 28.11 ppm
Diluted CO solution: 0.9776 ppm

time		time(min)	419	414	376	482	419c	414c
1	20	1.33	0.3185	0.3190	0.1430	0.0740	0.2035	0.2007
2	50	2.83	0.3190	0.3200	0.1430	0.0740	0.2040	0.2017
4	20	4.33	0.3205	0.3210	0.1430	0.0745	0.2053	0.2026
6	00	6.00	0.3215	0.3225	0.1430	0.0740	0.2065	0.2042
12	59	12.98	0.3225	0.3235	0.1420	0.0735	0.2083	0.2061
19	24	19.40	0.3245	0.3255	0.1415	0.0740	0.2104	0.2082
25	10	25.17	0.3240	0.3250	0.1405	0.0735	0.2107	0.2085
34	44	34.73	0.3245	0.3245	0.1400	0.0740	0.2113	0.2082
47	43	47.72	0.3255	0.3270	0.1425	0.0745	0.2106	0.2089
56	56	56.93	0.3240	0.3250	0.1405	0.0735	0.2107	0.2085
reference:								
0 40	36	40.60	0.3075	0.2995	0.1530	0.0750	0.0534	0.0651

Run #3: diluted CO solution
747.0 mmHg
22.5 deg celcius
Stock CO concentration: 28.19 ppm
Diluted CO solution: 0.1713 ppm

time		time(min)	419	414	376	482	419c	414c
1	40	1.666667	0.295	0.2865	0.1525	0.0735	0.1745	0.1623
3	51	3.85	0.2965	0.288	0.1525	0.0735	0.176	0.1638
5	49	5.816667	0.2975	0.289	0.152	0.0735	0.1773	0.1651
7	38	7.633333	0.2975	0.2895	0.152	0.074	0.1771	0.1655
13	40	13.66667	0.2975	0.2895	0.1505	0.0735	0.1782	0.1666
20	30	20.5	0.298	0.2895	0.1505	0.073	0.1789	0.1668
30	0	30	0.2985	0.29	0.1505	0.0735	0.1792	0.1671
40	0	40	0.2985	0.29	0.1502	0.073	0.1796	0.1675
50	0	50	0.299	0.2905	0.1505	0.073	0.1799	0.1678
1 5	30	65.5	0.299	0.2905	0.152	0.0735	0.1788	0.1666
reference:								
0 35	20	35.33333	0.289	0.274	0.155	0.0725	0.1675	0.1486

Run #4: diluted CO solution
747.6 mmHg
22.3 deg celcius
Stock CO concentration: 28.3 ppm
Diluted CO solution: 0.0721 ppm

time			time(min)	419	414	376	482	419c	414c
	1	15	1.25	0.3120	0.3170	0.1520	0.0765	0.0622	0.0862
	3	15	3.25	0.3125	0.3175	0.1515	0.0765	0.0638	0.0877
	5	10	5.17	0.3130	0.3180	0.1515	0.0765	0.0643	0.0882
	7	20	7.33	0.3140	0.3190	0.1510	0.0770	0.0671	0.0907
	12	20	12.33	0.3140	0.3190	0.1505	0.0765	0.0676	0.0912
	19	50	19.83	0.3140	0.3195	0.1505	0.0755	0.0663	0.0907
	29	00	29.00	0.3140	0.3195	0.1505	0.0760	0.0670	0.0912
	37	40	37.67	0.3140	0.3198	0.1495	0.0765	0.0699	0.0941
	47	50	47.83	0.3135	0.3195	0.1495	0.0760	0.0688	0.0933
1	02	18	62.30	0.3120	0.3175	0.1495	0.0760	0.0673	0.0913
reference:									
1	15	0	75	0.317	0.3085	0.1535	0.0755	0.1951	0.183

Run #5: no CO in solution
747.6 mmHg
22.3 deg celcius
Stock CO concentration: none
Diluted CO solution: 0 ppm

time			time(min)	419	414	376	482	419c	414c
	1	00	1.00	0.2975	0.2965	0.1545	0.0730	0.0374	0.0569
	2	50	2.83	0.2975	0.2965	0.1545	0.0730	0.0374	0.0569
	4	35	4.58	0.2977	0.2965	0.1540	0.0730	0.0387	0.0579
	7	00	7.00	0.2960	0.2965	0.1545	0.0730	0.0359	0.0569
	14	10	14.17	0.2955	0.2965	0.1545	0.0732	0.0357	0.0571
	22	40	22.67	0.2945	0.2955	0.1545	0.0728	0.0341	0.0557
	31	15	31.25	0.2935	0.2955	0.1545	0.0728	0.0331	0.0557
	41	30	41.50	0.2935	0.2955	0.1535	0.0728	0.0354	0.0577
reference:									
0	54	10	54.17	0.3015	0.2890	0.1530	0.0730	0.0449	0.0525

APPENDIX B

Diffusion Through Adsorbing Media with Linear Isotherm

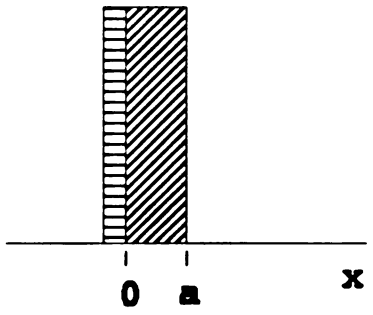

The one-dimensional diffusion through a film applied to an impermeable substrate can be conveniently described in mathematical terms by taking the film-substrate interface as the 'zero' reference, since no diffusion occurs across this boundary. For a film of thickness a,the film-solution interface then exists at point a along the x axis. If the adsorption of the diffusing solute proceeds quickly and reversibly along a linear isotherm, then S=RC. S is the local concentration of the adsorbed solute; C is the local concentration of the free solute; R is a constant. Since the adsorption process is fast relative to the diffusion, local equilibria can be assumed throughout the system. The boundary at the wall is always at a constant concentration C_o. The differential description of this system is

$$\frac{\partial C}{\partial t} = D' \frac{\partial^2 C}{\partial x} - \frac{\partial S}{\partial t}$$

$$\frac{\partial C}{\partial t} = \left(\frac{D'}{R+1}\right) \frac{\partial^2 C}{\partial x^2} = D \frac{\partial^2 C}{\partial x^2},$$

where

$$C = C_o, \quad x = a, \quad t \geq 0$$
$$\frac{\partial C}{\partial x} = 0, \quad x = 0, \quad t \geq 0$$

Applying the Laplace transformation yields

$$p\bar{C} = D\frac{\partial^2 \bar{C}}{\partial x^2},$$

Letting $q^2 = \frac{P}{D}$

$$\frac{d^2 \bar{C}}{dx^2} - q^2 \bar{C} = 0, \quad 0 < x < a$$

$$\bar{C} = C_o / p \text{ at } x = a$$

$$\frac{d\bar{C}}{dx} = 0,$$

which has the solution:

$$\bar{C} = \left[\frac{C_o \cosh(qx)}{p \cosh(qa)}\right] \Rightarrow$$
$$C = C_o \sum_{n=0}^{\infty} (-1)^n \text{erfc}\left[\frac{(2n+1)a - x}{2(Dt)^{1/2}}\right] + C_o \sum_{n=0}^{\infty} (-1)^n \text{erfc}\left[\frac{(2n+1)a + x}{2(Dt)^{1/2}}\right].$$

A more detailed derivation of this result can be found in *The Mathematics of Diffusion* (Crank, 1975).

On the following pages, this equation is numerically evaluated with Mathcad 3.0, using a diffusivity of 1×10^{-9} cm^2/s and a thickness of 3×10^{-5} cm. The matrix C gives the concentrations for various times after exposure to a 1×10^{-3} M solution of CO: 0.00001 seconds shown in the first column, 10.0 seconds shown in the far right column. The rows of the matrix give the position within the film: x=0 is shown in the top row, x=a is shown in the bottom row. A plot of concentration vs. position is then shown for various times.

base units: $cm \equiv 1L$ $g \equiv 1M$ $sec \equiv 1T$ $mmole \equiv 1Q$

derived units: $ml \equiv cm^3$ $M \equiv \frac{mmole}{ml}$

initial concentration: $C_o := 1 \cdot 10^{-3} \cdot M$

diffusivity: $D := 1 \cdot 10^{-9} \cdot \left[\frac{cm^2}{sec}\right]$

number of summation terms: $n := 100$ $i := 0, 1 .. n$

film thickness: $a := 3 \cdot 10^{-5} \cdot cm$

number of segments in profile: $m := 10$ $dx := \frac{a}{m}$ => $dx = 3 \cdot 10^{-6} \cdot cm$

$j := 0, 1 .. m$ $x_j := j \cdot dx$

$X := 0 \cdot cm, dx .. a$

time: $k := 0, 1 .. 6$

$$t := \begin{bmatrix} 0.000010 \\ 0.000100 \\ 0.001000 \\ 0.010000 \\ 0.100000 \\ 1.000000 \\ 10.00000 \end{bmatrix} \cdot sec$$

$$C_{j,k} := \left[C_o \cdot \left[\left[\sum_i (-1)^i \cdot \left[1 - erf\left[\frac{(2 \cdot i + 1) \cdot a - x_j}{2 \cdot \sqrt{[D \cdot t_k]}} \right] \right] \right] + \left[\sum_i (-1)^i \cdot \left[1 - erf\left[\frac{(2 \cdot i + 1) \cdot a + x_j}{2 \cdot \sqrt{[D \cdot t_k]}} \right] \right] \right] \right] \right]$$

$$C = \begin{bmatrix} 0 & 0 & 0 & 3.9407\cdot10^{-14} & 6.779\cdot10^{-5} & 9.1791\cdot10^{-4} & 1\cdot10^{-3} \\ 0 & 0 & 0 & 1.5665\cdot10^{-12} & 7.5862\cdot10^{-5} & 9.1892\cdot10^{-4} & 1\cdot10^{-3} \\ 0 & 0 & 0 & 8.0251\cdot10^{-11} & 1.006\cdot10^{-4} & 9.2193\cdot10^{-4} & 1\cdot10^{-3} \\ 0 & 0 & 0 & 2.6564\cdot10^{-9} & 1.4338\cdot10^{-4} & 9.2686\cdot10^{-4} & 1\cdot10^{-3} \\ 0 & 0 & 0 & 5.6994\cdot10^{-8} & 2.0607\cdot10^{-4} & 9.3359\cdot10^{-4} & 1\cdot10^{-3} \\ 0 & 0 & 0 & 7.9623\cdot10^{-7} & 2.9031\cdot10^{-4} & 9.4196\cdot10^{-4} & 1\cdot10^{-3} \\ 0 & 0 & 0 & 7.2904\cdot10^{-6} & 3.9683\cdot10^{-4} & 9.5175\cdot10^{-4} & 1\cdot10^{-3} \\ 0 & 0 & 1.9662\cdot10^{-13} & 4.4171\cdot10^{-5} & 5.2483\cdot10^{-4} & 9.6273\cdot10^{-4} & 1\cdot10^{-3} \\ 0 & 0 & 2.209\cdot10^{-8} & 1.7971\cdot10^{-4} & 6.715\cdot10^{-4} & 9.7463\cdot10^{-4} & 1\cdot10^{-3} \\ 0 & 1.9703\cdot10^{-14} & 3.3895\cdot10^{-5} & 5.0233\cdot10^{-4} & 8.3205\cdot10^{-4} & 9.8716\cdot10^{-4} & 1\cdot10^{-3} \\ 1\cdot10^{-3} & 1\cdot10^{-3} & 1\cdot10^{-3} & 1\cdot10^{-3} & 1\cdot10^{-3} & 1\cdot10^{-3} & 1\cdot10^{-3} \end{bmatrix} \cdot M$$

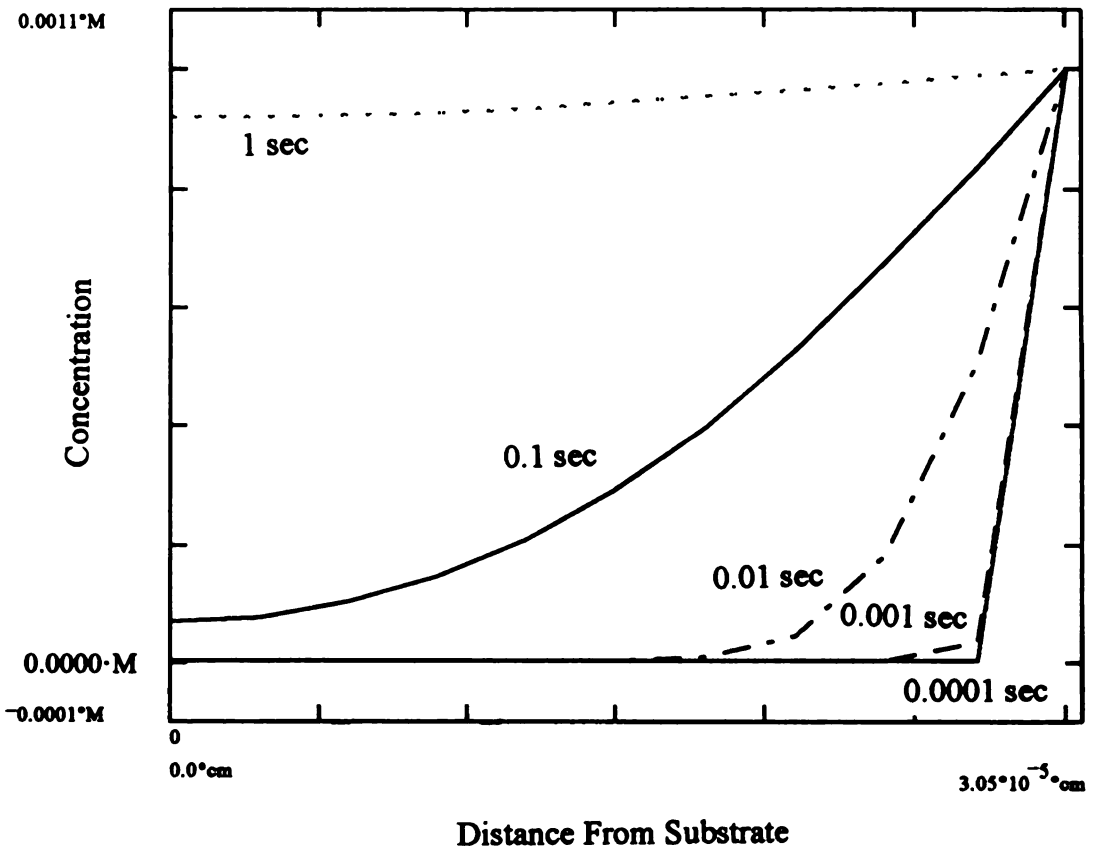

APPENDIX C

Diffusivity for Dense Region of Film

The time required for diffusion to occur is proportional to l^2/D. When this group of constants is known for the porous region, and time is known for both regions, and either l or D is known for the dense region, the remaining constant can be calculated from:

$$\frac{t_{dense}}{t_{porous}} = \frac{\left[\frac{l^2_{dense}}{D_{dense}}\right]}{\left[\frac{l^2_{porous}}{D_{porous}}\right]}.$$

On solving for the diffusion coefficient of the dense phase,

$$D_{dense} = \left[\frac{l^2_{dense}}{l^2_{porous}}\right]\left[\frac{t_{porous}}{t_{dense}}\right]D_{porous}.$$

If the dense phase diffusion required 15 minutes or 900 seconds, and the porous phase diffusion were complete after only 10 seconds, it follows that for an average distance of diffusion of 50 Å through dense media, the diffusion coefficient would be:

$$D_{dense} = \left(\frac{50}{3000}\right)^2\left(\frac{10}{900}\right) 10^{-9}\ \frac{cm^2}{s} = 3.1e\text{-}15\ \frac{cm^2}{s}.$$

If the characteristic distance of dense phase diffusion were slightly longer, 300 Å rather than 50 Å, then

$$D_{dense} = \left(\frac{300}{3000}\right)^2\left(\frac{10}{900}\right) 10^{-9}\ \frac{cm^2}{s} = 1.1e\text{-}13\ \frac{cm^2}{s}.$$

LIST OF REFERENCES

1. Atkins, W. P., 1986. Physical Chemistry, pp 431-462, W. H. Freeman and Company, New York.

2. Alben, J. O., 1978. In The Porphyrins (D. Dolphin, ed.) 3:323-345. Acedemic Press, New York.

3. Allinger, N. L., Cava, M. P., De Jongh, D. C., Johnson, C. R., Lebel, N. A., Stevens, C. L., 1976, Organic Chemistry,

4. Anderson, A. W., Bruce, J. R. Jr., Fallwell, E. L., 1958. U. S. 2,862,917 (Dec. 2) to Dow Corning Corp.

5. Arnold, H. R., and Foster, R. E., 1960. U. S. 2,943,066 (June 28) to E. I. du Pont.

6. Beek, J. B., and Pijpers, E. M. J., 1972. U. S. 3,647,754 (March 7) to Stamicarbon N. V..

7. Berglund, K. A., Tallant, D. R., and Dosch, R. G., 1986. In Science of Ceramic Chemical Processing (L. L. Hench, D. R. Ulrich, ed.) pp. 94-99. John Wiley and Sons, New York.

8. Bonnett, R., 1978. In The Porphyrins (D. Dolphin, ed.) 1:1-27. Acedemic Press, New York.

9. Bradley, D. C., and Wardlaw, W., 1951. J. Chem. Soc. 280-285.

10. Bradley, D. C., Mehrotra, R. C., and Wardlaw, W., 1952 (a). J. Chem. Soc. 2027-2032.

11. Bradley, D. C., Mehrotra, R. C., and Wardlaw, W., 1952 (b). J. Chem. Soc. 4204-4209.

12. Bradley, D. C., Mehrotra, R. C., and Wardlaw, W., 1952 (c). J. Chem. Soc. 5020-5023.

13. Bradley, D. C., Mehrotra, R. C., and Wardlaw, W., 1953. J. Chem. Soc. 2025-2030.

14. Bradley, D. C., Mehrotra, R. C., and Gaur, D. P., 1978. Metal Alkoxides, Academic Press, New York..

15. Brauman, J. I., and Blair, L. K., 1968. J. Amer. Chem. Soc. 90:6561

16. Brinker, C. J., Scherer, G. W., 1990. Sol-Gel Science, pp. 1-59, 787-881. Academic Press, New York..

17. Buchler, W. J., 1978. In The Porphyrins (D. Dolphin, ed.) 1:389-483. Acedemic Press, New York.

18. Case, L. C., 1968. U. S. 3,382,217 (May 7).

19. Chang, C. K. and Ebina, F., 1981. J. C. S. Chem. Commun. 778.

20. Colthrop, N. B., Daly, L. H., and Wiberley, S. E., 1990. Introduction to Infrared and Raman Spectroscopy, 3rd ed., Acedemic Press, New York

21. Coover, H. W. Jr., 1960. U. S. 2,948,712 (Aug. 9) to Eastman Kodak.

22. Crank, J., 1975. The Mathematics of Diffusion (2^{nd} ed.), Oxford University Press, London.

23. Dolphin, D. (ed.), 1978. The Porphyrins, Acedemic Press, New York.

24. Dawes, D. H., and Winkler, C. A., 1964. J. Polymer Sci., Part A, 2:3029-51.

25. DiNello, R. K. and Chang, C. K., 1978. In The Porphyrins (D. Dolphin, ed.) 1:289, Acedemic Press, New York.

26. Doeuff, S., J., Henry, Sanchez, C.,and Livage, M., 1987. J. Non. Cryst. Solids,89:206-216.

27. Dulebohn, J. I., Van Vlierberge, B., Berglund, K. A., Lessard, R., Yu, J., and Nocera, D., 1990. In Better Ceramics Through Chemistry IV (B. J. J. Zelinsky, C. J. Brinker, D. E. Clark, and D. R. Ulrich, ed.) pp.733-740, Mater. Res. Soc. Proc. 180, Pittsburgh, PA

28. Du Pont de Nemours, E. I., & Co., Bulletin on polyfunctional TYZOR organic titanates.

29. Falk, J. E., Smith, K. M., 1975. Porphyrins and Metalloporphyrins, Elsevier Scientific, New York.

30. Feld, R., and Cowe, P. L., 1965. The Organic Chemistry of Titanium, pp. 84-85, Butterworth and Co., Washington.

31. Felton, R. H., and Nai-Teng Yu, 1978. In The Porphyrins, ed. by D. Dolphin, 3:347-389. Acedemic Press, New York.

32. Fendler, J. D., 1982. Membrane Mimetic Chemistry, John Wiley and Sons, New York.

33. Flegler, S. L., Heckman, J. W. Jr., Klomparens, K. L., 1989. An Introduction to Electron Microscopy, Center for Electron Optics, Michigan State University, E. Lansing, MI.

34. Gagliardi, C. D., and Berglund, K. A., 1989. Processing Science of Advanced Ceramics, edited by Aksay, I. A., McVay, G. L., and Ulrich, D. R., Mater. Res. Soc. Proc. 155:127-135.

35. Gagliardi, C. D., and Berglund, K. A., 1990. Better Ceramics Through Chemistry IV, edited by Zelinski, B. J. J., Brinker, C. J., Clark, D. E., Ulrich, D. R., Mater. Res. Soc. Proc. 180:801-805.

36. Gouterman, M., 1978. In The Porphyrins (D. Dolphin, ed.) 3:1-167. Acedemic Press, New York.

37. Gaillissen, C. J., and Gancberg, A., 1956. U. S. 2,732,320 (Jan. 24).

38. Greenwood, N. N., and Earnshaw, A., 1984. Chemistry of the Elements, Pergamon Press, New York..

39. Harrick, N. J., 1967. Internal Reflection Spectroscopy, Interscience Publishers, New York..

40. Hartlein, R. C., and Olson, C. R., 1972. U. S. 3,647,846 (March 7) to Dow Corning Corp.

41. Haslam, J. H., 1952. U. S. 2,621,195 (Dec. 9) to E. I. du Pont.

42. Haslam, J. H., 1958. U. S. 2,822,348 (Feb. 4) to E. I. du Pont.

43. Hiroyuki, M., 1972. U. S. 3,658,926 (April 25) to Mitsubishi Petroleum Co., Ltd.

44. Hogan, J. P., and Witt, D. R., 1971. U. S. 3,622,521 (Nov. 23) to Phillips Petroleum Co.

45. Hopf, F. R., and Witten, D. G., 1978. In The Porphyrins (D. Dolphin, ed.) 2:188-189. Acedemic Press, New York.

46. Hubert-Pfalzgraf, L. G., 1987. New J. Chem. 11:663-675

47. Hwang, J., 1991. Private communication. Michigan State University, Lansing.

48. Hwang, S., and Kammermeyer, K., 1975. Membranes in Separations, John Wiley and Sons, New York.

49. Jaruzelski, J. J. and Sheppard, C. S., 1963. U. S. 3,106,570 (Oct. 8) to U. S. Steel.

50. Jen, J. S., and Thomas, T. D., 1975. J. Amer. Chem. Soc. 97(5):1199-1200.

51. Kesting, R. E., 1985. Synthetic Polymeric Membranes, John Wiley and Sons, New York.

52. Kreyszig, E., 1988. Advanced Engineering Mathematics, pp. 1248-1257, John Wiley and Sons, New York.

53. Kohn, L. S. and Guez, J. W., 1961. U. S. 3,014,826 (Dec. 26) to General Electric.

54. Lakshminarayanaiah, N., 1969. Transport Phenomena in Membranes, Acedemic Press, New York.

55. Lang's Handbook of Chemistry, 11th ed., edited by Dean, J. A., (1974) pp. (7)335-338. McGraw Hill, New York..

56. Langkammerer, C. M., 1952. U. S. 2,621,193 (Dec. 9) to E. I. du Pont de Nemours.

57. Lawham, W. M., 1965. U. S. 3,222,305 (Dec. 7) to Union Carbide.

58. Livage, J., 1986. Better Ceramics Through Chemistry II, edited by Brinker, C. J., Clark, D. E., Ulrich, D. R., Mater. Res. Soc. Proc. 121:717-724.

59. Livage, J., Henry, M., and Sanchez, C., 1988. Prog. Solid St. Chem. 18:259-341.

60. Long, D. A., 1977. Raman Spectroscopy, McGraw-Hill, New York.

61. Madaras, G. W., 1958. J. Soc. Dryers and Col., 74:834-41.

62. Marzocchi, A., 1972. U. S. 3,674,724 (July 4) to Owens Corning Fiberglass Corp.

63. McQuarrie, D. A., 1983. Quantum Mechanics, pp 437-490, University Science Books, Mill Valley, CA.

64. Mehrotra, R. C., 1967. Inorg. Chim. Acta Rev. 1:99-112.

65. Mehrotra, R. C. and Bohra, R., 1983. Metal Carboxylates, Academic Press, New York..

66. Mohr, C. M., Leeper, S. A., Engelgau, D. E., and Charboneau, B. L., Membrane Applications and Research in Food Processing, Noyes Data Corp., Park Ridge, N. J.

67. Orzechlowski, A. and MacKenzie, J. C., 1967. U. S. 3,326,877 (June 20) to Cabot Corp.

68. Paul, D. R., Morel, G., 1978. In Encyclopedia of Chemical Technology, 3rd ed. (Kirk-Othmer) 15:92-131. John Wiley and Sons, New York.

69. Pool, R., 1990. Science 247:634-636.

70. Payne, M., 1986. Master's Thesis, Michigan State University.

71. Rauner, L. A., and Tyler, L. J., 1962. U. S. 3,015,637 (Jan. 2) to Dow Corning Corp.

72. Reynolds, D. D., and Dunham, K. R., 1957. U. S. 2,789,969 (April 23) to Eastman Kodak.

73. Rettich, T. R., Battino, R., and Wilhelm, E., 1982. Ber. Bunsenges. Phys. Chem. 86, 1128

74. Sanchez, C., Livage, J., Henry, M., and Babonneau, F., 1988 (a). J. Non. Cryst. Solids,100:65-76.

75. Sanchez, C., Toledano, P., Ribot, F., 1990. Better Ceramics Through Chemistry IV, edited by Zelinski, B. J. J., Brinker, C. J., Clark, D. E., Ulrich, D. R., Mater. Res. Soc. Proc. 180:47-59.

76. Sanchez, C., Babonneau, F., Doeuff, S., and Leaustic, A., 1988 (b). Ulrastructure Processing of Advanced Ceramics, edited by Mackenzie, J. D., and Ulrich, pp. 77-87, John Wiley and Sons, New York.

77. Sanchez, C. and Livage, J., 1990. New J. Chem. 14:513-521.

78. Sianesi, D. and Caporiccio, G., 1966. U. S. 3,287,339 (Nov. 22) to Montecatini.

79. Skoog, D. A., and West, D. M., 1983. Principles of Instrumental Analysis (2nd ed.), pp 169-261, Saunders College, Philadelphia.

80. Smelts,K. C., 1969. U. S. 3,426,025 (Feb. 4) to E. I. du Pont.

81. Sotiriou, C. and Chang, C. K., 1988. J. Am. Chem. Soc. 110: 2264.

82. Spiro, T. G. 1983. In Iron Porphyrins - Part II. Physical Bioinorganic Chemistry Series (A. B. Lever and H. B. Gray, ed.) Addison-Wesley, New York

83. Stevens, M. P., and Gardner, J. D., 1965. Ind. Eng. Chem. Process Design and Development, 4(1):67-71.

84. Temin, S. and Baum, M., 1967. U. S. 3,321,552 (May 23) to Koppers Co.

85. Tu, A. T., 1982. Raman Spectroscopy in Biology, John Wiley and Sons, New York.

86. Ward, B. and Chang, C. K., 1982. Photochem. Photobiol., 35: 757.

87. Weber, F. X., 1962. U. S. 3,056,818 (Oct. 2) to B. F. Goodrich.

88. Yamane, M., Shinji, A., and Sakaino, T., 1978. J. Mater. Sci., 13: 865-870.

89. Yamdagni, R., and Kebarle, P., 1973. J. Amer. Chem. Soc. 95(12):4050-4052.

90. Yoldas, B. E., 1975. J. Mater. Sci., 10: 1856-1860.

91. Yoldas, B. E., 1977. J. Mater. Sci., 12: 1203-1208.

92. Zeitler, V. A., Brown, C. A., 1957. J. Phys. Chem. 61:1174

MICHIGAN STATE UNIV. LIBRARIES
31293007914520